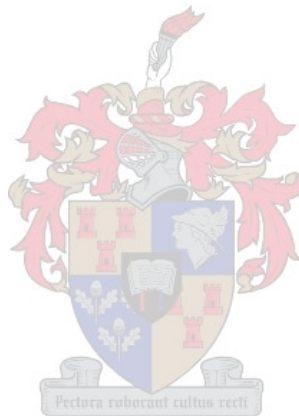


Orbital Lifetime Predictions of Low Earth Orbit Satellites and the effect of a DeOrbitSail

by

Michael A. Afful

*Thesis presented in partial fulfilment of the requirements for the degree of
Master of Engineering at Stellenbosch University*



Department of Electrical and Electronic Engineering
University of Stellenbosch
Private Bag X1, 7602, Matieland, South Africa.

Supervisors: Prof. W. H. Steyn

Dr. B. D. L. Opperman

December 2013

Declaration

By submitting this thesis electronically, I declare that the entirety of the work contained therein is my own, original work, that I am the owner of the copyright thereof (unless to the extent explicitly otherwise stated), that reproduction and publication thereof by Stellenbosch University will not infringe any third party rights and that I have not previously in its entirety or in part submitted it for obtaining any qualification.

Signature:

M. A. Afful

December 2013

Date:

Abstract

Throughout its lifetime in space, a spacecraft is exposed to risk of collision with orbital debris or operational satellites. This risk is especially high within the Low Earth Orbit (LEO) region where the highest density of space debris is accumulated.

This study investigates orbital decay of some LEO micro-satellites and accelerating orbit decay by using a deorbital sail. The Semi-Analytical Liu Theory (SALT) and the Satellite Toolkit was employed to determine the mean elements and expressions for the time rates of change. Test cases of observed decayed satellites (Iridium-85 and Starshine-1) are used to evaluate the predicted theory. Results for the test cases indicated that the theory fitted observational data well within acceptable limits.

Orbit decay progress of the SUNSAT micro-satellite was analysed using relevant orbital parameters derived from historic Two Line Element (TLE) sets and comparing with decay and lifetime prediction models. The study also explored the deorbit date and time for a 1U CubeSat (ZACUBE-01).

A proposed orbital debris solution or technology known as deorbital sail was also investigated to gain insight in sail technology to reduce the orbit life of spacecraft with regards to de-orbiting using aerodynamic drag. The deorbital sail technique significantly increases the effective cross-sectional area of a satellite, subsequently increasing atmospheric drag and accelerating orbit decay. The concept proposed in this work introduces a very useful technique of orbit decay as well as deorbiting of spacecraft.

Samevatting

Gedurende sy leeftyd in die ruimte word 'n ruimtetuig blootgestel aan die risiko van 'n botsing met ruimterommel of met funksionele satelliete. Hierdie risiko is veral hoog in die lae-aardbaan gebied waar die hoogste digtheid ruimterommel voorkom.

Hierdie studie ondersoek die wentelbaanverval van sommige Lae-aardbaan mikrosatelliete asook die versnelde baanverval wanneer van 'n deorbitaal meganisme gebruik gemaak word. Die Semi-Analitiese Liu Teorie en die Satellite Toolkit sagtewarepakket is gebruik om die gemiddelde baan-elemente en uitdrukkings vir hul tyd-afhanlike tempo van verandering te bepaal. Toetsgevalle van waargenome vervalde satelliete (Iridium-85 en Starshine-1) is gebruik om die verloop van die voorspelde teoretiese verval te evalueer. Resultate vir die toetsgevalle toon dat die teorie binne aanvaarbare perke met die waarnemings ooreenstem.

Die verloop van die SUNSAT mikrosatelliet se wentelbaanverval is ook ontleed deur gebruik te maak van historiese Tweelyn Elemente datastelle en dit te vergelyk met voorspelde baan-elemente. Die studie het ook ondersoek ingestel na die voorspelde baan-verbyval van 'n 1-eenheid cubesat (ZACUBE-01).

Die impak op wentelbaanverval deur 'n voorgestelde oplossing vir die beperking van ruimterommel, 'n deorbitaalseil, is ook ondersoek. So seil verkort 'n satelliet se ruimte-leeftyd deur sy effektiewe deursnee-area te vergroot en dan van verhoogde atmosferiese sleur en sonstralingsdruk gebruik te maak om die vervalproses te versnel. Hierdie voorgestelde konsep is 'n moontlike nuttige tegniek vir versnelde baanverval en beheerde deorbitalering van ruimtetuie om ruimterommel te verminder.

Acknowledgements

First and foremost I would like to thank God for the continuous guidance and mercy throughout my stay in South Africa. I forever remain grateful. My profound gratitude goes to my supervisors Prof. Willem H. Steyn and Dr. Ben D. L. Opperman for their guidance, valuable ideas and contributions towards the completion of my project. The continuous support in many aspects provided by Prof. Willem H. Steyn is greatly appreciated.

I would like to acknowledge the South African National Astrophysics and Space Science Programme (NASSP), University of Cape Town for awarding me the bursary to pursue further studies. Many thanks to the NASSP administrator, Mrs Nicky Walker, for her kind gesture and assistance. I sincerely appreciate the support and cooperation of my NASSP classmates and friends, Samuel Oronsaye, Temwani Phiri and Doreen Agaba.

I am grateful to the South African National Space Agency (SANSA) Space Science team for creating the enabling environment for my research. The warm hospitality, encouragement, and support granted me is highly acknowledged. I appreciate the support of Nicholas Ssessanga and Vumile Tyalimpi for their unwavering assistance. Many thanks to Mrs Elda Saunderson for proofreading my work.

I would like to express my heartfelt thanks to my parents Mr and Mrs Afful for all around continuous support from elementary school to present. Best of thanks to my brothers for their prayers and support. I am highly indebted to you all. Special thanks to my very best friend Ms. Lydia Quaye for her love, prayers and patience. May the good Lord reward you all.

Contents

Declaration	i
Abstract	ii
SameVatting	iii
Acknowledgement	iv
Content	iv
List of Figures	iv
List of Tables	iv
Nomenclature	iv
1 Introduction	1
1.1 Study Objectives	1
1.2 Thesis Overview	2
1.3 Research Motivation	2
2 Literature Review and Problem Description	4
2.1 Introduction	4
2.2 Historical Perspective	4

<i>CONTENTS</i>	vi
2.2.1 Reordering the Universe	5
2.2.2 Onset of the New Era	6
2.3 Space Debris Problem	7
2.3.1 Concerns and Threats posed by Space Debris	9
2.3.2 Mitigation Guidelines	10
2.4 DeOrbitSail Concept	11
2.5 Summary	13
3 Theoretical Background	14
3.1 Introduction	14
3.2 Equations of Motion	14
3.2.1 Two-Body Equation	16
3.2.1.1 Assumptions	16
3.2.1.2 Equation of Relative Motion	16
3.2.2 Constants of Motion	19
3.2.2.1 Energy Law	19
3.2.2.2 Angular Momentum	20
3.2.2.3 Trajectory Equation	20
3.3 Satellite State	21
3.3.1 Classical Orbit Parameters	21
3.4 Coordinate Systems and Transformations	23
3.4.1 Reference Systems	24
3.4.1.1 Earth Centred Inertial (ECI) System	24
3.4.1.2 Earth Centred Earth Fixed (ECEF) System	24
3.4.1.3 Geographic Co-ordinates	25
3.4.1.4 Perifocal Coordinate System	25

3.4.2	Coordinate Transformations	26
3.4.2.1	Transformation from ECEF to ECI	26
3.4.2.2	Transformation between Perifocal Coordinates and ECI	27
3.4.2.3	Position and Velocity from Orbital Elements	28
3.5	Two-Line Element Sets	29
3.6	Summary	30
4	Orbit Perturbations and Decay Employed in SALT	31
4.1	Introduction	31
4.2	Perturbation Effects on Orbital Elements	32
4.3	Osculating and Mean Elements	33
4.4	Variational Equations of Motion implemented in SALT	34
4.5	Effects of Earth Oblateness and Gravity	35
4.5.1	Non-spherical Gravity Potential	35
4.5.2	Earth Oblateness	36
4.6	Atmospheric Drag Effects	39
4.6.1	Evaluating Atmospheric Density	41
4.6.2	Atmospheric Density Model	42
4.7	Implementation of SALT in LIFTIM	43
4.7.1	Program Structure and Functionality	43
4.7.1.1	Elliptical Option	44
4.7.1.2	Circular Option	45
4.8	Summary	46
5	Simulation Environment	47
5.1	Introduction	47
5.2	LIFTIM Application	47

5.3	Data Preparation	47
5.3.1	Drag Coefficients	49
5.3.2	Decay Predictions	53
5.3.2.1	STK Lifetime Tool	54
5.4	Effects of using a DeOrbitSail	56
5.5	Summary	57
6	Results and Discussion	58
6.1	Introduction	58
6.2	Schatten data adopted in LIFTIM	58
6.3	Comparative Decay Results without a DeOrbitSail Mechanism	59
6.3.1	Iridium-85 Satellite	59
6.3.2	Starshine-1 Satellite	63
6.3.3	SUNSAT	66
6.3.4	1U CubeSAT (ZACUBE-01)	71
6.4	Theoretical Decay Results using a DeOrbitSail Mechanism	75
6.4.1	Iridium-85 Satellite	76
6.4.2	Starshine-1 Satellite	76
6.4.3	SUNSAT	77
6.4.4	1U CubeSAT (ZACUBE-01)	77
6.5	Discussion	78
6.5.1	Decay Predictions	78
6.5.2	Effects of the DeOrbitSail Mechanism	80
6.6	Summary	81
7	Conclusion and Future Work	83
7.1	Summary of Study	84

<i>CONTENTS</i>	ix
7.1.1 Lifetime Predictions	84
7.1.2 DeOrbitSail Mechanism	86
7.2 Conclusion	86
7.3 Further Research and Recommendation	87
Bibliography	87
Appendix	87
A Derivation of Equations of Motion	93
A.1 Two-Body Problem	93
A.2 Specific Mechanical Energy is a Constant	94
A.3 Specific Angular Momentum is a Constant	95
B Description of Files	97
B.1 Two-Line Element (TLE) file	97
B.2 Subroutine and Microflow	98
B.3 Input File Format used in Decay Analysis [1]	102
B.3.1 Iridium-85 Input File for Decay Prediction	103
B.3.2 Starshine-1 Input File for Decay Prediction	104
B.3.3 SUNSAT Input File for Decay Prediction	105
B.3.4 ZACUBE-01 Input File for Decay Prediction	106
C M-FILES	107
C.1 Routine for Estimated Drag Sail Size	107
C.2 TLE History File	108
C.3 Routine for Computing the various Decay Dates	111
C.4 Routine for Data in STK	113

D Predicted Decay Dates using STK	115
D.1 Iridium-85 Satellite	115
D.2 Starshine-1 Satellite	116
D.3 ZACUBE-01 Satellite	116
E De-orbitsail Technique	117
E.1 Configuration of a sail membrane	117
E.2 Observed Monthly Mean Solar Flux Data	118

List of Figures

2.1	Computer generated image of orbital debris in LEO [17].	7
2.2	LEO Environment Projection (LEGEND Study) [15].	8
2.3	Monthly number of catalogued objects in Earth orbit by object type [20]. .	9
2.4	Typical deployed $1.7 \times 1.7m$ sail [28].	12
3.1	Illustration of Kepler’s First Law.	15
3.2	Illustration of Kepler’s Second Law.	15
3.3	Two-body System adapted from [3].	17
3.4	Position vector of satellite in orbit [30].	18
3.5	Classical orbit elements [55].	22
3.6	(a) Earth Centred Inertial (ECI) Reference Frame. (b) ECEF and ECI frames related by changing sidereal time θ	24
3.7	(a) Geographic coordinates [12]. (b) Illustration of Geodetic and Geocentric latitudes.	25
3.8	A perifocal coordinate system adapted from [34].	26
3.9	Transformation from perifocal to ECI co-ordinate system using the three Euler angles ω, i, Ω [31].	28
4.1	General representation of secular and periodic variations of an orbital element [30].	33
4.2	Height vs. density for F10.7 values using the MSISE-90 model.	42

4.3	Actual (historic) and predicted smoothed monthly mean solar flux values at three activity levels required for predicting the atmospheric density. . . .	42
4.4	Actual (historic) and predicted smoothed monthly mean magnetic index values at three activity levels required for predicting the atmospheric density.	43
5.1	SUNSAT position errors using various drag coefficients adapted from [12]. . .	51
5.2	Iridium-85 position errors using various drag coefficients adapted from [12].	51
5.3	Starshine-1 position errors using various drag coefficients adapted from [12].	52
5.4	Dependence of orbital lifetime on drag coefficient for Starshine-1 satellite. .	52
5.5	STK Lifetime Tool (GUI for SUNSAT).	55
5.6	Comparison between Solar Flux Data for LIFTIM and Schatten.	56
6.1	Comparison in semi-major axis of Iridium-85.	59
6.2	Comparison in (a) eccentricity (b) inclination for Iridium-85.	60
6.3	(a) Comparison in apogee height. (b) Predicted decay date of Iridium-85 using LIFTIM and (c) STK.	61
6.4	Predicted orbit decay of Iridium-85 with and without Schatten solar flux data.	62
6.5	Comparison in (a) semi-major axis. (b) eccentricity of Starshine-1.	63
6.6	Comparison in (a) inclination. (b) apogee height of Starshine-1.	64
6.7	Predicted decay date of Starshine-1 using (a) LIFTIM. (b) STK	65
6.8	Predicted orbit decay of Starshine-1 with and without Schatten solar flux data.	66
6.9	(a) Average orbital height of SUNSAT since launch. (b) Evolution of semi-major axis from epoch until 1st Nov. 2012.	67
6.10	Evolution of (a) eccentricity. (b) inclination of SUNSAT from epoch until 1st Nov. 2012	68
6.11	(a) Comparison in apogee height from epoch until 1st Nov. 2012. (b) Predicted decay date of SUNSAT at two solar activity levels using LIFTIM.	69

6.12	Predicted decay date of SUNSAT using (a) STK. (b) LIFTIM with and without Schatten solar flux data..	70
6.13	Spectrum distribution of eccentricity for SUNSAT.	71
6.14	Evolution of (a) semi-major axis. (b) eccentricity of ZACUBE-01.	72
6.15	Evolution of (a) inclination. (b) apogee height of ZACUBE-01.	73
6.16	Predicted decay date of ZACUBE-01 (a) at two solar activity levels using LIFTIM. (b) STK.	74
6.17	Predicted orbit decay of ZACUBE-01 with and without Schatten data. . .	75
6.18	Estimates of sail size to deorbit in 25 years.	75
6.19	Predicted lifetime comparison of Iridium-85 with and without a $10m^2$ sail. .	76
6.20	Predicted lifetime comparison of Starshine-1 with and without a $10 m^2$ sail. .	76
6.21	Predicted lifetime comparison of SUNSAT with and without a $10 m^2$ sail. .	77
6.22	Predicted lifetime comparison of ZACUBE-01 with and without a $10 m^2$ sail using LIFTIM.	77
7.1	Orbit lifetime estimation process [7].	85
B.1	LIFTIM flow chart showing the routines for circular and elliptical cases [1].	101
D.1	Predicted decay date with a $10 m^2$ sail using STK for Iridium-85 satellite. .	115
D.2	Predicted decay date with a $10 m^2$ sail using STK for Starshine-1 satellite. .	116
D.3	Predicted decay date with a $10 m^2$ sail using STK for ZACUBE-01 satellite. .	116
E.1	Sail concept, stowed (left) and deployed (right) [28].	117
E.2	Observed monthly mean solar flux data	118

List of Tables

3.1	Relationship between conic section and eccentricity.	20
3.2	Parameters defining an ellipse [4].	22
3.3	Transforming position and velocity vectors to Kepler elements [4].	23
4.1	Pertubing effects on orbital elements.	33
5.1	Geometry of decayed satellites used in evaluating SALT.	48
5.2	Two-Line Elements at time closest after launch.	48
5.3	TLE-derived state vectors and osculating orbital elements of dates closest to launch.	49
5.4	Drag coefficients, position and velocity errors for SUNSAT, Iridium-85 and Starshine-1.	50
5.5	Optimum drag coefficients	53
5.6	Orbital parameters for ZACUBE-01.	54
6.1	Predicted deorbit dates for test case satellites.	79
6.2	Predicted deorbit dates & time for SUNSAT and ZACUBE-01.	80
6.3	LIFTIM predicted orbital lifetime with and without a deorbisail.	81
6.4	STK predicted orbital lifetime with and without a deorbisail.	82
B.1	Functional grouping of Subprograms	98

Nomenclature

Abbreviations and Acronyms

1U	1-Unit
ADR	Active Debris Removal
ASCII	American Standard Code for Information Interchange
BC	Ballistic Coefficient
CIRA	COSPAR International Reference Atmosphere
CPUT	Cape Peninsula University of Technology
DCM	Direction Cosine Matrix
DTM	Drag Temperature Model
ECI	Earth Centred Inertial
ECEF	Earth Centred Earth Fixed
FCC	Federal Communications Commission
FFT	Fast Fourier Transform
F'SATI	French South African Institute of Technology
GCI	Geocentric Inertial
GEO	Geosynchronous Orbit
GMST	Greenwich Meridian Standard Time
GSFC	Goddard Space Flight Center
GUI	Graphical User Interface
HPOP	High Precision Orbit Propagator
IADC	Inter-Agency Space Debris Coordination Committee
IKAROS	Interplanetary Kite-Craft Accelerated by Radiation of the SUN
ISS	International Space Station
LEGEND	LEO-to-GEO Environmental Debris Model
LEO	Low Earth Orbit

LIFTIM	Lifetime Prediction Program
MEO	Medium Earth Orbit
MSAFE	MSFC Solar Activity Future Estimation Model
MSFC	Marshall Space Flight Center
MSIS	Mass Spectrometer Incoherent Scatter
NASA	National Aeronautics and Space Administration
NOAA	National Oceanic and Atmospheric Administration
NORAD	North American Aerospace Defense Command
SALT	Semi Analytical Liu Theory
SGP4	Simplified General Perturbation No. 4
SLR	Satellite Laser Ranger
STK	Satellite ToolKit
TLE	Two Line Element
USSSN	United States Space Surveillance Network

Greek Symbols

μ	Gravitational Parameter
ν	True Anomaly
ε	Specific Mechanical Energy
Ω	Right Ascension of the Ascending Node
Υ	Vernal Equinox
ω	Argument of Perigee
α_r	Right Ascension
δ_d	Declination
λ	Longitude (Chapter 3)
ϕ	Latitude (Chapter 3)

Φ	Potential Function
φ	Geocentric Latitude (Chapter 4)
ρ	Atmospheric Density
θ	Geographic Longitude (Chapter 4)

Lowercase Letters

m	Mass
a	Semi-major Axis
e	Eccentricity
m_i	Mass of i^{th} Body
\dot{m}_i	Time rate of change of mass of the i^{th} body
\mathbf{h}	Specific Angular Momentum
p	Semi-parameter
i	Inclination
r_a	Apogee Radius
r_p	Perigee Radius
b	Semi-minor Axis
n	Mean Motion
\mathbf{n}	Nodal Vector
ω_{\oplus}	Earth Rotation Rate (Chapter 3)
θ_{nm}	Equilibrium longitude for J_{nm}
c_D	Drag Coefficient
∇	Gradient operator (del)
\mathbf{a}_{drag}	Acceleration due to Atmospheric Drag
r	Geocentric distance (Chapter 4)
ω_a	Earth rotational speed (Chapter 4)
$(\dot{r}_a)_d$	Average rate of change in r_a due to drag

$(\dot{r}_p)_d$	Average rate of change in r_p due to drag
\dot{a}_m	Rate of change of the transformed mean equation of motion of a
\dot{e}_m	Rate of change of the transformed mean equation of motion of e
\dot{i}_m	Rate of change of the transformed mean equation of motion of i
$\dot{\omega}_m$	Rate of change of the transformed mean equation of motion of ω
$\dot{\Omega}_m$	Rate of change of the transformed mean equation of motion of Ω
$\dot{\mathbf{M}}_m$	Rate of change of the transformed mean equation of motion of \mathbf{M}

Uppercase Letters

M	Mass of Earth
G	Gravitational Constant
R	Radius (Chapter 3)
\mathbf{R}	Position Vector
$\ddot{\mathbf{R}}_i$	Acceleration vector of the i^{th} body
$\dot{\mathbf{R}}_i$	Velocity vector of the i^{th} body
\mathbf{F}_{Drag}	Drag Force
\mathbf{F}_{Thrust}	Thrust Force
\mathbf{F}_{SUN}	External Force from the SUN
\mathbf{F}_{MOON}	External Force from the MOON
V	Satellite's Velocity
\mathbf{V}	Velocity Vector
N	Ascending Node
M	Mean Anomaly
E	Eccentric Anomaly
$\ddot{\mathbf{R}}$	Acceleration (Chapter 4)
$X_\omega, Y_\omega, Z_\omega$	Co-ordinate Axes
\mathbf{P}, \mathbf{Q}	Unit Vectors

B^*	Drag Term
J_2, J_3, J_4	Harmonic Terms
A	Cross-sectional Area
R_e	Equatorial radius of the Earth (Chapter 4)
P_n	Legendre polynomials of degree n, order 0
P_{nm}	Associated Legendre polynomials of degree n, order m
A_p	Magnetic Index
$F_{10.7}$	Solar Flux
H	Altitude (Chapter 4)

Chapter 1

Introduction

1.1 Study Objectives

The aim of this project is to study and investigate the present orbit decay progress of a Low Earth Orbit satellite (SUNSAT) by using relevant orbital parameters derived from historic NORAD Two Line Element (TLE)¹ [13] sets and comparing it with decay and lifetime prediction models such as the Semi-Analytical Liu Theory (SALT) [1] and Satellite Toolkit (STK) [44].

The study objectives are:

1. Investigate the accuracy of predicted orbital element evolution over (test) satellite's lifetime (re-entry date).
2. Investigate the effects of orbit perturbations on time evolution of satellite orbital elements and the orbital lifetime of SUNSAT.
3. Test the theory and long-term predicted solar and magnetic data sets by implementing relevant algorithms and software packages and comparing the theoretical results with observed/ historic TLE-derived orbital parameters.
4. Investigate the FP7 DeOrbitSail mission [42] to reduce the lifetime of satellites with regards to deorbiting using aerodynamic drag.

¹TLE - data format used to convey sets of orbital elements that describe the orbits of Earth-orbiting satellites. The format is specified by the North American Aerospace Defence Command (NORAD) and the National Aeronautics and Space Administration (NASA).

1.2 Thesis Overview

In Chapter 2, background information on historical concepts, an introduction to the space debris problem as well as the DeOrbitSail mission is presented. Chapter 3 focuses on theoretical overview on orbit fundamentals. The equations developed serve as an illustration for understanding two-body mechanics. Co-ordinate frames used to describe the orientation and position of a satellite are introduced. Co-ordinate transformation matrices needed for vector transformation between the various co-ordinate frames are also explained.

Chapter 4 deals with orbit perturbations and decay as implemented in SALT. The mathematical modelling of the orbit perturbation forces and methods used in a general perturbed orbit are explained. The effects of perturbations on a satellite's orbital parameters are presented. The software structure is discussed. The SALT employed in this study is presented as well as the atmospheric model, and its associated dynamics are discussed.

The theme of Chapter 5 is the simulation environment. Description of the methods used in obtaining the results are presented. The results of this study are presented and discussed in Chapter 6. A conclusion, with a summary of the project findings, some recommendations and future work are given in Chapter 7.

1.3 Research Motivation

Spacecraft are exposed to the risk of collisions with orbital debris² and operational satellites throughout its launch, early orbit and mission phases. This risk is especially high during passage through, or operations within, the Low Earth Orbit (LEO) region, because this region is highly concentrated with "space junk". Understanding the lifetime of these spacecraft in LEO would be useful for studying the long term evolution of space objects in assessing the risk of potential collision of these objects with active spacecraft.

An increasing number of countries have active or planned space programmes which would result in the growth of the number of satellites to be launched over the next decade. Satellite launches both replace satellites whose operational lives have ended and place new satellites in orbit. The outcome of these current and future satellite launch activities is and will be an increase in the number of satellites and launch vehicle upper stages in orbit. There are also several satellites launched into LEO for short duration missions.

²Orbital debris, also known as space debris, space junk or space waste, is a collection of objects in orbit around Earth that were created by humans but no longer serve any useful purpose. These objects consist of everything from spent rocket stages and defunct satellites to erosion, explosion and collision fragments.

The growing population of spacecraft that have completed their missions, especially those launched for short-duration, low altitude missions, continues to accumulate, which will unavoidably lead to an increasing space clutter of debris.

A satellite in LEO naturally experiences an orbital decay process. The physical orbital lifetime is determined almost entirely by interaction with the atmosphere, which leads to re-entry of the spacecraft through the Earth's atmosphere. Segments of the satellites' internal structure and other instruments may endure the adverse heating and forces of the re-entry process, ultimately impacting the Earth's surface.

Prediction of satellite lifetime, or of an accurate re-entry date, is important to satellite planners, trackers, users and frequently, to the general public. Re-entry of large satellites may pose a risk to humans, hence, information concerning the potential impact time and location of satellites will aid in warning affected areas of the re-entry, thus allowing for preventive action to be taken. The prediction of satellite lifetime depends on factors such as knowledge of the satellite's initial orbit parameters, satellite mass to cross-sectional area ratio (in the direction of motion), behaviour of the upper atmospheric density and how it responds to space environmental parameters.

Although a comprehensive atmospheric model is used to describe atmospheric density variations in time, season, altitude and latitude, there are uncertainties in the prediction of a satellite's attitude and solar and geomagnetic indices. Even with most of the quantities of the model known, there appears to be an irreducible level below which it is impossible to predict accurately over very long time scales [4].

Chapter 2

Literature Review and Problem Description

2.1 Introduction

An overview of information relating to the research and historic events which lead to the onset of civilisation and the continual advancement in satellite designs will be addressed.

A short review of the historical aspects will be given. The current space debris problem and its associated mitigation guidelines will be introduced. Finally, the DeOrbitSail mission, using a drag sail as an aerodynamic method to deorbit satellites, will be addressed briefly.

2.2 Historical Perspective

Since the dawn of civilisation, man has looked to the heavens with awe searching for exceptional signs. Some of these men became experts in deciphering the mystery of the stars and developed rules for governing life based upon their placement. Presently, it is known that the alignment of man-made structures such as the pyramids and Stonehenge were inspired by celestial observations, and that these inventions themselves were used to measure the time of celestial events such as the vernal equinox [2].

One of man's earliest endeavours for trying to understand the motions of the Sun, Moon and other planets comes from the belief that they controlled his destiny. Other reasons were the need to measure time and later the use of celestial objects for navigation [3]. More than four thousand years ago, the Egyptians and Babylonians were, for the most part,

content with practical and religious applications of their heavenly observations although they contributed immensely to astronomy by their observations and calendar. The ancient Greeks took a more contemplative approach to studying space. It was the Greek view of the cosmos that governed western philosophy for some time [4].

The modern orbit types have been developed based on theories dating back centuries. These early astrologers; Aristotle (384 - 322 B.C), Aristarchus (300 B.C), Hipparchus (130 B.C) proposed and developed comprehensive rules to explain phenomena such as the motion of objects and to predict the motion of planets. Although, there were no physical principles on which to base their rules, some of the results obtained were very accurate and remained virtually unchanged as it was an accepted theory throughout the Middle Ages [3].

The early astrologers accomplished much work which laid the basis for the next generation of scholars namely Nicholas Copernicus, Galileo Galilei, Johannes Kepler and Isaac Newton. These men took the concepts and values discovered earlier and integrated them with newly formed orbital theories to describe the motion of planets. Their observations and rules explaining the motion of the celestial bodies ultimately succeeded and was represented in the laws of Newton. For further information, see [2, 3, 4].

2.2.1 Reordering the Universe

With the Renaissance and Humanism came a renewed emphasis on the accessibility of the heavens to human thought. Scholars reordered the theory explaining the universe by disproving some of the comprehensive rules governing the universe at that time. Johannes Kepler (1571 - 1630), who worked on the orbit of the planet Mars, found that Mars' orbit and that of all planets were represented by an ellipse with the Sun at one of its foci, rather than a circle as postulated by Copernicus. The discovery of Mars' elliptical orbit led to another breakthrough; the first of Kepler's three laws of planetary motion which describes the orbit of the planets around the Sun, with the third law following in 1619 [6].

Though Kepler's laws were only a description and not an explanation of planetary motion, it typified the observed motions of the planets which brought about a new emphasis on finding and quantifying the physical cause of motion [6]. However, these laws made no attempt to describe the forces behind them.

Up to Kepler's time, humanity's efforts to explore the universe had been remarkably successful, but constrained by the limits of human eyesight. This was to change: a few prominent individuals, Galileo Galilei (1564 - 1642), Rene Descartes (1596 - 1650) and

John Napier (1550 - 1617) contributed to science by discovering theorems and algorithms to reduce all the tedious calculations. Gottfried Leibniz, Edmund Halley, Christopher Wren and Robert Hooke were some of the key players in the scientific revolution.

To complete the astronomical revolution which had started and advanced by Kepler and Galileo, most of the laws had to be united under one set of natural laws. Isaac Newton (1642 - 1727) answered this challenge. He invented calculus and developed his three laws of motion and the law of Universal Gravitation. These laws of motion and Universal Gravitation were published in the *Mathematical Principles of Natural Philosophy (Principia)* in 1687 which formulated a grand view that was consistent and capable of describing and unifying the simple motion of a falling apple and the motion of the planets [4, 5].

Other prominent men also enriched human knowledge by means of their contribution with regards to other interesting discoveries in celestial mechanics. Nevertheless, Newtonian mechanics prevailed for some time until Albert Einstein (1879 - 1953) redefined gravity, time and space in his formulation of general and special relativity.

2.2.2 Onset of the New Era

By the dawn of the Space Age (1957), astronomers had constructed a view of the universe radically different from earlier concepts. They continued to explore the universe with their minds and Earth-based instruments. But since the mid-twentieth century, nations have also been able to launch probes into space to explore the universe directly. Thus, advances in our understanding of the universe increased with our efforts to send probes and people into space. These missions began with the advent of the hot air balloon and sounding rockets used for the purpose of aerial observation from the upper atmosphere. Balloons were ultimately succeeded by satellites which proved to serve diverse applications.

From the first man-made satellite, Sputnik 1 to the International Space Station (ISS), the largest satellite in Earth orbit, the use and need for satellites have increased substantially. To satisfy multi-task requirements, complex large satellites were designed and manufactured with intricate kinds of payload systems and other scientific instruments onboard to carry out respective mission objectives. Advances in rocket science and telemetry made it possible to place sensors in orbit and relay information back to Earth. Improved technologies and miniaturisation of electronics have allowed small satellites (micro, nano) to accomplish many of the tasks of the larger predecessors, and at a fraction of the cost and time required to construct a traditional satellite [9].

Since 1957, thousands of satellites have been launched into the Earth's exo-atmosphere. The majority of these are currently defunct and orbit in a cloud of debris around the Earth, known as space debris or 'space junk'. This relatively dense debris cloud pose serious collision risks with operational satellites.

Today, satellites, interplanetary probes and space-based instruments continue to revolutionise our lives and understanding of the universe.

2.3 Space Debris Problem

The terms space debris and orbital debris are often used interchangeably, with the following definition as adopted by the Inter-Agency Space Debris Coordination Committee (IADC): "Space debris are all man-made objects including fragments and elements thereof in Earth orbit or re-entering the atmosphere that are non functional" [17].

The contribution of artificial bodies (i.e. spent satellites and their components) to the debris population in space was not considered in the early years of space exploration. Previous practices and procedures allowed unregulated growth of orbital debris. However, because of the risk of collisions the issue of orbital debris has become extremely important, requiring that space industries monitor debris orbiting Earth and develop procedures to curb its growth in future. Figure 2.1 shows a computer generated image of the concentration of orbital debris in LEO.

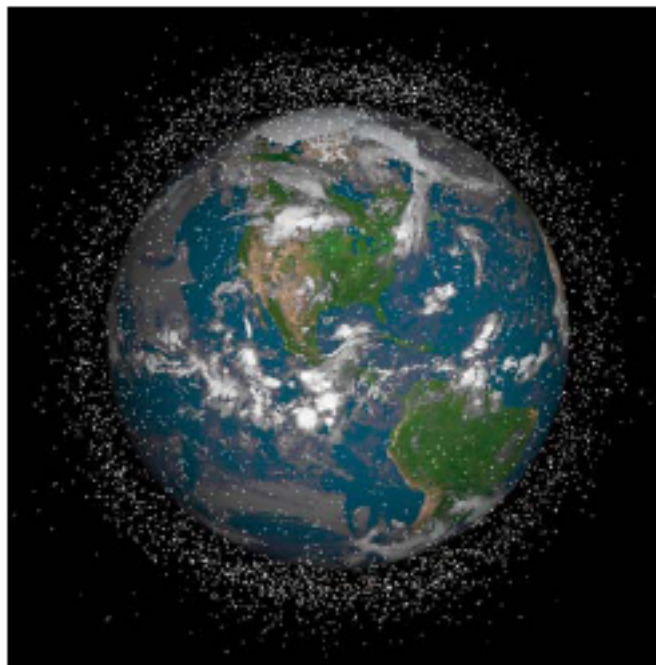


Figure 2.1: Computer generated image of orbital debris in LEO [17].

Space debris is a problem of the near Earth environment with global dimensions to which all spacefaring nations have contributed over more than half a century of space activities. As the space debris environment evolved progressively, it became evident that understanding its causes and controlling its sources are a prerequisite to ensure safe space flight [14]. In the past, the natural meteoroid environment was considered in satellite designs. Present and future satellite designs have to take in account space debris in addition to the natural environment. Past design practices, including deliberate and unintentional explosions in space, have created a significant debris population within the region of operationally important orbits [3]. Much of these debris are resident at altitudes of considerable operational interest.

Space debris have been a growing concern due to the potential risk of causing collisions. Research has shown that the debris problem is growing fast and hence is a burden to operational satellites in both the LEO and Geosynchronous Orbit (GEO) regimes. The risk will certainly grow as more nations gain the technology to launch satellites into Earth orbit [16]. The National Aeronautics Space Administration (NASA) LEGEND (LEO-to-GEO Environmental Debris model) predicted a non-linear growth of objects for the LEO region if no mitigation measures [15] are followed, as shown in Figure 2.2.

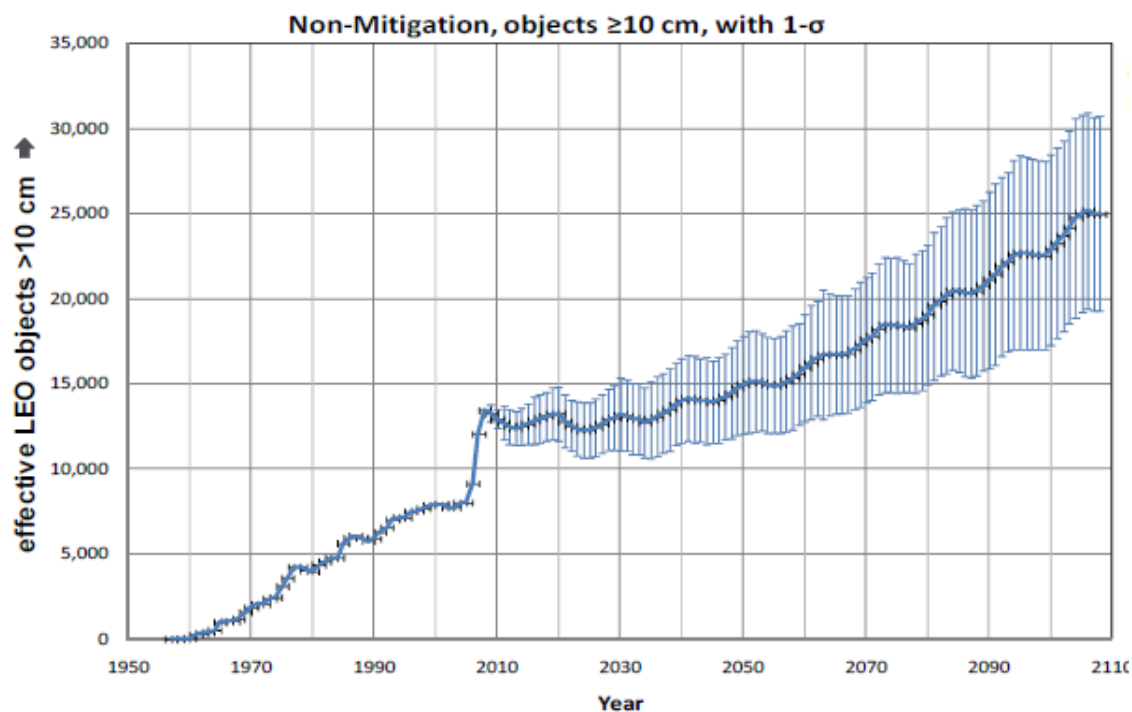


Figure 2.2: LEO Environment Projection (LEGEND Study) [15].

In order to have a sustainable LEO population, the implementation of commonly adopted mitigation measures, as well as Active Debris Removal (ADR), will be required.

2.3.1 Concerns and Threats posed by Space Debris

The most important single source of debris proliferation is on-orbit collisions of satellites and rocket stages, sometimes more than 20 years after their launch [14]. Collisions are either accidental or deliberate. The Chinese shot down their satellite (deliberately) [35] while an Iridium-Cosmos collision was accidental [43]. When these collisions happen they also produce many fragments. The abandonment of satellites and upper stages in their current orbit, after their operational lifetime, is also a major contributor to the space population. These practises have led to the accumulation of approximately 1968 tons of orbital debris as reported by NASA in 1995 [18]. The average growth rate in debris population of about 5% per annum in LEO is as a result of assets being launched into space at a faster rate than being removed by either artificial or natural means.

Studies have shown that, even if there were no new launches, collisions of existing satellites and rocket bodies would lead to a growing debris count as more pieces of debris are created which in turn collide with each other. Therefore collisions will most likely be the largest contributor of debris generation in LEO in the near future [19]. Figure 2.3 illustrates the increase in number of space objects. There is an increasing growth trend that will adversely impact our expected future, if not corrected. It also shows a summary of all objects ($d > 10$ cm) in Earth orbit officially catalogued by the U.S. Space Surveillance Network. “Fragmentation debris” includes satellite breakup debris and anomalous event debris, while “mission-related debris” includes all objects dispensed, separated or released as part of a planned mission.

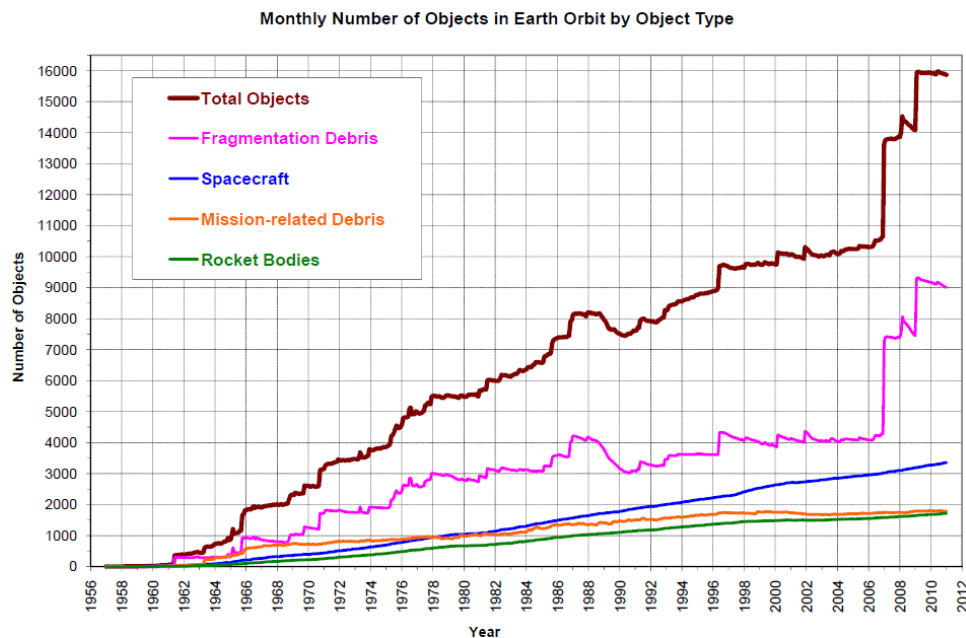


Figure 2.3: Monthly number of catalogued objects in Earth orbit by object type [20].

The growth of space debris has become an issue of concern as it continues to have an impact on the utilisation of space assets. This impacts both the immediate and long term effects of collisions and explosions in the space debris population. The motivation for this study is as a result of the growing concern about ‘space junk’ and how it can be controlled by means of deorbiting these satellites after their operational lifetime, hence the requirement for lifetime predictions. Removal of some of these defunct satellites (e.g. SUNSAT) in the LEO region, is the primary focus.

2.3.2 Mitigation Guidelines

Controlling the growth of the space debris population is a high priority for most major spacefaring nations for future generations. Currently, the man-made debris environment in the LEO region is assumed to dominate the natural meteoroid contribution, except for a confined size regime around 0.1 mm diameter [21].

Mitigation measures take the form of preventing the creation of new debris, designing satellites to withstand impacts by small debris and implementing operational procedures such as using orbital regimes with less debris, adopting specific satellite attitudes and even maneuvering to avoid collisions with debris.

Several orbital debris mitigation guidelines have been issued by various organisations - NASA, U.S Government, the IADC and the Federal Communications Commission (FCC). Some of these guidelines are summarised here shortly, with the focus on post mission disposal of satellites in LEO for the purpose of this study.

NASA [22] have three main options for post mission disposal in LEO:

- atmospheric re-entry,
- maneuvering to storage orbits,
- direct retrieval.

The U.S Government [23] have similar mitigation guidelines, but with some additions in the various domains.

- Option one includes the human casualty risk, which should be less than one in ten thousand for re-entry into the Earth’s atmosphere.
- The second option discusses several storage regimes:
 - between LEO and MEO,
 - between MEO and GEO,

- Above GEO,
- Heliocentric, Earth-escape.
- The last option makes use of time constraints:
 - removal from orbit should be as soon as practical after completion of a mission.

The IADC guidelines [17] give alternatives for space structures to be disposed of by either deorbiting, direct re-entry, maneuvering to an orbit that reduces the lifetime and finally by direct retrieval.

The FCC guidelines [24] comprise three different procedures for post mission disposal similar to that of NASA, but with an addition in atmospheric re-entry:

- use the propulsion system of a spacecraft to lower the orbit attitude towards the Earth's atmosphere.
- maneuver the satellite into an orbit where atmospheric drag will accelerate its re-entry, causing it to decay within 25 years after launch by mechanically increasing the satellite's cross-sectional area.

A satellite system operator should submit a debris mitigation plan for authorisation to enhance a continuous debris free environment as suggested by the FCC. For detailed description of these mitigation guidelines, refer to the following papers [22, 23, 17, 24] respectively.

2.4 DeOrbitSail Concept

A non-rocket form of space travel known as solar sailing was conceived by Tsiolkovsky [37] and Tsander in the 1920's [38]. However, critical developments had to wait till the mid seventies where a rendezvous mission was proposed making use of a solar sail, but was later cancelled. Albeit, the study sparked international interest in solar sailing for future mission applications [25].

Solar sailing is a means of travelling in "space" by using the energy from the Sun. It gains momentum from photons, the quantum packets of energy of which sunlight is composed. Solar sailing is a unique form of propellant-less propulsion reducing the reliance on a reaction mass, such as chemical propulsion. As solar sails are not limited by a finite reaction mass, they can provide continuous acceleration, limited only by the lifetime of the sail film in the space environment [26]. In order to generate as high an acceleration as

possible from the momentum transported by the intercepted photons, solar sails must be made extremely light and also near perfect reflectors.

A solar sail is thus a large membrane of thin reflective material which reflects incident photons from the Sun, thereby causing acceleration [27]. Solar sailing could be compared to the sail of a ship, but using solar radiation pressure for propulsion instead of the wind. Figure 2.4 shows a typical solar sail when deployed. For a comprehensive discussion on the dynamics of a solar sail, orbit configuration and types, its performance and mission related technologies, refer to [26, 27].

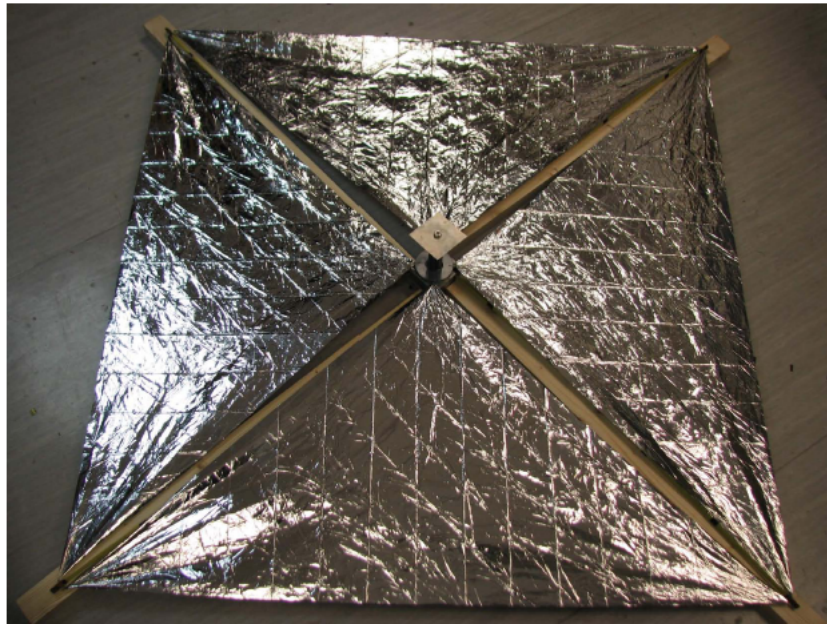


Figure 2.4: Typical deployed $1.7 \times 1.7m$ sail [28].

The DeOrbitSail mission [42] is to employ a drag sail as a deorbiting mechanism to augment the proposed methods for debris mitigation. DeOrbitSail is a deorbiting device that uses aerodynamic drag for deorbiting. It is very low in complexity, has a low parasitic mass and does not require any propellant. The purpose of the drag sail is to demonstrate and prove the effectiveness of drag deorbiting, by increasing the drag area and shortening the orbit decay period. Solar radiation pressure can also be used for the general maneuvering of satellites to higher or lower orbits. Solar sailing is more effective above about 650 km when the constant solar force becomes more dominant than the drag force and below 650 km the drag force becomes exponentially more dominant.

Investigations have shown that the use of a solar or drag sail as a deorbiting mechanism can be an advantageous, low-cost solution for deorbiting satellites, as the total cost of the technology is not prohibitive. For certain missions, it can be a better solution than

a traditional chemical propulsion system, which would require large amounts of chemical propellant [28].

The solar sail technology was employed on the interplanetary IKAROS satellite launched in May, 2010. With a 200 m^2 sail, its objective was to demonstrate the solar sailing principle [29]. Though the solar sail had been successfully deployed, its overall effectiveness and success still need to be assessed. The orbital lifetime of Nanosail-D2 (240 days) showed the efficiency of the drag sail technology [39]. The benefits and capabilities of solar and drag sailing as a means of deorbiting still requires further investigation, hence the motivation for this study.

Evaluation of the potential risk involved with space debris have led to possible solutions and reduction measures such as the deorbital sail concept. Active removal of defunct spacecraft, upper stages and other “space junk” may be the most efficient means of avoiding future collisions. However, it might not be cost effective and would require difficult maneuvering of objects in space.

2.5 Summary

This chapter provides a description of the history leading to the dawn of the space age. A brief overview of the historical foundation is discussed. The space debris problem with an outline of some proposed mitigation guidelines are presented. These guidelines cover the overall environmental impact of space missions with a focus on the following: limitation of debris released during normal operations, minimisation of the potential for on-orbit break-ups, prevention of on-orbit collisions and post-mission disposal (which is the main aim of this study).

Recent events have accentuate the growing problem that orbital debris, or “space junk” poses to spacecraft. In order to control this problem, the idea of the deorbital sail concept is proposed and described. This seeks to demonstrate satellite deorbiting manoeuvres for space debris mitigation and to reduce the deorbit time of satellites by increasing the drag area.

Chapter 3

Theoretical Background

3.1 Introduction

Understanding the motion of an object in space is fundamental to orbit propagation and determination. In this chapter, the necessary theory and concepts of orbital mechanics using the equations of motion for two-body and N-body problems are introduced. Detailed analyses, solution or implementation of the two-body or N-body problem, however, falls outside the scope of this study and are not addressed.

Relevant coordinate frames used in this work are discussed. The transformation matrices employed to convert coordinates from one reference frame to another are presented. Because of the importance of historic Two-Line Element data used in the study, this topic is addressed in some detail, but the popular Simplified General Perturbation (SGP4) orbit propagator [13] is not covered.

3.2 Equations of Motion

Orbital equations of motion are governed by Kepler and Newton's laws. Kepler's laws describe the motion of planets in the solar system and can be applied to artificial Earth satellite motion as well. Kepler's laws are illustrated in Figures 3.1 and 3.2 and in [6]:

- FIRST LAW - The orbits of the planets are ellipses with the Sun at one focus.
- SECOND LAW - The line joining the planet to the Sun sweeps out equal areas in equal times.

- **THIRD LAW** - The square of the orbital period of a planet is proportional to the cube of the mean distance from the Sun.

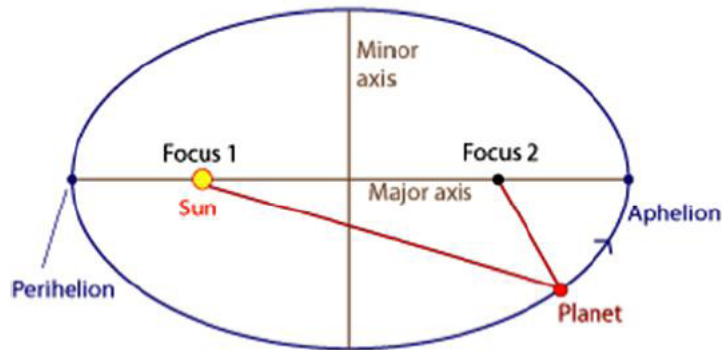


Figure 3.1: Illustration of Kepler's First Law.

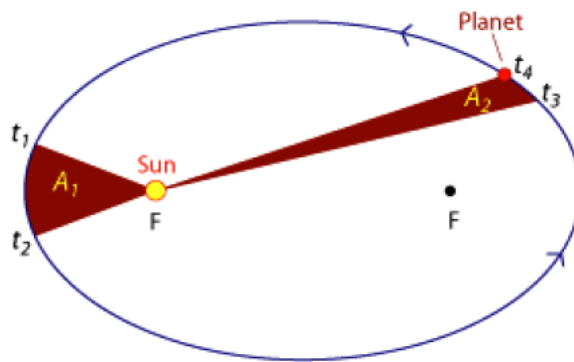


Figure 3.2: Illustration of Kepler's Second Law.

Most analyses of celestial and satellite orbits are based on Newton's laws, which describe gravitational attraction between bodies with mass. These laws are stated in [6]:

- **FIRST LAW (INERTIA)** - Every body continues in a state of rest or uniform motion in a straight line, unless it is compelled to change that state by a force imposed on it.
- **SECOND LAW (CHANGING MOMENTUM)** - When a force is applied to a body, the time rate of change of momentum is proportional to, and in the direction of, the applied force.
- **THIRD LAW (ACTION-REACTION)** - For every action there is a reaction that is equal in magnitude but opposite in direction to the action.

- LAW OF UNIVERSAL GRAVITATION - Every particle in the universe attracts every other particle with a force that is proportional to the product of the masses and inversely proportional to the square of the distance between the particles.

3.2.1 Two-Body Equation

3.2.1.1 Assumptions

In developing the two-body equation, certain assumptions are made [4]:

1. The bodies of the satellite and attracting body are spherically symmetrical with uniform density, hence can be considered as point masses.
2. The coordinate system chosen for a particular problem is inertial. The geocentric equatorial system serves for satellites orbiting the Earth.
3. No external forces act on the system except for the gravitational forces that act along a line joining the centers of the two bodies.

3.2.1.2 Equation of Relative Motion

Consider a system of two bodies of masses m and M , as illustrated in Figure 3.3. Their position vectors with respect to an inertial frame are \mathbf{R}_m and \mathbf{R}_M . By applying Newton's law of gravitation (Appendix A), it can be shown that [3]

$$\ddot{\mathbf{R}} = -\frac{G(M+m)}{R^3}\mathbf{R}, \quad (3.1)$$

where,

$\mathbf{R} = \mathbf{R}_m - \mathbf{R}_M$, Position of body m relative to M ,

G = Gravitational constant, $6.672 \times 10^{-11} m^3 kg^{-1} s^{-2}$,

M = Mass of the Earth, $5.9742 \times 10^{24} kg$,

m = Mass of satellite,

R = Magnitude of position vector \mathbf{R} .

The gravitational parameter (μ), is defined as $\mu = G(M+m) \approx GM$. The principal mass M , is assumed fixed in inertial space. When $m \ll M$, Equation (3.1), reduces to the

restricted 2-body problem given as [3]

$$\ddot{\mathbf{R}} + \frac{\mu}{R^3}\mathbf{R} = 0, \quad (3.2)$$

Equation (3.2) is known as the Two-Body equation of motion which gives the motion of a satellite position of mass, m , as it orbits the Earth.

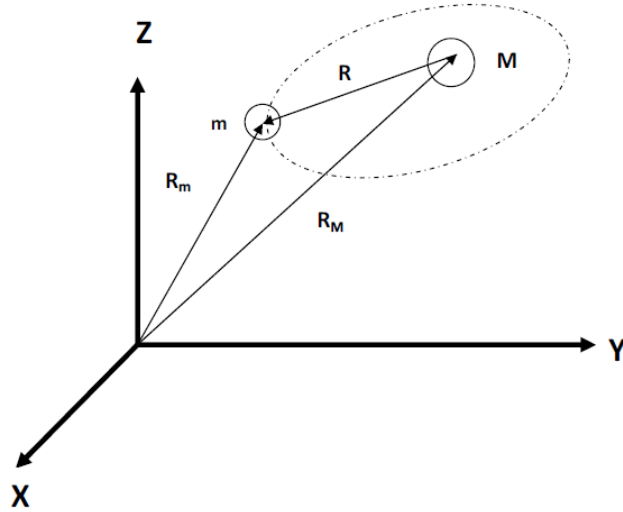


Figure 3.3: Two-body System adapted from [3].

A solution to Equation (3.2) for a satellite orbiting the Earth is the polar equation of a conic section, which gives the magnitude of the position vector in terms of the location in the orbit [5] as illustrated in Figure 3.4,

$$R = \frac{a(1 - e^2)}{1 + e \cos \nu}, \quad (3.3)$$

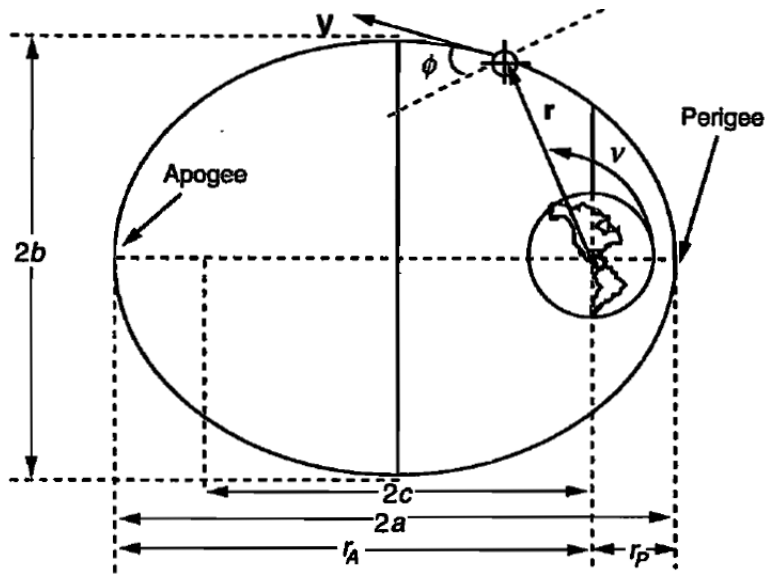
where,

a = Semi-major axis,

e = Eccentricity,

ν = Polar angle or true anomaly.

Two-body motion, however, is not sufficiently accurate in describing orbital motion and improved propagating accuracy is obtained by including additional forces acting on the satellite. These forces including atmospheric drag, Earth's aspherical gravity attraction, planetary attraction, solar radiation pressure, Sun, Moon causes a departure from the two-body motion.



$v =$ true anomaly, $r = R =$ position vector of the satellite relative to Earth's centre, $V =$ velocity vector of the satellite relative to Earth's center, $\phi =$ flight path angle.

Figure 3.4: Position vector of satellite in orbit [30].

The two-body motion is a special case of the *N-Body problem*. Consider a system of N -bodies ($m_1, m_2, m_3, \dots, m_N$), the total acceleration of the, i^{th} , body, m_i , due to gravitational attraction from the N -bodies is given as [6]

$$\ddot{\mathbf{R}}_i = -G \sum_{j=1, \neq i}^N \frac{m_j}{R_{ji}^3} \mathbf{R}_{ji}, \quad (3.4)$$

where,

$\ddot{\mathbf{R}}_i =$ Acceleration vector of the, i^{th} , body,

$G =$ Gravitational constant,

$\mathbf{R}_{ji} = \mathbf{R}_i - \mathbf{R}_j$.

The vector sum of all gravitational and other external forces acting on m_i determines its motion. Combining Newton's law of universal gravitation and second law of motion renders [6]

$$\ddot{\mathbf{R}}_i = -G \sum_{j=1, \neq i}^N \frac{m_j}{R_{ji}^3} \mathbf{R}_{ji} + \frac{1}{m_i} (-\dot{\mathbf{R}}_i \dot{m}_i + \mathbf{F}_{Drag} + \mathbf{F}_{Thrust} + \mathbf{F}_{SUN} + \mathbf{F}_{MOON} + \mathbf{F}_{other}). \quad (3.5)$$

Equation (3.5) is a second order, non-linear, vector differential equation describing the equation of motion of a body influenced by gravitational and other external forces.

The *N-body problem* is a coupled second order differential equation which has to be solved numerically by numerical integration using high-order numerical integrators such as Runge-Kutta, Adams-Bashforth-Moulton, Gauss-Jackson [4] etc. to achieve precision and medium term orbit propagation results. However, this is not the scope of the study and hence will not be addressed in detail.

SALT utilises the effect of Earth's aspherical gravity and atmospheric drag, hence these perturbations will be discussed in detail in Chapter 4.

3.2.2 Constants of Motion

Orbital motion occurs in a conservative gravitational field which explains why satellites conserve mechanical energy and angular momentum.

3.2.2.1 Energy Law

The energy constant of motion is obtained by scalar multiplication of Equation (3.2) by $\dot{\mathbf{R}}$. After some manipulation, the conservation of energy, namely the specific mechanical energy (Appendix A) is found as [5]:

$$\frac{V^2}{2} - \frac{\mu}{R} = \varepsilon = \text{constant}, \quad (3.6)$$

with,

$$\varepsilon = \text{Satellite's specific mechanical energy} = -\frac{\mu}{2a} \text{ (km}^2/\text{s}^2\text{)},$$

$$V = \text{Satellite's velocity (km/s)},$$

$$\mu = \text{Gravitational parameter (km}^3/\text{s}^2\text{)},$$

$$R = \text{Satellite's distance from Earth's centre (km)}.$$

The relative kinetic energy per unit mass is $\frac{V^2}{2}$ and $-\frac{\mu}{R}$ is the potential energy per unit mass of a satellite. The total mechanical energy per unit mass (ε), is the sum of the kinetic and potential energies per unit mass. Because ε is conserved, it must be the same at any point along an orbit. Specific mechanical energy (ε) is dependent on position (R), velocity (V) and the local gravitational parameter (μ). Hence if the position and velocity of a satellite along any point on the orbit is known, the specific mechanical energy at every point on its orbit is also known. Equation (3.6) is also referred to as the *energy integral* or the *vis – viva* equation. It is valid for all trajectories, including rectilinear ones.

3.2.2.2 Angular Momentum

Angular momentum is very useful in determining and maintaining the satellite's orbit. The angular momentum constant of motion for a satellite is the result of the cross product between the position and velocity vectors. This is evaluated by cross-multiplying Equation (3.2) by \mathbf{R} (Appendix A). The resultant is the specific angular momentum \mathbf{h} , given as [5]

$$\mathbf{h} = \mathbf{R} \times \mathbf{V}, \quad (3.7)$$

where

- \mathbf{h} = Satellite's specific angular momentum vector (km^2/s),
- \mathbf{R} = Satellite's position vector (km),
- \mathbf{V} = Satellite's velocity vector (km/s).

The angular momentum vector (\mathbf{h}) is always perpendicular to (\mathbf{R}) and (\mathbf{V}), which defines the orbital plane. Thus if \mathbf{h} is at right angles to the orbital plane and it is a constant, then the orbital plane must also be constant. In Equation (3.2) the orbital plane is forever frozen in inertial space. In reality, due to orbit perturbations, the orbital plane changes gradually over time.

3.2.2.3 Trajectory Equation

The trajectory equation presents a great insight into orbital motion, thus describing the dimensions and shape of the orbit. By writing equation (3.2) into the specific angular momentum vector \mathbf{h} and evaluating, we find the actual solution for a satellite's motion in polar coordinates as Equation (3.3) [4] with $p = a(1 - e^2)$, where p is the semiparameter and e the eccentricity which defines the shape of the orbit as shown in the Table 3.1. The trajectory equation doesn't restrict the motion of an ellipse, hence it's an extension of Kepler's first law as stated above.

Table 3.1: Relationship between conic section and eccentricity.

Conic Section	Eccentricity (e)
Circle	$e = 0$
Ellipse	$0 < e < 1$
Parabola	$e = 1$
Hyperbola	$e > 1$

3.3 Satellite State

Six quantities describe the *orbit* of a satellite, three each for position and velocity in a cartesian coordinate system or an element set, typically used with scalar magnitude and angular representation of the classical or Kepler orbital elements¹. A state vector is usually obtained from numerically integrating the equations of motion, which are described by the coupled 2nd order differential equations.

3.3.1 Classical Orbit Parameters

The Keplerian orbital elements (Figures 3.4 and 3.5) are often referred to as classical or conventional elements. This set of orbital elements can be divided into two groups, namely: dimensional and orientational elements. Dimensional elements specify the size and shape of the orbit and relate the position in the orbit to time, whereas orientational elements specify the position of the orbit in inertial space. All but one quantity varies slowly with time (the True Anomaly varies proportionally with time) [3].

- Semi-major Axis (a): defines the size of the orbit.
- Eccentricity (e): defines the shape of the orbit.
- Inclination (i): vertical tilt of the orbital plane with the unit vector in the $Z - axis$ with respect to the equatorial plane.
- Right Ascension of Ascending Node (Ω): angle between the vernal equinox (Υ)² vector and the ascending node (N). The ascending node is the point where a satellite passes through the equatorial plane moving from South to North.
- Argument of Perigee (ω): angle from the ascending node to the orbital eccentricity vector. The eccentricity vector points from the Earth's centre to perigee with a magnitude equal to the eccentricity.
- True Anomaly (ν): angle from the eccentricity vector to the satellite position vector. Mean anomaly (M) and eccentric anomaly (E) are also used in calculation of orbit parameters.

The first two elements define the shape and size of the ellipse (Figure 3.4). The parameters, i and Ω define the orientation of the orbital plane with respect to the coordinate system

¹The derivation of these orbital elements can be found in most works on celestial mechanics.

²Vernal equinox - It is a point on the intersection of the celestial plane and the ecliptic.

[3]. The last two elements define the position of the satellite on the orbital plane as in Figure 3.5.

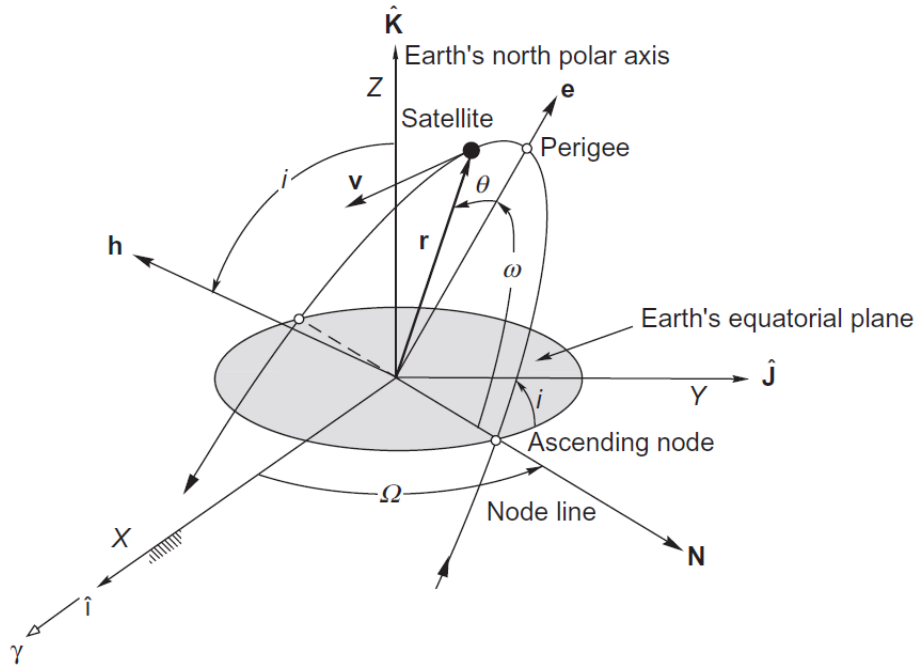


Figure 3.5: Classical orbit elements [55].

A summary of some parameters defining the geometry of an ellipse is given in Table 3.2.

Table 3.2: Parameters defining an ellipse [4].

Element	Symbol	Equation
Semi major axis	a	$a = \frac{r_a + r_p}{2}$
Semi minor axis	b	$b = \sqrt{a^2(1 - e^2)}$
Eccentricity	e	$e = \frac{r_a - r_p}{r_a + r_p}$
Apogee radius	r_a	$r_a = a(1 + e)$
Perigee radius	r_p	$r_p = a(1 - e)$
Semiperimeter	p	$p = a(1 - e^2)$
Mean motion	n	$n = \sqrt{\frac{\mu}{a^3}}$
Orbital period	P	$P = \frac{2\pi}{n}$

The orbital elements contain the same information as the position and velocity vectors at a specific time. Assuming \mathbf{R} and \mathbf{V} are known, as illustrated in Table 3.3, the orientation of the orbit in space can be visualised by changing from one set of coordinates to the other.

Table 3.3: Transforming position and velocity vectors to Kepler elements [4].

Element	Equation	Remark
Semi-major axis	$a = \left(\frac{2}{R} - \frac{v^2}{\mu} \right)^{-1}$	
Semi-perimeter	$p = \frac{h^2}{\mu}$	h = specific angular momentum $\mu = GM$
Eccentricity	$\mathbf{e} = \frac{\mathbf{V} \times \mathbf{h}}{\mu} - \frac{\mathbf{R}}{R}$	\mathbf{h} = angular momentum vector normal to the orbital plane
Nodal vector	$\mathbf{n} = \hat{\mathbf{K}} \times \mathbf{h}$	$\hat{\mathbf{K}}$ = unit vector normal to Earth equatorial plane
Inclination	$i = \cos^{-1} \left(\frac{\hat{\mathbf{K}} \cdot \mathbf{h}}{Kh} \right)$	$0 \leq i \leq 180^\circ$ h = magnitude of \mathbf{h} K = magnitude of $\hat{\mathbf{K}}$
Right ascension of the ascending node	$\Omega = \cos^{-1} \left(\frac{\hat{\mathbf{I}} \cdot \mathbf{n}}{In} \right)$	$n_J \geq 0$, then $0 \leq \Omega \leq 180^\circ$ *, $n_J < 0$, then $180^\circ < \Omega < 360^\circ$ $\hat{\mathbf{I}}$ = unit vector in the principal direction (vernal equinox) I = magnitude of $\hat{\mathbf{I}}$
Argument of perigee	$\omega = \cos^{-1} \left(\frac{\mathbf{n} \cdot \mathbf{e}}{ne} \right)$	$e_K \geq 0$, then $0 \leq \omega \leq 180^\circ$ † $e_K < 0$, then $180^\circ < \omega < 360^\circ$
True anomaly	$\nu = \cos^{-1} \left(\frac{\mathbf{e} \cdot \mathbf{R}}{eR} \right)$	$\mathbf{R} \cdot \mathbf{V} \geq 0$, then $0 \leq \nu \leq 180^\circ$ $\mathbf{R} \cdot \mathbf{V} < 0$, then $180^\circ < \nu < 360^\circ$ \mathbf{R} = position vector R = magnitude of \mathbf{R}

* $n_J = J$ component of the nodal vector, † $e_K = K$ component of the eccentricity vector. J and K components determine which quadrants Ω and ω lie respectively.

3.4 Coordinate Systems and Transformations

Relevant coordinate systems are always defined for space mission geometry problems in order to describe the motion of a satellite. This section discusses the Earth Centred Inertial (ECI), Earth Centred Earth Fixed (ECEF) and some other common reference systems used in this study. The transformation matrices used to convert coordinates from one reference system to another are also presented. The Earth's centre is usually chosen as the origin for most orbital mechanics applications. For some applications, such as remote sensing, the satellite's centre is chosen to view the relative motion and position with respect to the centre as observed from its reference frame, or for analysis of payload observations [30].

3.4.1 Reference Systems

3.4.1.1 Earth Centred Inertial (ECI) System

The ECI system is a non-rotating reference frame assumed to be fixed in space. Its origin is centred at Earth. The positive X -axis is aligned with the Earth's equator and pointing to vernal equinox (Υ). The Z -axis is directed along the celestial North Pole (Earth's North Pole for J2000³) perpendicular to the celestial equatorial plane (Earth equatorial plane for J2000) with the Y -axis completing the right hand system. The position and velocity vectors, denoted by \mathbf{R} and \mathbf{V} respectively, as well as the right ascension α_r and the declination δ_d , are illustrated in Figure 3.6. The α_r is measured from the vernal equinox to the projection of \mathbf{R} onto the equatorial plane and δ_d is measured from the same projection to \mathbf{R} [31]. The ECI coordinates are frequently called GCI (Geocentric Inertial). This system is used extensively in orbit analysis and in some aspects of astronomy.

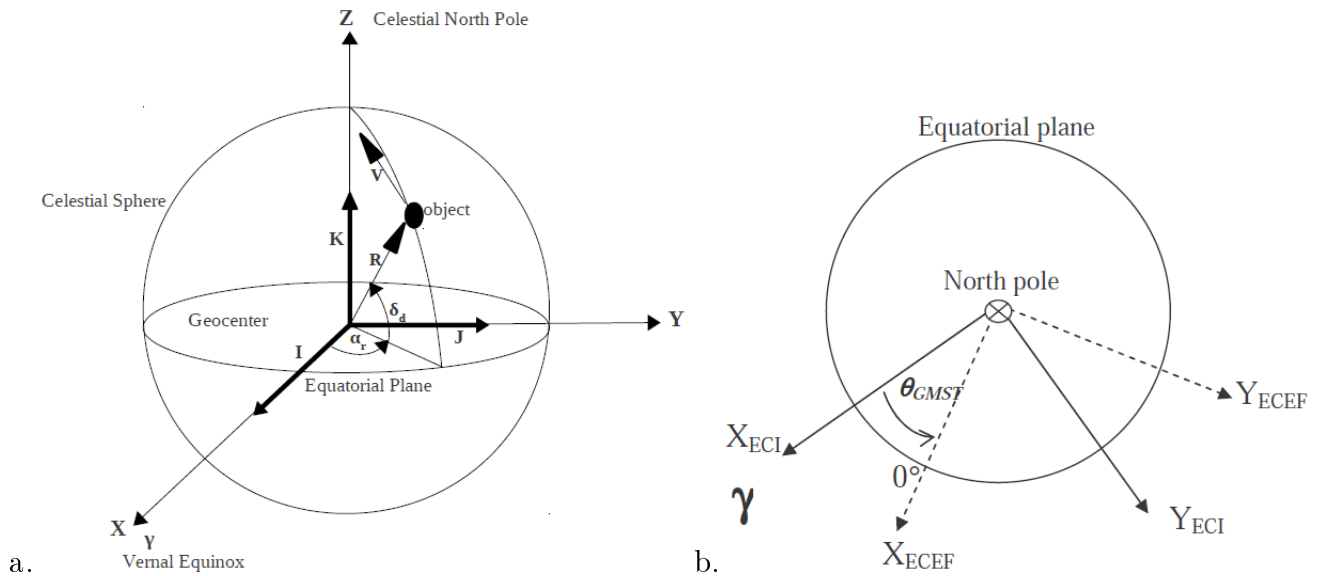


Figure 3.6: (a) Earth Centred Inertial (ECI) Reference Frame. (b) ECEF and ECI frames related by changing sidereal time θ .

3.4.1.2 Earth Centred Earth Fixed (ECEF) System

The origin of the ECEF system is in the geo-centre of the Earth. The Z -axis is defined along the Earth's rotational axis, pointing towards the Earth's North Pole. The X -axis, is along the line joining the geo-centre with the intersection of the Earth's equatorial plane and the Greenwich meridian. The Y -axis, is advanced 90° from the X -axis in the Earth's

³Julian year 2000 used to describe the time-dependent orientation of the equator and ecliptic, thus the standard reference frame based on the mean equator, ecliptic and equinox of a fixed epoch.

equatorial plane. The ECEF coordinate rotates with the Earth about its rotation axis [4]. It's very useful in processing satellite observations from a site and conversion of actual observations to the J2000 system for use in other calculations. The ECEF and ECI frames are related through the Greenwich mean sidereal time θ_{GMST} as in Figure 3.6b.

3.4.1.3 Geographic Co-ordinates

The geographical position of any point on the Earth's surface is best described in terms of its latitude (ϕ) and longitude (λ). The origin of the geographic coordinate system is the intersection of the equator and the prime meridian (Greenwich). The geodetic latitude (ϕ) is the angle between the normal and the equatorial plane while the geocentric latitude (ϕ') is the angle between the equatorial plane and the radius from the center to a point on the surface as shown in Figure 3.7b. Geodetic longitude is the angular distance between the prime meridian and another meridian passing through a point on the Earth's surface. Because the vertex of the angle is the centre of the Earth, the same applies for geocentric longitudes. Latitudes and longitudes are measured in degrees with $\phi \in [-90^\circ, 90^\circ]$ and $\lambda \in [-180^\circ, 180^\circ]$. Values for longitude are negative west of Greenwich and values for latitude negative south of the equator.

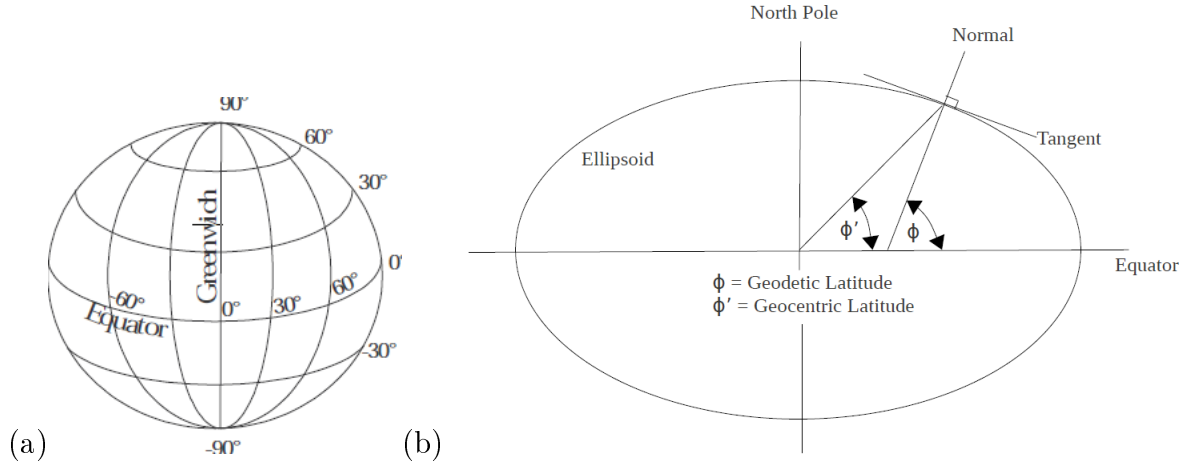


Figure 3.7: (a) Geographic coordinates [12]. (b) Illustration of Geodetic and Geocentric latitudes.

3.4.1.4 Perifocal Coordinate System

The fundamental plane is the satellite's orbit and the origin is at the Earth's centre. The principal axis, X_ω , points in the direction of perifocus, the Y_ω - axis is 90° advanced from perifocus in the direction of satellite movement and the Z_ω - axis is normal to the orbital plane [6]. The perifocal system always maintains orientation towards perigee and does

not rotate with the satellite. It is well suited for orbits with a well-defined eccentricity. The position of the orbit plane in space is defined by the three classical orientation angles, inclination (i), argument of perigee (ω) and longitude of ascending node (Ω).

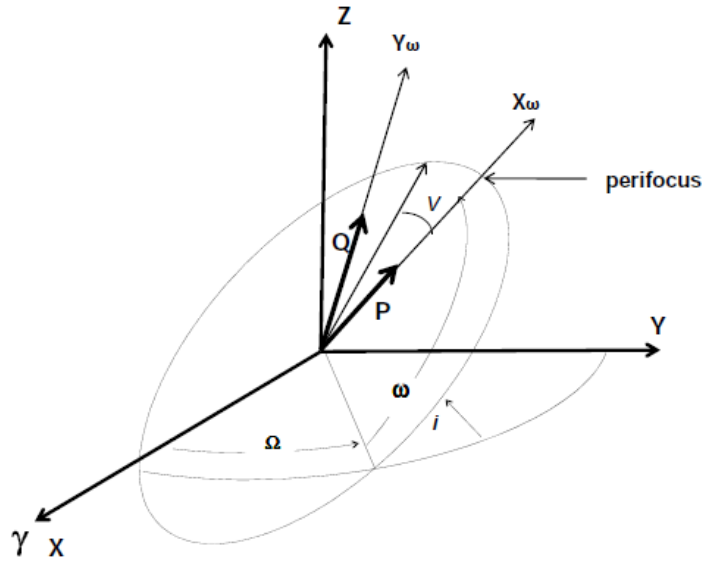


Figure 3.8: A perifocal coordinate system adapted from [34].

3.4.2 Coordinate Transformations

A coordinate rotation merely changes the vector's coordinate frame. The vector therefore has the same length and direction after the rotation and still represents the same quantity, but the three vector components differ.

3.4.2.1 Transformation from ECEF to ECI

The rotation of the ECEF coordinate system relative to the ECI coordinate system is the rotation about their coincident Z -axis, equal to the angle $\theta_{GMST} = \theta_{GMST,2000} + \omega_{\oplus}t^4$. The conversion between the two coordinate systems is given by the following matrix [4]:

$$\mathcal{M}_{ECEF \rightarrow ECI} = \begin{bmatrix} \cos(\theta_{GMST}) & -\sin(\theta_{GMST}) & 0 \\ \sin(\theta_{GMST}) & \cos(\theta_{GMST}) & 0 \\ 0 & 0 & 1 \end{bmatrix}, \quad (3.8)$$

⁴ $GMST$ = Greenwich Mean Sidereal Time, ω_{\oplus} = Earth rotation rate, t = elapsed time (seconds) since ECEF and ECI frames were separated by an angle of $\theta_{GMST,2000}$. Value taken on 1 January 2000, 00 : 00 : 00 UTC.

where, $\omega_{\oplus} = 7.2921158553 \times 10^{-5} \text{ rad/s}$,

$$\theta_{GMST,2000} = 1.74476716333061 \text{ rad}.$$

This conversion assumes that any precession, nutation and polar motion effects are neglected. The same procedure is used for the inverse transformation, but with using the transpose of the rotation matrix given above as it's an orthonormal matrix for which the inverse equals the transpose.

3.4.2.2 Transformation between Perifocal Coordinates and ECI

The transformation from perifocal to ECI coordinate system can be used to find \mathbf{R} and \mathbf{V} of a satellite in the ECI system. Assuming a satellite is rotating in a counterclockwise direction when viewed from Earth's North Pole, then the transformation from perifocal to ECI can be made using three consecutive clockwise rotations by Euler angles⁵ conforming to the 3–1–3 sequence (Figure 3.9). The rotation sequence follows as [31]

1. rotation about \hat{h} mapping \hat{e} onto \hat{I} , $0 \leq \omega \leq 2\pi$,
2. rotation about \hat{I} mapping \hat{h} onto \hat{z} , $0 \leq i \leq \pi$,
3. rotation about \hat{z} mapping \hat{I} onto \hat{x} , $0 \leq \Omega \leq 2\pi$.

The composite rotation transforming a vector from perifocal to ECI coordinate system is given as

$$R_{perifocal}^{ECI}(\omega, i, \Omega) = R_3(\Omega, \hat{z})R_2(i, \hat{I})R_1(\omega, \hat{h}). \quad (3.9)$$

Evaluating (3.9) gives the Direction Cosine Matrix (DCM)⁶ [31]

$$R_{perifocal}^{ECI}(\omega, i, \Omega) = \begin{bmatrix} c(\Omega)c(\omega) - s(\Omega)s(\omega)c(i) & c(\Omega)s(\omega) + s(\Omega)c(\omega)c(i) & s(\Omega)s(i) \\ -s(\Omega)c(\omega) - c(\Omega)s(\omega)c(i) & -s(\Omega)s(\omega) + c(\Omega)c(\omega)c(i) & c(\Omega)s(i) \\ s(\omega)s(i) & -c(\omega)s(i) & c(i) \end{bmatrix}, \quad (3.10)$$

where $c = \cos$ and $s = \sin$.

The inverse transformation i.e. from ECI to perifocal system can be obtained using the inverse (transpose) of the DCM above.

⁵Euler theorem - the most general displacement of a rigid body with one point fixed is a rotation about some axis.

⁶DCM expresses one set of orthonormal basis vectors in terms of another set, or expresses a known vector in a different basis.

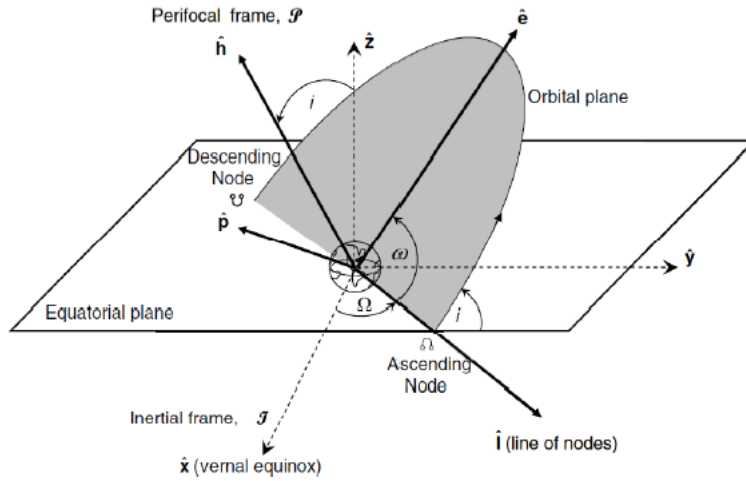


Figure 3.9: Transformation from perifocal to ECI co-ordinate system using the three Euler angles ω , i , Ω [31].

3.4.2.3 Position and Velocity from Orbital Elements

The position \mathbf{R} and velocity \mathbf{V} vectors are first expressed in the perifocal coordinate system and then transformed to the geocentric equatorial frame or ECI. Now, \mathbf{R} can be expressed in terms of the perifocal system (Figure 3.8) as [6]

$$\mathbf{R} = R \cos \nu \mathbf{P} + R \sin \nu \mathbf{Q}, \quad (3.11)$$

where the scalar magnitude R can be obtained from equation (3.3) and \mathbf{P} , \mathbf{Q} (perifocal system) are unit vectors in the direction of X_ω , Y_ω respectively with $Z_\omega = 0$. The velocity vector \mathbf{V} , is found by differentiating (3.11) to obtain

$$\mathbf{V} = \dot{\mathbf{R}} = (\dot{R} \cos \nu - R \dot{\nu} \sin \nu) \mathbf{P} + (\dot{R} \sin \nu + R \dot{\nu} \cos \nu) \mathbf{Q}. \quad (3.12)$$

Equation (3.12) can be simplified by recognising $h = R^2 \dot{\nu}$ and $p = \frac{h^2}{\mu}$ and further differentiating (3.5) to obtain

$$\dot{R} = \sqrt{\frac{\mu}{p}} e \sin \nu, \quad (3.13)$$

and

$$R \dot{\nu} = \sqrt{\frac{\mu}{p}} (1 + e \cos \nu). \quad (3.14)$$

Substituting these results in (3.12) yields [6]

$$\mathbf{V} = \sqrt{\frac{\mu}{p}}[-\sin \nu \mathbf{P} + (e + \cos \nu) \mathbf{Q}]. \quad (3.15)$$

The transformation from perifocal to geocentric equatorial frame or ECI is as illustrated in subsection 3.4.2.2.

3.5 Two-Line Element Sets

Accurate observations of a satellite's position and velocity at any given time is required to manage operations such as space debris monitoring, lifetime predictions and space debris mitigation successfully.

The classical orbital elements are widely used throughout the scientific community, but they are not universally available for all satellites. The standard format for communicating the orbit of an Earth-orbiting satellite is the Two-Line Element (TLE) set. Satellite data for various spacecraft are available to the public in the form of TLE's. These are provided by NASA/Goddard Space Flight Center (GSFC) and published on the internet by *Celestrak* [10] or *Space-Track* [11]. Although these elements are supplied as classical orbit elements, they are actually Kozai *mean* elements⁷ [4]. Public domain software is available for propagation of these elements, the most common being the SGP4 propagator. Although ten values are listed in a TLE file, the first six represent the independent quantities required for calculations while the remaining variables (mean motion rate, mean motion acceleration, and B^* , a drag-like parameter) are required to describe the effect of perturbations on satellite motions, which will be discussed in Chapter 4.

The first SUNSAT TLE looks as follows:

```
1 25635U 99008B 99068.23100837 .00000196 00000-0 61890-4 0 482
2 25635 96.4768 19.8698 0151917 209.5613 149.6933 14.40791150 1989
```

Using the TLE format description (Appendix B), the data translates to [4]

Epoch: March 9 1999, 05:32:39.12 UTC

$$\bar{n} = 14.40791150 \text{ rev/day,}$$

⁷Kozai mean elements - Only the short period terms (i.e. those involving averaging over the period of the orbit) are considered. The only perturbation force considered is the oblateness arising from the J₂ gravity term.

$$\begin{aligned}\frac{\dot{n}}{2} &= 1.96 \times 10^{-6} \text{ rev/day}^2, \quad \frac{\ddot{n}}{6} = 0.0 \text{ rev/day}^3, \\ B^* &= 6.1890 \times 10^5, \\ e &= 0.0151917, \\ i &= 96.4768^\circ, \\ \Omega &= 19.8698^\circ, \\ \omega &= 209.5613^\circ, \\ M &= 149.6933^\circ.\end{aligned}$$

The true *ballistic coefficient* BC, is obtained from B^* with a constant conversion of [32]

$$\text{BC} = \frac{1}{12.74162B^*} \text{kg.m}^{-2}.$$

However, the value of B^* is always modified. It is an arbitrary free parameter in the differential correction [4].

3.6 Summary

The equations described in this chapter exemplifies the two-body problem, though not sufficiently accurate for satellite ephemerides or for calculations which requires precise knowledge of the satellite's position or velocity. However, they are accurate enough to estimate overall mission characteristics in most regions of space.

The requirement for describing an orbit is to define a suitable reference frame, thus finding an appropriate inertial coordinate system. A description of the coordinate frames used in this study is presented. The position of the satellite is best described in terms of the Earth Centred Inertial (ECI) frame. The different transformation matrices needed to convert from one coordinate frame to the other is addressed. Data in the form of TLE's obtained from [10, 11] are used extensively in this study, hence a description of the two-line element set is presented and further explained in Appendix B.

The following chapter describes the importance of SALT and its application in LIFTIM for this study. The equations of motion and the perturbative effects on the orbital elements are presented.

Chapter 4

Orbit Perturbations and Decay Employed in SALT

4.1 Introduction

Analytic solutions which describes the effect of atmospheric drag on the motion of artificial satellites exist. But these solutions are usually based on simplified analytical models for the atmospheric density and also have some limitations on the size of the eccentricity and/or the perigee height due to the use of series expansions. Semi-analytical theories have been developed and are been used, but most of these theories just emphasise on long-term predictions without numerical examination for high-drag test cases [4].

The Semi Analytical Liu Theory (SALT) accounts for the effects of atmospheric drag on the motion of artificial satellites in the presence of the gravitational field of an oblate Earth. It uses a combination of general and special perturbation techniques, which estimate the decay history or lifetime (long-term predictions) and generate short-term orbital ephemerides for close-Earth satellites perturbed by atmospheric drag and Earth oblateness. The efficiency of SALT enhances the use of analytical techniques which make use of sufficient numerical methods permitting the inclusion of a state-of-the-art atmospheric density model without series expansions [51].

The numerical inefficiencies created by the fast dynamical variations with periods on the order of one orbit is treated by the average variational equations. These are based on the use of transformations which allow the system of differential equations for the osculating state to be transformed into a system for propagation of the mean state [52].

Predicting orbital motion of a satellite is difficult due to the fact that, several characteristics of the satellite and the atmosphere are not deterministically known. Predictions generated by SALT avoids this difficulty, by comparing with the numerical integration of the original equations of motion for the osculating state, assuming deterministic or known values for the random variables in the model. Proper initialisation procedures vital to the prediction accuracy exhibits excellent precision as well as large savings in computational time [1].

The approach to the orbital decay prediction problem uses a combination of general and special perturbation techniques. Subsequently, the method of averaging is utilised to obtain the mean elements and expressions for their time rates of change. Time rate of change of the orbital element due to drag is determined by direct numerical integration over the true anomaly using the Gauss-Legendre method, whilst that due to Earth oblateness is solved by analytic expressions [40].

The theory determines the time histories of the semi-major axis (a), argument of perigee (ω), eccentricity (e), and longitude of ascending node (Ω) due to the influence of Earth oblateness and atmospheric drag as dominant perturbative forces. The evolution of the elements is generated until a sufficient altitude decrease (to an altitude $< 90 \text{ km}$) indicates re-entry. Inclination is assumed constant throughout the orbital lifetime. The major perturbative forces responsible for LEO decay which are atmospheric drag and Earth oblateness (only in combination with atmospheric drag, it will contribute to LEO decay) are discussed.

4.2 Perturbation Effects on Orbital Elements

Perturbations on orbital motion result in secular and periodic changes. Variations in the orbital elements are illustrated in Figure 4.1. Secular changes in a particular element vary linearly, or in some cases proportionally to a power of time, such as a quadratic.

Short periodic variations are trigonometric functions of fast varying elements such as true anomaly ν , etc. or linear combinations of ν and ω (argument of perigee). These variations typically repeat in the order of a satellite's period or less [4].

Long periodic variations are trigonometric functions of slow varying argument of perigee (ω) but also most other orbital elements. These effects have cycles considerably longer than one orbital period, thus typically one or two orders of magnitude longer and may be as long as weeks. Variations in orbital elements are classified as in Table 4.1 [33].

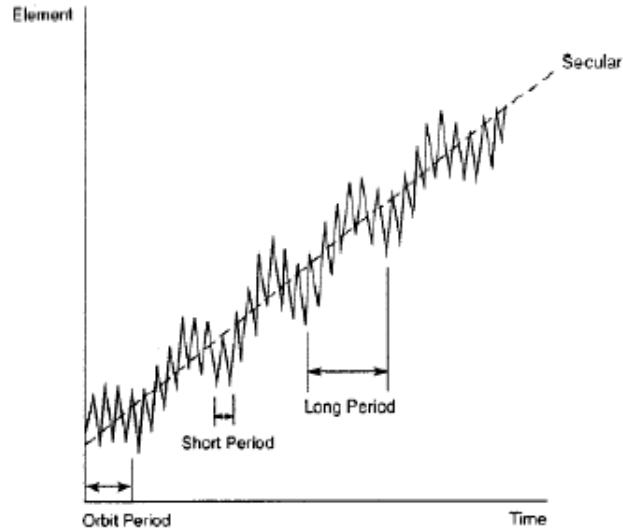


Figure 4.1: General representation of secular and periodic variations of an orbital element [30].

Table 4.1: Perturbing effects on orbital elements.

	Secular		Periodic	
	Large	Small	Moderate	Small
Earth's Oblateness	ω, Ω	-	e	i, Ω, ω
Atmospheric Drag	a, e	i	-	Ω, ω
Sun and Moon	-	Ω, ω	-	a, e, i, ω, Ω
Solar Radiation Pressure	-	-	-	a, e, i, ω, Ω

4.3 Osculating and Mean Elements

Osculating elements are true time-varying orbital elements which include all periodic (short and long) and secular effects. They represent a high precision trajectory and are useful for highly accurate simulations, including real-time pointing and tracking operations.

Long-term behaviour of satellite orbits is best computed by using mean orbit elements rather than the osculating orbit elements. The mean elements are “averaged” over some selected time (or an appropriate angle such as true anomaly), hence they are relatively smoothly varying and are free from short periodic variations. The mean elements depend on an unspecified averaging time interval: the true, eccentric, or mean anomaly, or on the longitude of ascending node. Theories exist for computing mean elements such as those from Kozai [53] and Brouwer [54], but most of these theories strive to evaluate the secular,

short and long periodic variations and should subsequently not be mixed up, as this would lead to unintended results [4].

4.4 Variational Equations of Motion implemented in SALT

The variational equations of motion under the influence of atmospheric drag and Earth oblateness for a LEO satellite can be given in terms of the osculating orbital elements $a, e, i, \omega, \Omega, M$ as [1],

$$\dot{a} = \dot{a}_u + \dot{a}_{ob} + \dot{a}_d, \quad (4.1a)$$

$$\dot{e} = \dot{e}_u + \dot{e}_{ob} + \dot{e}_d, \quad (4.1b)$$

$$\dot{i} = \dot{i}_u + \dot{i}_{ob} + \dot{i}_d, \quad (4.1c)$$

$$\dot{\omega} = \dot{\omega}_u + \dot{\omega}_{ob} + \dot{\omega}_d, \quad (4.1d)$$

$$\dot{\Omega} = \dot{\Omega}_u + \dot{\Omega}_{ob} + \dot{\Omega}_d, \quad (4.1e)$$

$$\dot{M} = \dot{M}_u + \dot{M}_{ob} + \dot{M}_d, \quad (4.1f)$$

with initial conditions $a_o, e_o, i_o, \omega_o, \Omega_o, M_o$ and the subscripts u, ob and d representing the unperturbed, Earth oblateness and drag induced variations respectively.

The osculating orbital elements are transformed to mean orbital elements to obtain the transformed variational equations of motion [1]

$$\dot{a}_m = (\dot{a}_m)_u + (\dot{a}_m)_{ob} + (\dot{a}_m)_d, \quad (4.2a)$$

$$\dot{e}_m = (\dot{e}_m)_u + (\dot{e}_m)_{ob} + (\dot{e}_m)_d, \quad (4.2b)$$

$$\dot{i}_m = (\dot{i}_m)_u + (\dot{i}_m)_{ob} + (\dot{i}_m)_d, \quad (4.2c)$$

$$\dot{\omega}_m = (\dot{\omega}_m)_u + (\dot{\omega}_m)_{ob} + (\dot{\omega}_m)_d, \quad (4.2d)$$

$$\dot{\Omega}_m = (\dot{\Omega}_m)_u + (\dot{\Omega}_m)_{ob} + (\dot{\Omega}_m)_d, \quad (4.2e)$$

$$\dot{M}_m = (\dot{M}_m)_u + (\dot{M}_m)_{ob} + (\dot{M}_m)_d, \quad (4.2f)$$

where subscript m represents the transformed mean equation of motion.

The secular decrease in a and e are the principal effects of the atmospheric drag on LEO satellites, hence the drag effects on the other parameters (i, ω, Ω , and M) are ignored. The simplification is numerically justified because the drag effects are assumed to be of

second-order magnitude, and therefore follows as

$$(\dot{a}_m)_u = (\dot{e}_m)_u = (\dot{i}_m)_u = (\dot{\Omega}_m)_u = (\dot{\omega}_m)_u = 0, \quad (4.3a)$$

$$(\dot{a}_m)_{ob} = (\dot{i}_m)_d = (\dot{\Omega}_m)_d = (\dot{\omega}_m)_d = (\dot{M}_m)_d = 0, \quad (4.3b)$$

$$(\dot{M}_m)_u = n, \quad (4.3c)$$

where n is the satellite's orbit mean motion.

4.5 Effects of Earth Oblateness and Gravity

4.5.1 Non-spherical Gravity Potential

The acceleration of a satellite orbiting a central, spherical symmetric homogeneous mass is given by [34]

$$\ddot{\mathbf{R}}_{2-body} = \nabla \Phi_{2-body}, \quad (4.4)$$

where

$$\nabla \Phi_{2-body} = -\frac{\mu}{R} \mathbf{R}.$$

As the Earth is a non-spherical body which is bulged at the equator, flattened at the poles and generally asymmetric, its asymmetrical mass distribution causes the gravitational field to deviate from the ideal spherical model, and causes periodic variations in the orbital elements. The normalised gravitational coefficients are classified into three groups, viz the zonal, sectorial and tesseral harmonics¹ [4].

From potential theory the gravitational force or acceleration along a given direction is defined as the partial derivative or gradient of a potential (Φ) in that direction. The acceleration of a satellite due to the Earth's non-spherical behaviour can subsequently be obtained by taking the gradient of the potential function Φ_{Earth} given by [4]

$$\ddot{\mathbf{R}} = \nabla \Phi_{Earth}, \quad (4.5)$$

where ∇ is the gradient operator (del).

The potential function Φ_{Earth} is defined by [34]

$$\Phi_{Earth} = \frac{\mu}{r} \left[1 - \sum_{n=2}^{\infty} \left(\frac{R_e}{r} \right)^n \left\{ J_n P_n \sin \varphi - \sum_{m=1}^n J_{nm} P_{nm} \sin \varphi \cos m(\theta - \theta_{nm}) \right\} \right], \quad (4.6)$$

¹Detailed explanation of these harmonics are given in [3,4,6]

with

- r = Geocentric distance.
- φ = Geocentric latitude.
- θ = Geographic longitude.
- θ_{nm} = Equilibrium longitude for J_{nm} .
- R_e = Equatorial radius of the Earth.
- J_{nm} = Harmonic coefficients ($J_n = J_{n0}$).
- μ = Gravitational parameter.
- P_n = Legendre polynomials of degree n and order 0.
- P_{nm} = Associated Legendre polynomial of degree n and order m .

4.5.2 Earth Oblateness

The Earth oblateness is a conservative force, but causes first-order secular and periodic changes in the inertial orientation of a satellite's orbit and thus with respect to the complex non-spherical Earth atmosphere [1]. The non-spherical Earth causes periodic variations in all the classical orbit elements. The principal effects of the J_2 zonal harmonic are secular motions in Ω, ω and mean anomaly, M . The motion of Ω occurs due to the added attraction of the Earth's equatorial bulge, which introduces a force component towards the equator. The secular motion in ω arises because the force is no longer proportional to the inverse square radius and the orbit is consequently no longer a closed ellipse [3].

Other elements such as a, e, i experience periodic variations only about their mean motions. Analytic expressions are developed for the slow drift of the elements Ω, ω and \mathbf{M} due to the J_2 effects. The J_2 term (in the order of 10^{-3}) as a result of the equatorial bulge, while the J_3 term is due to the "pear shape" of the Earth, will cause very small short-periodic perturbations. The values of J_2, J_3 and J_4 as used in SALT are

$$J_2 = 1.08263 \times 10^{-3},$$

$$J_3 = -2.54 \times 10^{-6},$$

$$J_4 = -1.58 \times 10^{-6}.$$

The transformed mean equations of motion as a result of the Earth's oblateness are obtained by substituting equations (4.3a) and (4.3b) into equations (4.2a–4.2f) which yields [1]

$$\begin{aligned}
(\dot{e}_m)_{ob} = & -\frac{3}{2}nJ_2^2 \left(\frac{R_e}{p}\right)^4 \sin^2 i \cdot (14 - 15 \sin^2 i) \cdot e \cdot (1 - e^2) \cdot \sin 2\omega \\
& -\frac{3}{8}nJ_3 \left(\frac{R_e}{p}\right)^3 \sin i \cdot (4 - 5 \sin^2 i) \cdot (1 - e) \cdot \cos \omega \\
& -\frac{15}{32}nJ_4 \left(\frac{R_e}{p}\right)^4 \sin^2 i \cdot (6 - 7 \sin^2 i) \cdot e \cdot (1 - e^2) \cdot \sin 2\omega.
\end{aligned} \tag{4.7a}$$

$$\begin{aligned}
(\dot{i}_m)_{ob} = & \frac{3}{64}nJ_2^2 \left(\frac{R_e}{p}\right)^4 \sin 2i \cdot (14 - 15 \sin^2 i) \cdot e^2 \cdot \sin 2\omega \\
& +\frac{3}{8}nJ_3 \left(\frac{R_e}{p}\right)^3 \cos i \cdot (4 - 5 \sin^2 i) \cdot e \cdot \cos \omega \\
& +\frac{15}{64}nJ_4 \left(\frac{R_e}{p}\right)^4 \sin 2i \cdot (6 - 7 \sin^2 i) \cdot e^2 \cdot \sin 2\omega.
\end{aligned} \tag{4.7b}$$

$$\begin{aligned}
(\dot{\omega}_m)_{ob} = & \frac{3}{4}nJ_2 \left(\frac{R_e}{p}\right)^2 (4 - 5 \sin^2 i) \\
& +\frac{3}{4}nJ_2^2 \left(\frac{R_e}{p}\right)^4 \left[12 - \frac{103}{4} \sin^2 i + \frac{215}{16} \sin^4 i + \left(\frac{7}{4} - \frac{9}{8} \sin^2 i - \frac{45}{32} \sin^4 i \right) \cdot e^2 \right. \\
& \quad \left. +\frac{3}{2} \left(1 - \frac{3}{2} \sin^2 i \right) \cdot (4 - 5 \sin^2 i) \sqrt{1 - e^2} \right] \\
& -\frac{15}{32}nJ_4 \left(\frac{R_e}{p}\right)^4 \left[(16 - 62 \sin^2 i + 49 \sin^4 i) + \frac{3}{4} (24 - 84 \sin^2 i + 63 \sin^4 i) \cdot e^2 \right] \\
& +\frac{3}{64}nJ_2^2 \left(\frac{R_e}{p}\right)^4 [-2 (14 - 15 \sin^2 i) \sin^2 i + (28 - 158 \sin^2 i + 135 \sin^4 i) \cdot e^2] \cos 2\omega \\
& +\frac{3}{8}nJ_3 \left(\frac{R_e}{p}\right)^3 \frac{1}{e \sin i} [(4 - 5 \sin^2 i) (\sin^2 i - e^2 \cos^2 i) + 2 \sin^2 i (13 - 15 \sin^2 i) \cdot e^2] \sin \omega \\
& -\frac{6}{32}nJ_4 \left(\frac{R_e}{p}\right)^4 \left[3 \sin^2 i (6 - 7 \sin^2 i) + \frac{1}{2} (-36 + 210 \sin^2 i - 189 \sin^4 i) \cdot e^2 \right] \cos 2\omega.
\end{aligned} \tag{4.7c}$$

$$\begin{aligned}
(\dot{\Omega}_m)_{ob} = & -\frac{3}{2}nJ_2 \left(\frac{R_e}{p}\right)^2 \cos i \\
& -\frac{3}{2}nJ_2^2 \left(\frac{R_e}{p}\right)^4 \cos i \cdot \left[\left(\frac{9}{4} + \frac{3}{2}\sqrt{1-e^2}\right) - \sin^2 i \cdot \left(\frac{5}{2} + \frac{9}{4}\sqrt{1-e^2}\right) + \frac{1}{4} \left(1 + \frac{5}{4}\sin^2 i\right) \cdot e^2 \right] \\
& + \frac{15}{16}nJ_4 \left(\frac{R_e}{p}\right)^4 (4 - 7\sin^2 i) \cdot \cos i \cdot \left(1 + \frac{3}{2}e^2\right) - \frac{3}{16}nJ_2^2 \left(\frac{R_e}{p}\right)^4 \cos i \cdot (7 - 15\sin^2 i) \cdot e^2 \cdot \cos 2\omega \\
& - \frac{3}{2}nJ_3 \left(\frac{R_e}{p}\right)^3 \left(\frac{15}{4}\sin^2 i - 1\right) \cdot e \cdot \cot i \cdot \sin \omega - \frac{15}{16}nJ_4 \left(\frac{R_e}{p}\right)^4 \cos i \cdot (3 - 7\sin^2 i) \cdot e^2 \cdot \cos 2\omega.
\end{aligned} \tag{4.7d}$$

$$\begin{aligned}
(\dot{M}_m)_{ob} = & n + \frac{3}{2}nJ_2 \left(\frac{R_e}{p}\right)^2 \cdot \left(1 - \frac{3}{2}\sin^2 i\right) \cdot \sqrt{1-e^2} \cdot -\frac{15}{8}nJ_2^2 \left(\frac{R_e}{p}\right)^4 \cdot \sqrt{1-e} \\
& \left[\left(-1 + \frac{5}{2}\sin^2 i - \frac{13}{8}\sin^4 i\right) + \frac{1}{2}e^2 \cdot \left(-1 + \sin^2 i + \frac{5}{8}\sin^4 i\right) \right] \\
& + \frac{3}{2}nJ_2^2 \left(\frac{R_e}{p}\right)^4 \left(1 - \frac{3}{2}\sin^2 i\right)^2 (1 - e^2) - \frac{45}{128}nJ_4 \left(\frac{R_e}{p}\right)^4 (8 - 40\sin^2 i + 35\sin^4 i)e^2 \\
& \cdot \sqrt{1-e^2} - \frac{9}{64}nJ_2^2 \left(\frac{R_e}{p}\right)^4 \sin^2 i \cdot (14 - 15\sin^2 i) \cdot e^2 \cdot \sqrt{1-e^2} \cdot \cos 2\omega \\
& + \frac{3}{32}nJ_2^2 \left(\frac{R_e}{p}\right)^4 \sin^2(14 - 15\sin^2 i) \cdot (1 - e^2)^{\frac{3}{2}} \cdot \cos 2\omega \\
& - \frac{3}{8}nJ_3 \left(\frac{R_e}{p}\right)^3 \sin i \cdot (4 - 5\sin^2 i) \cdot \frac{1 - 4e^2}{e} \cdot \sqrt{1-e^2} \cdot \sin \omega \\
& + \frac{15}{64}nJ_4 \left(\frac{R_e}{p}\right)^4 \sin^2 i \cdot (6 - 7\sin^2 i) \cdot (2 - 5e^2) \cdot \sqrt{1-e^2} \cdot \cos 2\omega \\
& + \frac{9}{8}nJ_2^2 \left(\frac{R_e}{p}\right)^4 \frac{1}{\sqrt{1-e^2}} \left\{ \left(3 - \frac{15}{2}\sin^2 i + \frac{47}{8}\sin^4 i\right) + \left(\frac{3}{2} - 5\sin^2 i + \frac{117}{16}\sin^4 i\right) \cdot e^2 \right. \\
& + \frac{1}{8}(1 + 5\sin^2 i - \frac{101}{8}\sin^4 i) \cdot e^4 + \frac{1}{24}\sin^2 i [(70 - 123\sin^2 i)e^2 + 2(28 - 33\sin^2 i)e^4] \\
& \left. \cos 2\omega + \frac{9}{128} \cdot e^4 \sin^4 i \cdot \cos 4\omega \right\}.
\end{aligned} \tag{4.7e}$$

4.6 Atmospheric Drag Effects

The presence of neutral gas molecules and atoms in the Earth's upper atmosphere, produce drag forces that retard a satellite's motion and alter the orbit shape.

Atmospheric drag is the main non-conservative force that acts on a satellite in LEO. Drag acts in the direction opposite to the velocity vector and removes energy from the orbit in the form of friction on the satellite. Furthermore, the decrease in energy causes the orbit to decay until the satellite re-enters the atmosphere. Drag force is the dominating perturbative force during the last few revolutions of a satellite's life. Perturbative effects of drag on a satellite is deemed to be more important than those from the Earth's oblateness regarding the contribution of orbital decay [1].

The acceleration of the satellite due to atmospheric drag can be expressed as [4,33]

$$\mathbf{a}_{\text{drag}} = -\frac{1}{2}\rho\frac{C_D A}{m}v^2\hat{\mathbf{v}} \quad (4.8)$$

where

- ρ = Atmospheric density (kg/m^3),
- C_D = Drag coefficient (dimensionless),
- A = Cross-sectional area (m^2),
- m = Satellite mass (kg),
- v = Velocity magnitude of the satellite relative to the atmosphere (m/s),
- $\hat{\mathbf{v}}$ = Unit vector of satellite's relative atmospheric velocity.

The drag coefficient (C_D) is a dimensionless quantity which reflects the satellite's susceptibility to drag forces. The value of C_D depends on the cross-sectional area, its attitude with respect to the velocity vector and whether it is spinning, tumbling or stabilised [3]. Cross-sectional area (A) is defined to be normal to the satellite's velocity vector. Ballistic coefficient (BC) defined as $\frac{m}{C_D A}$ is the measure of a satellite's response to drag effects. It is also an indication of how fast a satellite will decay. Satellites with a low BC respond quickly to the atmosphere and their orbits tend to decay faster than those with high BC [30].

Drag effects are secular changes mainly in the semi-major axis (a) and eccentricity (e), and to a small degree inclination (i). Periodic changes are experienced in all the orbit elements especially the argument of perigee (ω) and longitude of ascending node (Ω). No analytic drag theory exists due to the intrinsic nature of evaluating the atmospheric

density variations and accurately predicting the drag coefficient [34].

The drag effects in a and e implemented in SALT are given as [1]

$$(\dot{a}_m)_d = -\frac{1}{2\pi} \int_0^{2\pi} B\rho V \frac{a}{1-e^2} \left[1 + e^2 + 2e \cos \nu - \omega_a \cos i \sqrt{\frac{a^3 (1-e^2)^3}{\mu}} \right] dM, \quad (4.9a)$$

$$(\dot{e}_m)_d = -\frac{1}{2\pi} \int_0^{2\pi} B\rho V \left\{ e + \cos \nu - \frac{\omega_a}{2} \frac{r^2 \cos i}{\mu a (1-e^2)} [2(e + \cos \nu) - e \sin^2 \nu] \right\} dM, \quad (4.9b)$$

where

$$B = \text{Inverse ballistic coefficient} = \frac{c_D A}{m_s}, \quad m_s \text{ is the satellite mass,}$$

$$\rho = \text{Atmospheric density,}$$

$$\omega_a = \text{Earth rotational speed,}$$

$$V = \text{Magnitude of satellite's velocity, explicitly given as.}$$

$$V = \sqrt{\frac{\mu}{p}} (1 + e^2 + 2e \cos \nu)^{\frac{1}{2}} \left[1 - \frac{(1 - e^2)^{\frac{3}{2}} \omega_a}{1 + e^2 + 2e \cos \nu} \cos i \right].$$

Subsequently, the perturbing effects can be computed by measuring the drag effects on perigee and apogee, thus [1]

$$(\dot{r}_p)_d = -\frac{1}{2} \int_0^{2\pi} B\rho V \frac{a(1-e^2)}{(1-e^2)} \left\{ 1 + \cos \nu - \frac{r^2 \omega_a \cos i}{\sqrt{\mu a (1-e^2)}} \left[1 + \cos \nu - \frac{e}{2} \sin^2 \nu \right] \right\} dM, \quad (4.9c)$$

$$(\dot{r}_a)_d = -\frac{1}{2} \int_0^{2\pi} B\rho V \frac{a(1-e^2)}{(1+e^2)} \left\{ 1 - \cos \nu - \frac{r^2 \omega_a \cos i}{\sqrt{\mu a (1-e^2)}} \left[1 - \cos \nu + \frac{e}{2} \sin^2 \nu \right] \right\} dM. \quad (4.9d)$$

The integration operations which compute the average drag effects with respect to M from 0 to 2π are evaluated by means of the Gauss-Legendre quadrature. The integration is done over the true anomaly ν instead of the mean anomaly M , and is obtained by the transformation

$$dM = \left(\frac{r}{a}\right)^2 (1 - e^2)^{\frac{1}{2}} d\nu. \quad (4.9e)$$

4.6.1 Evaluating Atmospheric Density

Atmospheric density depends on the chemical properties of atmospheric gases and physical processes governing its dynamics. Though modelling of the forces require detailed knowledge of the interaction of neutral gas as well as charged particles with the different satellite surfaces, the chemical properties of the atmosphere, especially the upper atmosphere, are not accurately known.

The distribution of the chemical constituents [Nitrogen (78%), Oxygen (21%), Carbon dioxide (0.04%), Argon ($\sim 0.9\%$)] in the atmosphere is taken into account during its modelling. Below 100 *km*, the atmospheric species are in a state of turbulent mixing called the homosphere². Molecular dissociation and diffusion leads to an inhomogeneous species distribution in the heterosphere³. Nitrogen is dominant below 170 *km* whereas between 500 – 600 *km*, depending on solar activity, the atmosphere mainly consists of atomic oxygen. In the regime from 600 – 900 *km*, helium dominates followed by atomic hydrogen at higher altitudes [36].

Modelling of the complex properties and dynamics of the Earth's atmosphere is very challenging because of the complex nature of the atmosphere. The density of the upper atmosphere shows significant temporal and spatial variations, hence it is difficult to model and even more so to predict. The density variation exhibits some regularity in response to generally predictable factors such as altitude, solar activity, time of year, time of day and local latitude. Predicting atmospheric density over long periods is arduous because of the difficulty in predicting the solar flux (F10.7) and magnetic indices (A_p). The effect of atmospheric drag is directly related to the atmospheric density and therefore decreases exponentially with the orbit height (Figure 4.2). The densities were obtained from the MSISE model 1990.

Simple models, such as the exponential static model, assumes the density of the atmosphere decays exponentially from the Earth's surface, but does not account for seasonal or diurnal variations. It also lacks the accuracy and sophistication needed for highly accurate studies [33]. More sophisticated atmospheric models (Harris-Priester model, COSPAR International Reference Atmosphere (CIRA) model, Mass Spectrometer Incoherent Scatter (MSIS), Drag Temperature Model (DTM), etc.) have been developed and used to predict the spatial and temporal density variations.

²Zone of the atmosphere where the constituent gases are fairly well mixed-on average the composition is homogeneous throughout.

³Zone of the atmosphere with poor mixing thus, the average composition varies depending on the location within it.

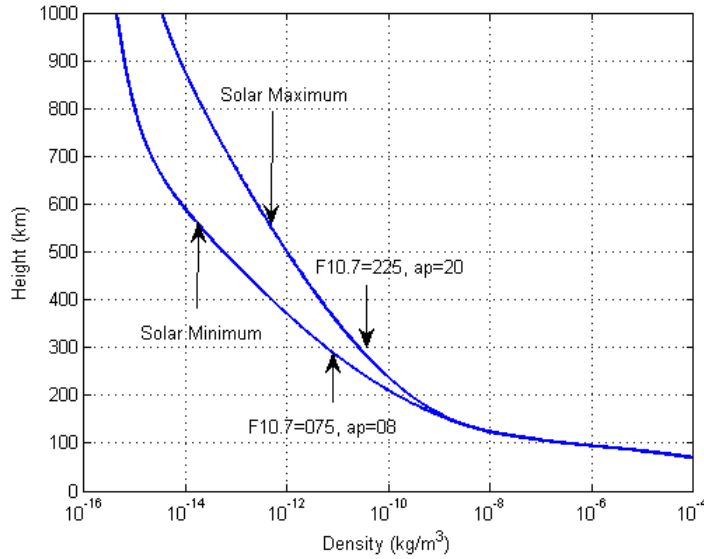


Figure 4.2: Height vs. density for F10.7 values using the MSISE-90 model.

4.6.2 Atmospheric Density Model

The atmospheric density model calculates atmospheric density at three probable solar activity levels, 5% (-2sigma), 50% (nominal) and 95% (+2sigma) over several solar cycles. Atmospheric density is then interpolated from a lookup table as a function of altitude and temperature. The observed [8] and predicted solar flux and magnetic index used to calculate the atmospheric density in this study are shown below (Figures 4.3 and 4.4).

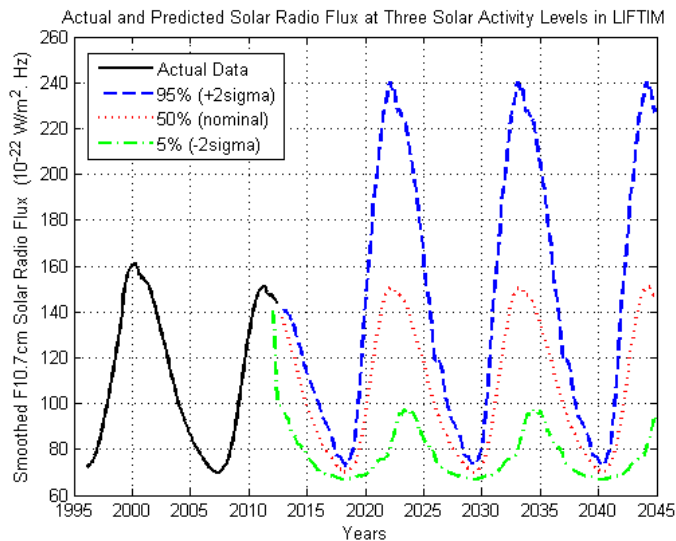


Figure 4.3: Actual (historic) and predicted smoothed monthly mean solar flux values at three activity levels required for predicting the atmospheric density.

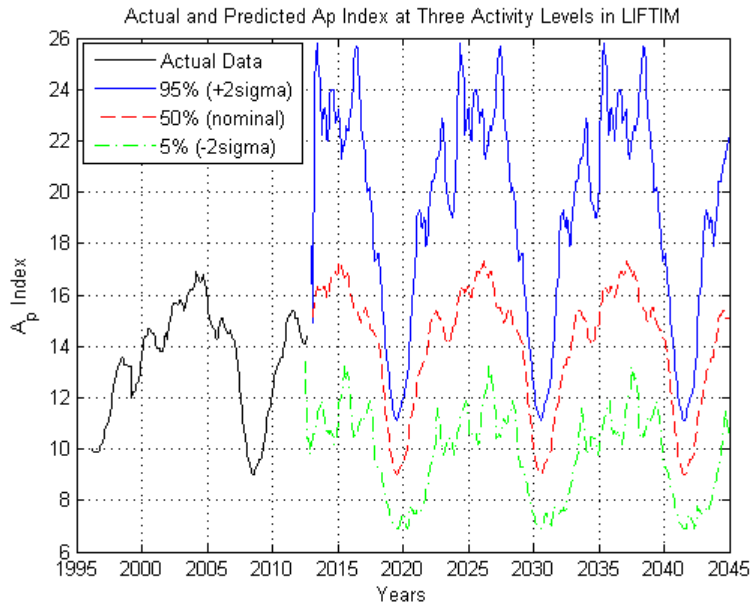


Figure 4.4: Actual (historic) and predicted smoothed monthly mean magnetic index values at three activity levels required for predicting the atmospheric density.

4.7 Implementation of SALT in LIFTIM

The SALT as implemented in LIFTIM utilises the simplified Jacchia 70 model to calculate the atmospheric density. The prediction accuracy of the Jacchia 70 model over existing models is as a result of the differential corrections of the ballistic coefficient, using observed orbit decay data and accurate prediction of orbit decay in a dynamic atmosphere that models the 11 year solar cycle (Jacchia 70 model) [1].

The model provides for density variations due to solar activity and the semi-annual variation, and estimates the accurate exospheric temperature at a given time, together with the satellite's altitude at the point of consideration where the atmospheric density can be properly interpolated [1].

4.7.1 Program Structure and Functionality

The numerical application of SALT as employed in LIFTIM is separated into two parts, each having its own error control. The error control for the differential equations will determine the time step and the quadrature error control will determine the number of true anomaly values for which the integrand of the quadrature will be evaluated. In the decay process, an elliptical orbit ultimately changes to a circular orbit due to drag, hence

two options are required. The elliptical and circular options for the satellite's lifetime. A flow chart showing the functions and subroutines are described in Appendix B. The elliptical option integrates $\dot{r}_a, \dot{\Omega}, \dot{r}_p$ and $\dot{\omega}$, whereas \dot{a} and $\dot{\Omega}$ are integrated in the circular case. The transformation from osculating to mean orbital elements and vice versa is, however, valid for both elliptical and circular orbits.

4.7.1.1 Elliptical Option

The average rate of change in r_a and r_p due to the combined effects of oblateness and drag results in the differential equations of motion given as in [1]

$$\dot{r}_a = (\dot{r}_a)_d + a\dot{e}, \quad (4.10a)$$

$$\dot{r}_p = (\dot{r}_p)_d - a\dot{e}, \quad (4.10b)$$

with $(\dot{r}_a)_d$ and $(\dot{r}_p)_d$ as

$$\begin{aligned} (\dot{r}_a)_d = - & \left[\frac{(1-e^2)^3}{4M\pi n(1-e)^2} \right] \int_{-\pi}^{\pi} \frac{1000c_D A \rho}{(1+e \cos \nu)^3} \left[\frac{n}{\sqrt{1-e^2}} (1+2e \cos \nu + e^2)^{\frac{1}{2}} - \frac{p\omega_a \cos i}{(1+2e \cos \nu + e^2)} \right] \\ & \left[\frac{2n(1+\cos \nu)}{\sqrt{1-e^2}} + \frac{p\omega_a \cos i}{(1-e \cos \nu)} (e \sin^2 \nu - 2 \cos \nu - 2) \right] d\nu, \end{aligned} \quad (4.10c)$$

$$\begin{aligned} (\dot{r}_p)_d = - & \left[\frac{(1-e^2)^3}{4M\pi n(1-e)^2} \right] \int_{-\pi}^{\pi} \frac{1000c_D A \rho}{(1+e \cos \nu)^3} \left[\frac{n}{\sqrt{1-e^2}} (1+2e \cos \nu + e^2)^{\frac{1}{2}} - \frac{p\omega_a \cos i}{(1+2e \cos \nu + e^2)} \right] \\ & \left[\frac{2n(1-\cos \nu)}{\sqrt{1-e^2}} - \frac{p\omega_a \cos i}{(1-e \cos \nu)} (e \sin^2 \nu - 2 \cos \nu + 2) \right] d\nu. \end{aligned} \quad (4.10d)$$

The integrals in Equations (4.10c and 4.10d) are evaluated by the Gauss-Legendre quadrature [41]. These are separated into two quadratures for orbits with eccentricity greater than 0.0001 and a perigee altitude between 90 – 300 km. The two quadratures has its range dependent on r_p and e and covers the interval $[-\pi, \pi]$. One quadrature is centred at perigee with the other covering the remaining part of the orbit. For perigee altitudes above 300 km, the integration is performed over the interval $[-\pi, \pi]$. For the circular option, the quadrature is not divided.

The rate of change \dot{e} is determined from Equation (4.7a), thus $\dot{e} = (\dot{e}_m)_{ob}$. $\dot{\Omega}$ and $\dot{\omega}$ are computed from Equations (4.7c) and (4.7d) respectively.

Estimation of the atmospheric density for the elliptical option is calculated from the satellite's altitude given as

$$H = r - R_e \left[1 - \frac{\sin^2 i}{f} \sin^2(\omega + \nu) \right], \quad (4.11)$$

where f is the Earth's flatness factor (constant), r is the satellite's orbital radius with short periodic terms included and is calculated from [1]

$$\begin{aligned} r = & \frac{p}{(1 + e \cos \nu)} - \frac{J_2}{2} \left(\frac{R_e}{p} \right)^2 \left(1 - \frac{3}{2} \sin^2 i \right) \left[1 + \frac{1 - (1 - e^2)^{\frac{1}{2}}}{e} \right] \cos \nu \\ & + \frac{2(1 - e^2)^{\frac{1}{2}}}{(1 + e \cos \nu)} + \frac{J_2}{4} \left(\frac{R_e^2}{p} \right)^2 \sin^2 i \cos(2\omega + 2\nu). \end{aligned} \quad (4.12)$$

The Jacchia 70 atmospheric model requires the satellite position unit vectors to determine its position relative to the diurnal bulge. The components of the unit vector are

$$\begin{aligned} \hat{x} &= \cos(\omega + \nu) \cos \Omega - \sin(\omega + \nu) \sin \Omega \cos i, \\ \hat{y} &= \cos(\omega + \nu) \sin \Omega + \sin(\omega + \nu) \cos \Omega \cos i, \\ \hat{z} &= \sin i \sin(\omega + \nu). \end{aligned} \quad (4.13)$$

4.7.1.2 Circular Option

For a perfect circular orbit, the variational equations of motion for the elliptical orbit do not hold because ω and M are undefined for circular orbits ($e = 0$). However, the sum $\omega + M$ does exist at $e = 0$. The time rate of change for eccentricity (\dot{e}_m) is zero for the circular case since e , under the influence of oblateness, is very small and atmospheric drag tends to keep e at zero.

The circular option consists of the rate of change of semi-major axis (\dot{a}) and longitude of ascending node ($\dot{\Omega}$) respectively, thus

$$\dot{a} = -\frac{1000\sqrt{a\mu}}{2M} \left(1 - \frac{\omega_a \cos i}{n} \right)^2 \int_{\pi}^{\pi} c_D A \rho \, d\nu, \quad (4.14a)$$

$$\dot{\Omega} = \left\{ -\frac{3}{2} J_2 + [J_4 (3.75 - 6.5625 \sin^2 i) + J_2^2 (5.625 - 7.125 \sin^2 i)] \left(\frac{R_e}{2} \right)^2 \right\} n \left(\frac{R_e}{a} \right)^2 \cos i, \quad (4.14b)$$

where a is the semi-major axis.

The atmospheric density estimation in the circular option is based on the altitude evaluated from

$$H = a - \frac{3}{2}J_2 \left(\frac{R_e}{a} \right) \left[1 - \frac{3}{2} \sin^2 i \right] + \frac{1}{4}J_2 \left(\frac{R_e}{a} \right) \cos 2\nu \sin^2 i - R_e \left[1 - \frac{\sin^2 i}{f} \sin^2 \nu \right], \quad (4.15)$$

and the satellite position vector determined from

$$\begin{aligned} \hat{x} &= \cos \nu \cos \Omega - \sin \nu \sin \Omega \cos i, \\ \hat{y} &= \cos \nu \sin \Omega + \sin \nu \cos \Omega \cos i, \\ \hat{z} &= \sin i \sin \nu. \end{aligned} \quad (4.16)$$

The true anomaly (also mean anomaly for circular orbit) is measured from the ascending node as used in the equation above.

4.8 Summary

The significance of SALT employed in this study is described. The approach used in SALT to estimate the decay or lifetime and to generate orbital ephemerides for LEO satellites which are perturbed by atmospheric drag and Earth oblateness due to spherical harmonics are presented. Liu's theory which was developed using the method of averaging employs sufficient numerical emphasis to include a rather sophisticated atmospheric density model.

Variational equations of motion applied in SALT were described [1]. Most importantly, the effects of Earth oblateness and atmospheric drag which are the principal forces influencing the decay of Earth satellites were discussed. Mean solar flux and magnetic index values required for calculating the atmospheric density was presented. Implementation of SALT in LIFTIM based on both the elliptical and circular options were presented and discussed. The methodology and the simulation environment applied in this study is given in chapter 5.

Chapter 5

Simulation Environment

5.1 Introduction

This chapter describes the methods implemented in this study. The LIFTIM software package, as explained in Chapter 4, is utilised. The Satellite ToolKit (STK) software was employed in this study as well. Further analysis on predicting the lifetime of satellites using solar sails is addressed here. The results of the decay and solar sail predictions will be presented in Chapter 6.

5.2 LIFTIM Application

LIFTIM [1] was implemented in FORTRAN with MATLAB scripts (Appendix C) written and executed to achieve the results as presented in this study. LIFTIM was evaluated against the actual orbit decay histories of *Iridium-85* and *Starshine-1* satellites prior to applying the solution to the SUNSAT orbit. LIFTIM was also applied to determine the expected lifetime of a 1U CubeSAT (ZACUBE-01).

5.3 Data Preparation

The LIFTIM program uses two input files for the lifetime analysis: the *solar.dat* [8] file contains observed and long-term predicted solar flux and magnetic activity data, and the other file contains satellite specific parameters such as initial orbital elements, mass, drag coefficient and model-specific parameters. Input files for the various satellites used in this

study are listed in Appendix B including an explanation of the parameters.

The cross-sectional area, mass (satellite geometry), drag coefficient (C_D) and the satellite state vectors are some of the parameters required by the model. General information for the satellites was obtained from [11] and is given in Table 5.1. The satellite state information and the osculating orbital elements were extracted from the first available TLE files after launch. Two line element's were obtained from [11] and processed to obtain their desired states presented in Tables 5.2 and 5.3.

Table 5.1: Geometry of decayed satellites used in evaluating SALT.

Satellite	International designator	Mass (kg)	Area (m^2)	Launch Date	Deorbit Date
Iridium 85	25529	689	5.12	6 November, 1998	30 December, 2000
Starshine-1	25769	39	0.18	27 May, 1999	18 February, 2000
SUNSAT	25636	63	0.40	23 February, 1999	—

Table 5.2: Two-Line Elements at time closest after launch.

Iridium 85	
1	25529U 98066C 98310.67459616 .00000038 00000-0 00000+0 0 11
2	25529 086.0152 311.9254 0013613 223.7877 136.0772 15.14192003 04
Starshine-1	
1	25769U 99030B 99156.34105187 .02711664 00000-0 29127-1 0 12
2	25769 51.5915 257.3806 0012795 323.4372 36.5573 15.59813944 1386
SUNSAT	
1	25635U 99008B 99068.23100837 .00000196 00000-0 61890-4 0 482
2	25635 96.4768 19.8698 0151917 209.5613 149.6933 14.40791150 1989

Table 5.3: TLE-derived state vectors and osculating orbital elements of dates closest to launch.

State vectors and Kepler Elements	Iridium-85 6 Nov., 1998 16:11:25.11 UTC	Starshine-1 5 June, 1999 08:11:06.88 UTC	SUNSAT 9 Mar., 1999 05:32:38.12 UTC
$X(km)$	4615.72658	-1470.88476	6798.25947
Y	-5140.06454	-6597.40002	2455.08495
Z	-3.25021	7.57515	14.89957
$V_x(km.s^{-1})$	0.39972	4.65907	0.32093
V_y	0.34453	-1.0378	-0.76881
V_z	7.57386	6.02051	7.32982
$a(km)$	6901.57000	6766.33242	7134.02304
e	0.00136	0.00128	0.01519
$i(^{\circ})$	86.0152	51.5915	96.4768
$\Omega(^{\circ})$	311.9254	257.3806	19.8698
$\omega(^{\circ})$	223.7877	323.4372	209.5613
$M(^{\circ})$	136.0772	36.5573	149.6933
$r_a(km)$	532.82	396.856	864.255
r_p	514.04	379.541	647.523

5.3.1 Drag Coefficients

Optimum C_D -values for the satellites were obtained in a drag analysis study [12] as those rendering the minimum state errors when comparing long-term precision propagated states (several days) with the NASA-generated Satellite Laser Range (SLR)- observed states for SUNSAT and the TLE-derived states (other satellites). The drag coefficients and their respective position and velocity errors for each satellite were estimated by precision orbit analysis using the precision propagator *orbfitz* [12], and are presented in Table 5.4.

For *Iridium-85* and *Starshine-1*, two TLE's five days apart, were used to derive an analysis epoch state, $(\mathbf{r}_o, \mathbf{v}_o)$ at an epoch t_o and a final reference state, $(\mathbf{r}_f, \mathbf{v}_f)$, at time $t_f = t_o + 5days$. Using the geometry of the satellites and an initial C_D - estimate, each satellite's initial state, $(\mathbf{r}_o, \mathbf{v}_o)$, was propagated from t_o to t_f . Their respective propagated states at t_f , $(\mathbf{r}_{fp}, \mathbf{v}_{fp})$, were compared to the reference state, $(\mathbf{r}_f, \mathbf{v}_f)$ and the error $\|((\mathbf{r}_f, \mathbf{v}_f) - (\mathbf{r}_{fp}, \mathbf{v}_{fp}))\|$ was calculated. The C_D -value was adapted and the process repeated until a sufficiently small

Table 5.4: Drag coefficients, position and velocity errors for SUNSAT, Iridium-85 and Starshine-1.

SUNSAT		
C_D	Position error (km)	Velocity error (km/s)
2.0	3.614	0.0038
2.2	2.965	0.003
3.0	0.369	3.834e-4
3.08	0.116	1.52e-4
3.1	0.063	1.254e-4
3.15	0.129	1.96e-4
3.26	0.4804	5.43e-4
3.27	0.513	5.77e-4

Iridium-85		
C_D	Position error (km)	Velocity error (km/s)
3.0	150	0.165
2.8	164	0.181
3.8	91	0.101
4.0	76.9	0.085
4.4	47.9	0.050
4.85	15.31	0.016
4.95	8.06	0.008
5.0	4.4	0.004
5.15	6.45	0.007
5.3	17.34	0.020

Starshine-1		
C_D	Position error (km)	Velocity error (km/s)
1.9894	170.0	0.20
2.0822	65.9	0.08
2.0955	51.0	0.06
2.1220	21.1	0.02
2.1300	12.0	0.01
2.1353	6.1	0.01
2.1366	4.7	0.0055
2.1370	4.22	0.0050
2.1375	3.64	0.0043
2.1485	8.8	0.012
2.1883	53.8	0.06
2.3209	204.0	0.2

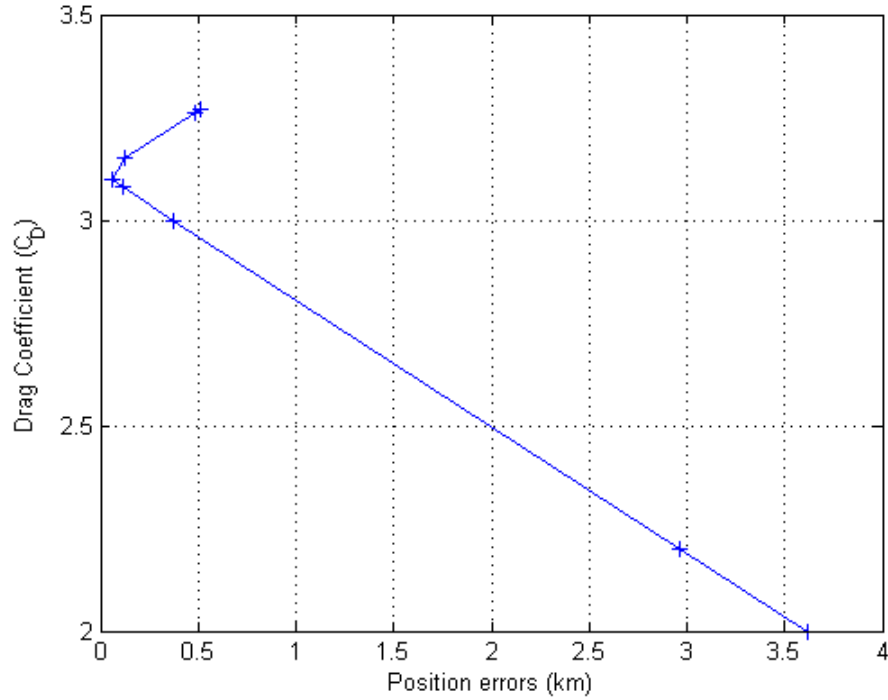


Figure 5.1: SUNSAT position errors using various drag coefficients adapted from [12].

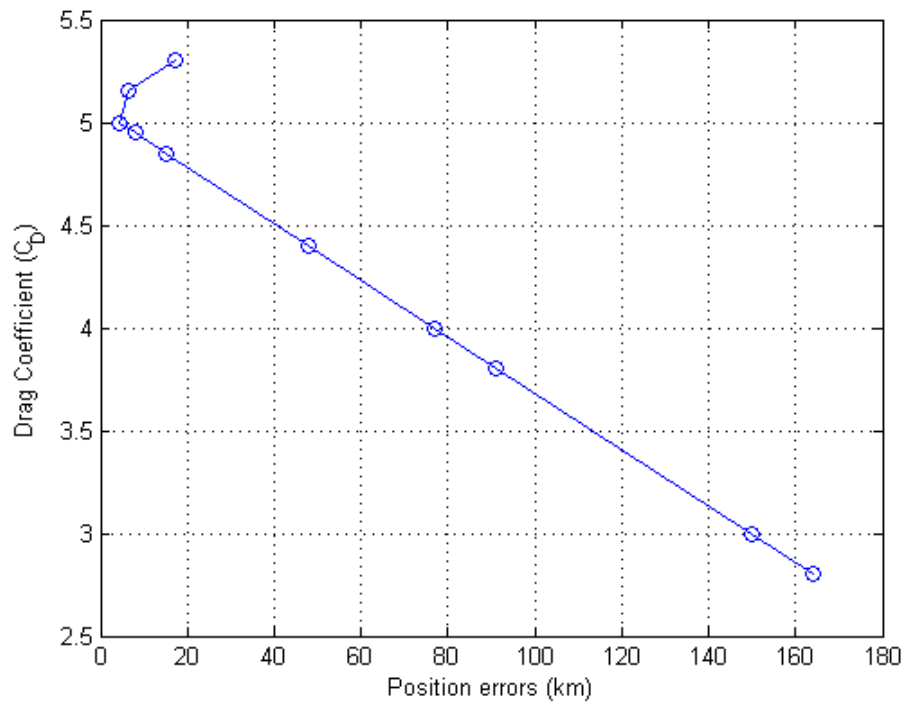


Figure 5.2: Iridium-85 position errors using various drag coefficients adapted from [12].

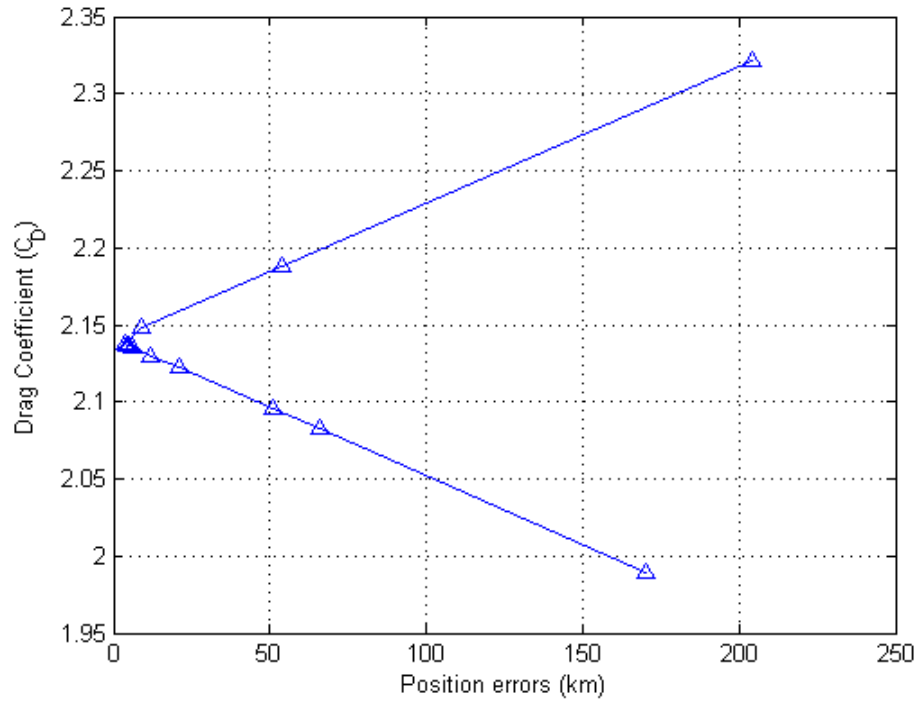


Figure 5.3: Starshine-1 position errors using various drag coefficients adapted from [12].

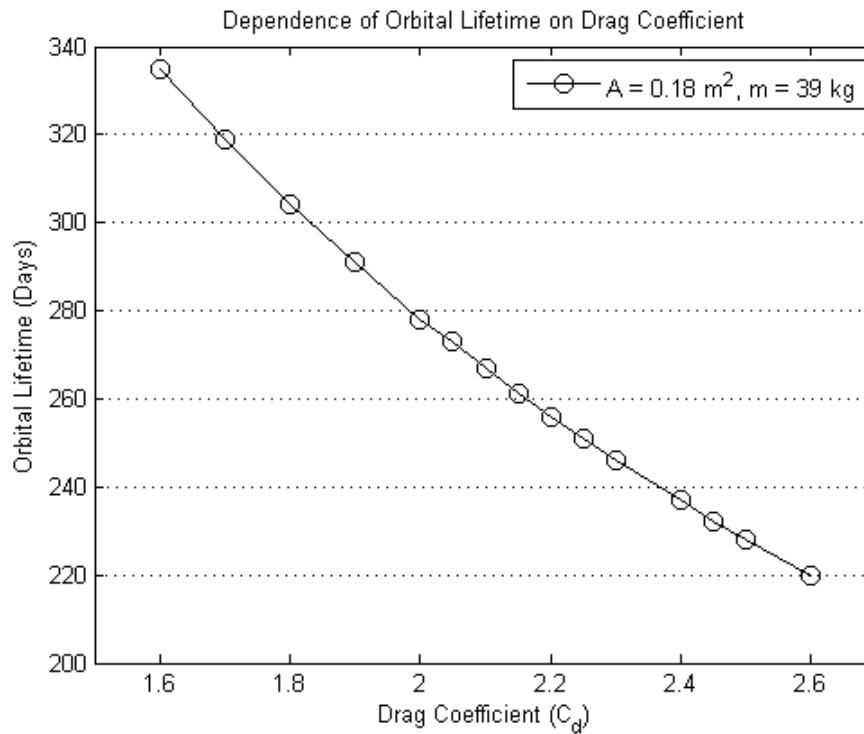


Figure 5.4: Dependence of orbital lifetime on drag coefficient for Starshine-1 satellite.

error was obtained (< 5 km for *Starshine-1* and *Iridium-85* and 63 m for SUNSAT) [12]. The position errors resulting from all the drag coefficients evaluated are shown in Figures 5.1 to 5.3. The effect of drag coefficient on orbit lifetime is important. Orbital lifetime decreases with increasing drag coefficients as illustrated in Figure 5.4 with drag area (A) of 0.18 m^2 and mass (m) 39 kg.

Optimum satellite drag coefficients, with their corresponding errors in position and velocity as used in this study, are listed in Table 5.5.

Table 5.5: Optimum drag coefficients .

Satellite	c_D	$BC = \left(\frac{m}{c_D * A}\right)$ ($kg.m^{-2}$)	r -error (km)	v -error ($km.s^{-1}$)
Iridium-85	5.0	26.9	4.4	0.004
Starshine-1	2.1375	101.3	3.6	0.0043
SUNSAT	3.1	50.8	0.063	1.254e-4

5.3.2 Decay Predictions

The relevant historic TLE-derived orbital elements (semi-major axis, eccentricity, apogee radius, perigee radius and inclination) for the different satellites were extracted from their launch dates to decay dates, and compared with the corresponding predicted values from LIFTIM and Satellite ToolKit (STK) software packages. Due to the long orbital lifetime (years), the evolution of the orbital elements, rather than the cartesian position of the satellites over their lifetimes, was analysed. The TLE-derived orbital elements were overlaid as a time series on the predicted values. The error between the observed and predicted values were calculated and plotted as a function of time for a quantitative comparison.

The evolution of the orbital elements from launch until present (1st November, 2012) was generated and compared with historic TLE's of SUNSAT and predicted values of STK. Similarly, the errors between the observed and predicted values were calculated. A spectrum distribution of the eccentricity of SUNSAT was obtained using the Fast Fourier Transform (FFT). Two steps are required to satisfy the conditions of the FFT algorithm.

- Interpolation is used to reproduce the eccentricity set e_i , thus the data set from unevenly spaced is converted to an evenly spaced data set, as the FFT algorithm requires evenly spaced data.
- e_i is replaced by e'_i (evenly spaced eccentricity data set).

The expected lifetime of a 1U CubeSAT (ZACUBE-01), which was recently developed and built by postgraduate students from the French South African Institute of Technology (FSATI) group at the Cape Peninsula University of Technology (CPUT) [50], was determined using the LIFTIM and STK software packages. The predicted evolved orbital elements were analysed, compared and relevant graphs produced. The characteristic orbital parameters are listed in Table 5.6. A typical C_D value of 2.2 (for non-spherical convex-shaped spacecraft) was implemented with a drag area of $0.01 m^2$ and mass of 1 kg.

Table 5.6: Orbital parameters for ZACUBE-01.

Altitude (km)	Semi-major axis (km)	Eccentricity	Period (mins)	Mean motion	Inclination (deg)
600	6978	0	96.54	14.8453	97.03

5.3.2.1 STK Lifetime Tool

STK is an off-the-shelf mission modelling and analysis software for space systems. It is developed to perform analysis of complex missions and includes integrated 2-D and 3-D graphics for visualisation. The software is also capable of custom data product generation, including reports, graphs and Visual Data Format (VDF) files.

The lifetime analysis tool of STK estimates a satellites's orbital lifetime i.e., the amount of time a satellite remains in orbit before atmospheric drag and other perturbative forces causes its re-entry. The analysis tool is based on algorithms developed at NASA's Langley Research Centre [44]. The lifetime tool requires the inputs from the user regarding the satellite's characteristics (launch date, initial orbit, mass, cross-sectional area, drag coefficient etc.), similar to LIFTIM. The algorithm computes drag effects by applying the satellite characteristics along with an atmospheric density model (Jacchia 1970) and a solar flux file, which are selected by the user from a list of options.

The Jacchia 1970 atmospheric density model which was employed by the LIFTIM software package was also chosen and used in STK.

Figure 5.5 shows the Graphical User Interface (GUI) for the lifetime analysis tool for SUNSAT with its characteristic drag coefficient, drag area and mass. Similar analyses were executed for the other satellites with their corresponding parameters and the decay dates determined. The simulations were performed using the most recent solar flux file [45]. These files contain predictions of solar radiation flux and geomagnetic index values which are produced by K. H. Schatten in ASCII format and, updated frequently [46].

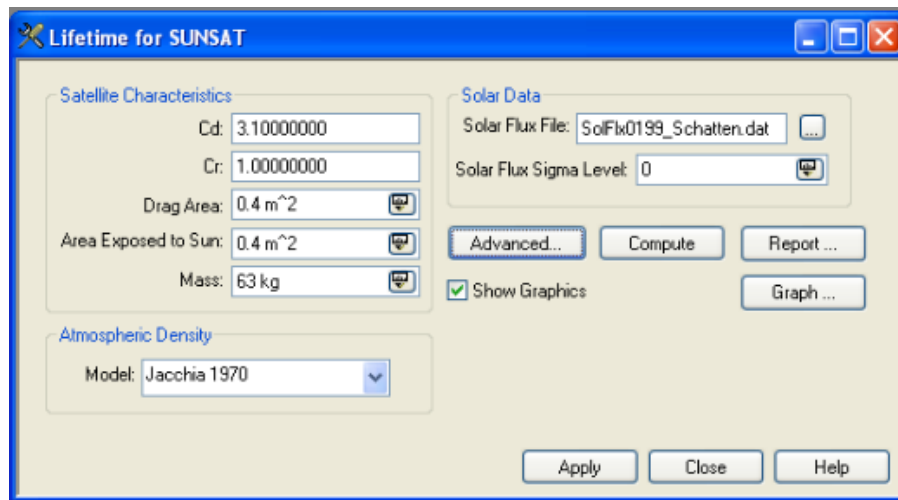


Figure 5.5: STK Lifetime Tool (GUI for SUNSAT).

The solar flux sigma level is maintained at zero, in order to use the mean solar flux and weighted planetary geomagnetic index. After the simulations, the lifetime tool estimates the orbital lifetime of the satellite and provides its corresponding date of decay. It should be emphasised that, although the lifetime computations are based on sophisticated orbital theory and accurate environment models, the results are estimates due to the seemingly random variations in atmospheric density and the difficulty in accurately predicting solar activity involved in calculating a satellite's orbital lifetime [47].

The drag integration routine in STK is performed by n 9-point Gaussian quadratures per orbit, where n is the number set which determines increase in accuracy and if lowered below 6, increases the speed. This routine approximately integrates the slowly varying orbital elements over time. It does this by integrating over one orbit to determine the rate-of-change of each variable, and then assumes this rate is constant for n number of orbits per calculation

The Schatten solar flux data (nominal) was also implemented in the LIFTIM program to predict the lifetimes of the test case satellites and the expected deorbit dates of SUNSAT and ZACUBE-01. Comparison of the solar flux data for both LIFTIM and Schatten is shown in Figure 5.6.

The LIFTIM solar flux data contains observed and predicted solar flux and geomagnetic index information, derived from recent monthly mean solar activity values obtained from the National Oceanic and Atmospheric Administration (NOAA) [48]. The data file contains 5, 50 and 95 percentile solar activity data, which are obtained using the MSFC Solar Activity Future Estimation (MSAFE) model [49]. The model estimates the intermediate-term (months) and long-term (years) behaviour of $F_{10.7}$ and A_p for up to 132 months

into the future initialised from a cycle minimum or a cycle maximum.

The Schatten solar flux data in STK, on the other hand, also contains predicted values of the monthly mean 10.7 cm solar radiation flux ($F_{10.7}$) and the geomagnetic index formatted for compatibility with STK software. The difference in the solar flux data as shown in Figure 5.6 is as a result of the different methods used in the estimation process for each data set.

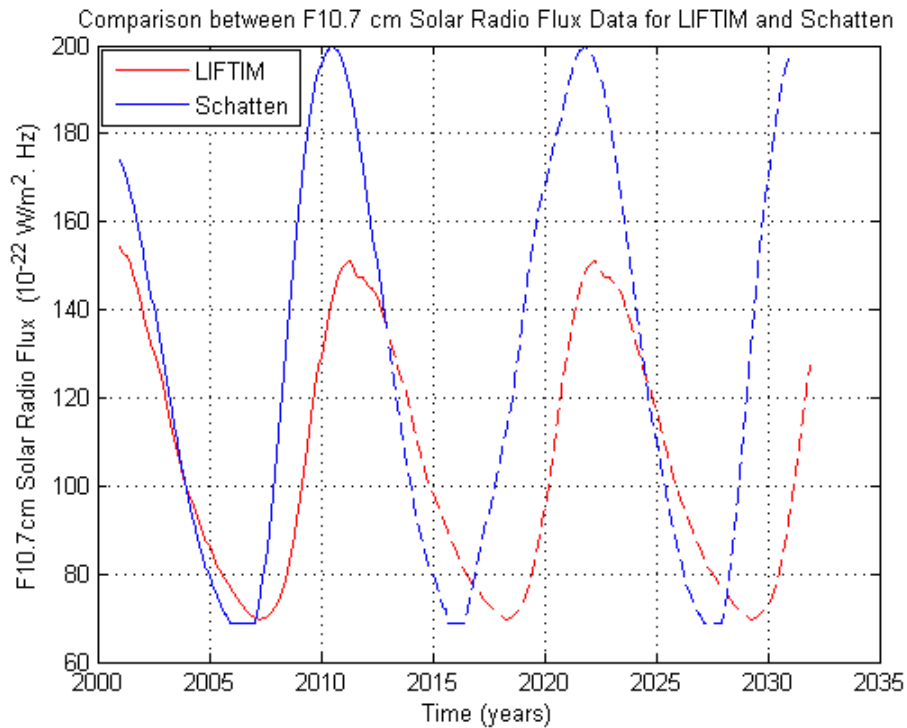


Figure 5.6: Comparison between Solar Flux Data for LIFTIM and Schatten.

The Schatten solar flux data has high $F_{10.7}$ cm values as compared to the solar flux data of LIFTIM. The peaks lie around almost the same time (year) and coincide very nearly to solar maxima, to levels of high solar activity.

5.4 Effects of using a DeOrbitSail

Deorbiting using drag sails was investigated. A comparison of sail sizes as a function of altitude, for initial masses between 200 kg and 1000 kg to deorbit within 25 years was analysed and presented in chapter 6.

The lifetime of SUNSAT was predicted assuming a 10 m^2 sail deployed. Similarly, the 1U CubeSat (ZACUBE-01) lifetime was also estimated assuming 10 m^2 drag sail. Comparisons were made and the advantage of a low-cost solar sail was established.

The drag sail concept was also applied to *Iridium-85* and *Starshine-1* satellites to investigate decreased lifetimes should a sail have been used. Relevant graphs are presented in Chapter 6.

5.5 Summary

This chapter presented the approach used in this study. Application of the lifetime software packages (LIFTIM and STK) were discussed. Drag coefficients were presented with their respective position and velocity errors as estimated by precision orbit analysis using the precision propagator *orblitz*. Evaluation and methods used in the decay prediction of the test case satellites, SUNSAT and 1U CubeSAT (ZACUBE-01) were described. The method used in deorbiting satellites employing solar sails was addressed briefly and will be presented and discussed in Chapter 6.

Chapter 6

Results and Discussion

6.1 Introduction

This chapter presents a comparison of historic (observed) TLE-derived orbital elements and those predicted by the decay and lifetime packages LIFTIM and STK for all the satellites considered in this study. The test results are presented for two considered scenarios: observed decay histories and, the predicted decay results when employing a drag sail to demonstrate the deorbisail concept as space debris mitigation mechanism.

6.2 Schatten data adopted in LIFTIM

A comparative investigation was performed using the Schatten solar flux data (nominal) [45] in the LIFTIM program ($LIFTIM_{Schatten}$) to determine variations in the evolved orbital parameters (semi-major axis, eccentricity, inclination, apogee height) for the test case satellites, SUNSAT and ZACUBE-01. The characteristic orbital parameters, mass and C_D values for the different satellites were maintained. Predicted orbit decay dates for the respective satellites were estimated.

6.3 Comparative Decay Results without a DeOrbitSail Mechanism

6.3.1 Iridium-85 Satellite

The *Iridium-85* satellite was launched on the 6th of November, 1998. Its observed decay date was 30 December, 2000. After careful analysis, the LIFTIM lifetime tool predicted an orbit decay date of 24 December, 2000 while that of STK computed an orbit decay date of 26 December, 2000. The predicted decay dates differ in six days, four days and eight months respectively for LIFTIM, STK and LIFTIM_{Schatten} from the observed decay date. Figures 6.1 to 6.3a shows variations in the predictions for the different orbital parameters (semi-major axis, eccentricity, inclination, apogee height) of the Iridium-85 satellite. Orbit decay predictions using LIFTIM, STK and LIFTIM_{Schatten} are shown in Figures 6.3b to 6.4 respectively.

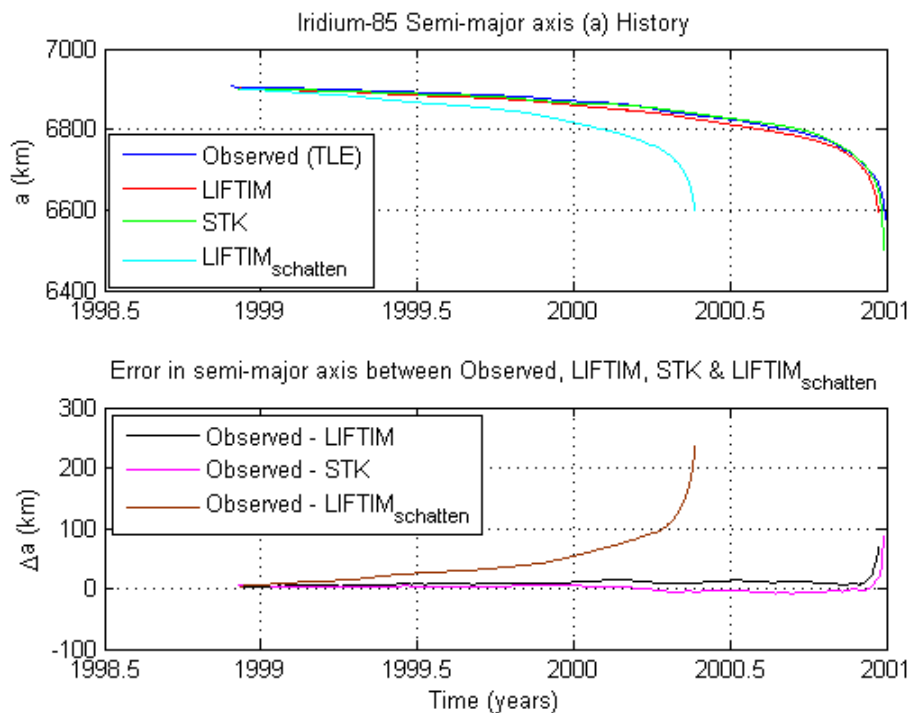
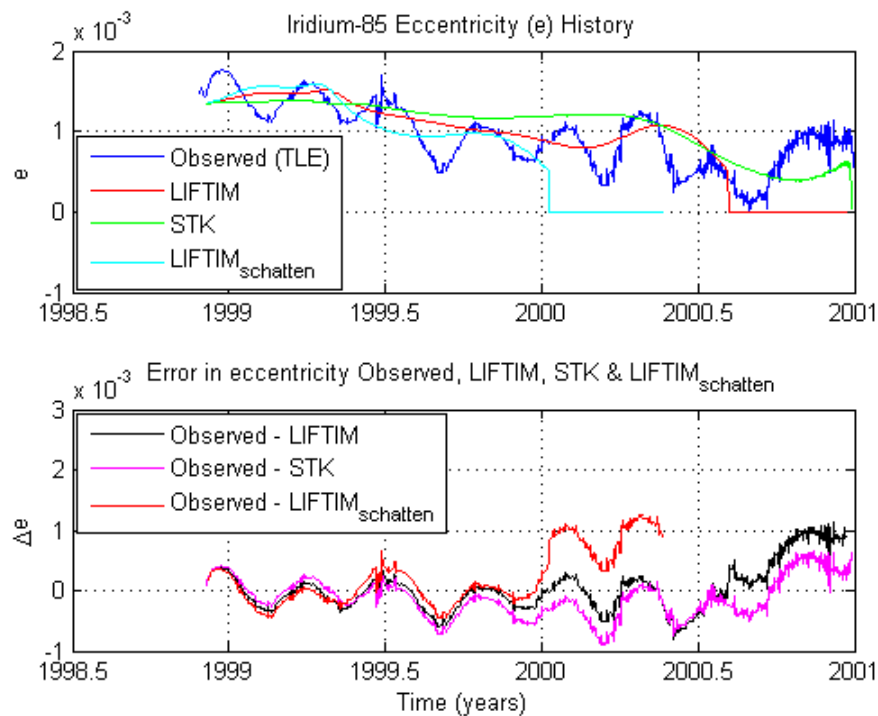
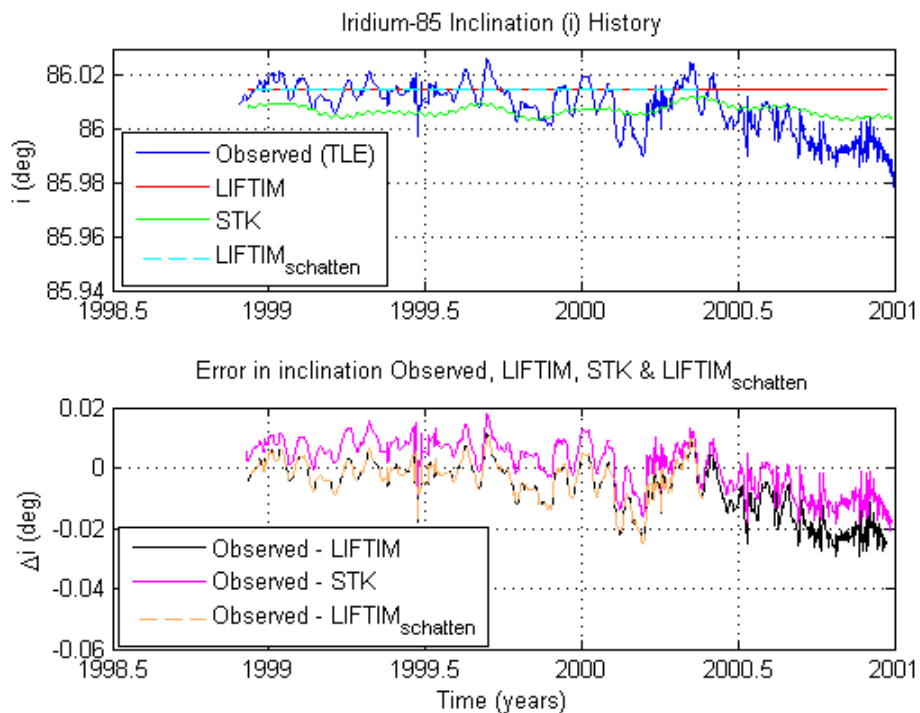


Figure 6.1: Comparison in semi-major axis of Iridium-85.



(a)



(b)

Figure 6.2: Comparison in (a) eccentricity (b) inclination for Iridium-85.

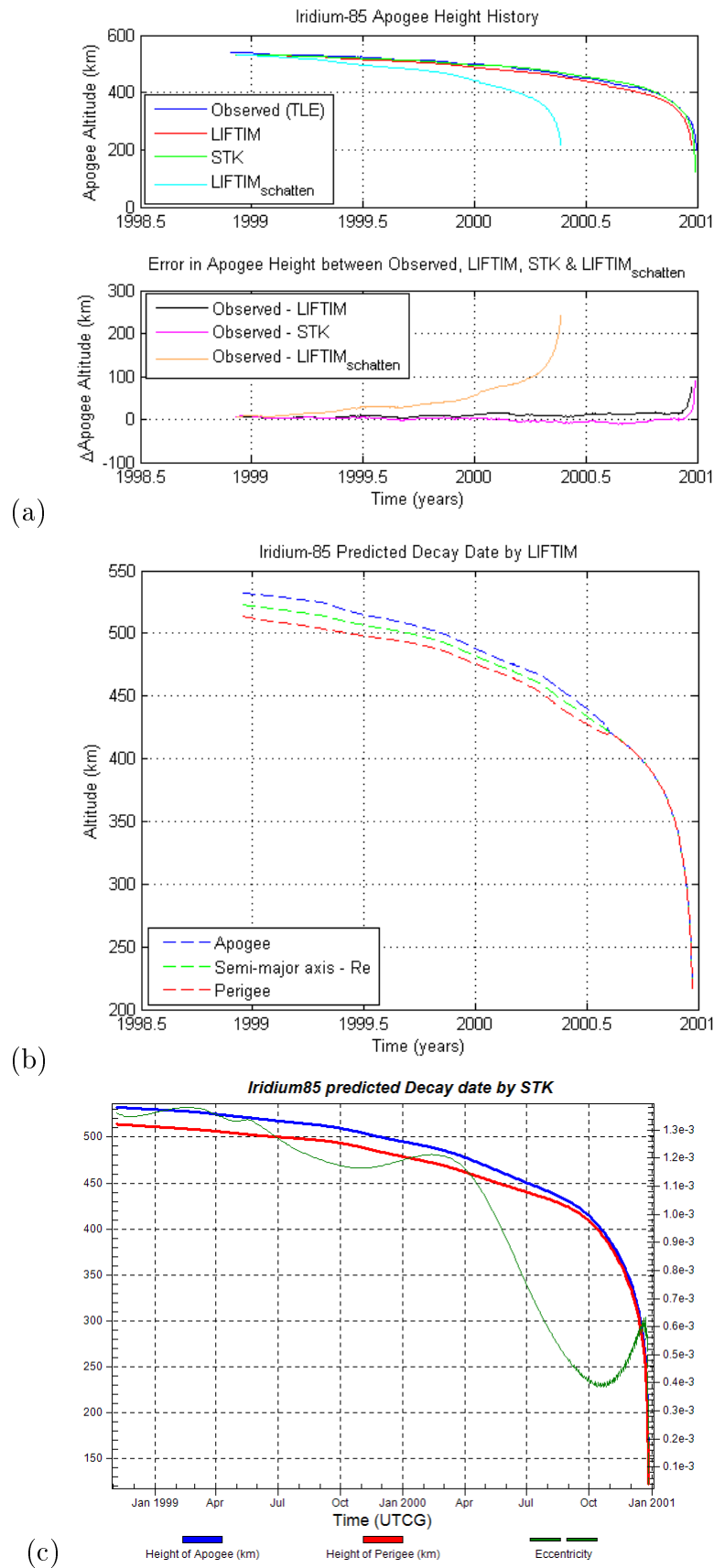


Figure 6.3: (a) Comparison in apogee height. (b) Predicted decay date of Iridium-85 using LIFTIM and (c) STK.

Time histories of the predicted and observed orbital parameters from epoch date (6th November, 1998) to deorbit date is presented with the respective qualitative and quantitative error comparisons. Periodic changes as a result of the Earth's oblateness are observed in eccentricity and inclination (though not very evident as in Figures 6.1b and 6.2a) with secular variations in the semi-major axis as shown in Figure 6.1. The small error difference between observed TLE, LIFTIM and STK shows prediction accuracy of the software packages except for LIFTIM_{Schatten} which showed large variation.

When the orbital eccentricity drops below the switchover eccentricity value (0.0005), the elliptical orbit option automatically switches to the circular orbit option for most LIFTIM predictions as discussed in subsection 4.7.1 until re-entry (Figures 6.1b, 6.5b).

Atmospheric drag effects have negligible effects on the rest of the orbital parameters according to the Liu theory [1]. Since secular decrease in semi-major axis and eccentricity are the principal effects of atmospheric drag, the inclination angle is assumed to be zero (equations 4.3a and b) and hence remains constant throughout the orbital lifetime as shown for the prediction using LIFTIM and LIFTIM_{Schatten} (Figure 6.2a). Changes in the apogee height, gives an indication of how the solar activity levels vary with time (years) depending on the software packages as in Figure 6.2b.

The predicted and observed TLE decay dates are shown below.

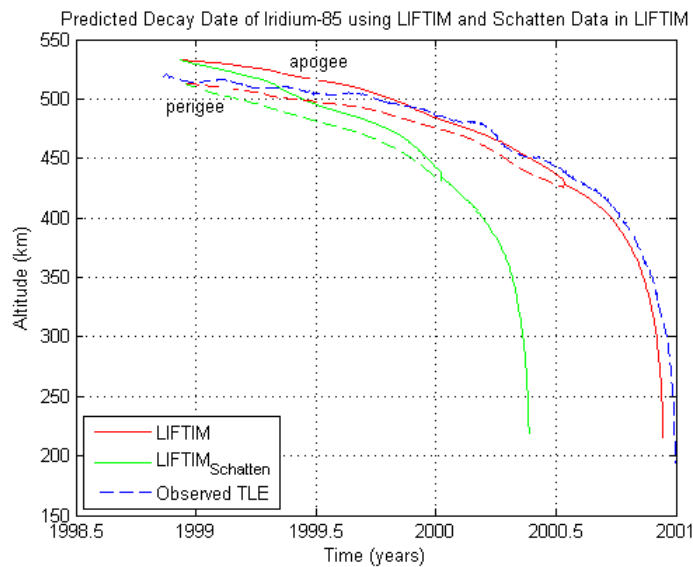


Figure 6.4: Predicted orbit decay of Iridium-85 with and without Schatten solar flux data.

The estimated decay date for LIFTIM_{Schatten} is 20 April, 2000. The difference in decay prediction is due to the vast difference in the solar activity data recorded for the various software packages which uses different algorithms in estimating the solar flux data.

6.3.2 Starshine-1 Satellite

Changes in the predicted orbit elements (semi-major axis, eccentricity, inclination, apogee height) of the starshine-1 satellite from epoch date, 5 June 1999 until decay date 18 Feb. 2000, are presented in Figures 6.5 to 6.6 with estimated error predictions. The predicted decay dates are 08 March, 2000 and 28 Feb. 2000 differing by eighteen and ten days respectively for LIFTIM and STK from the observed decay date.

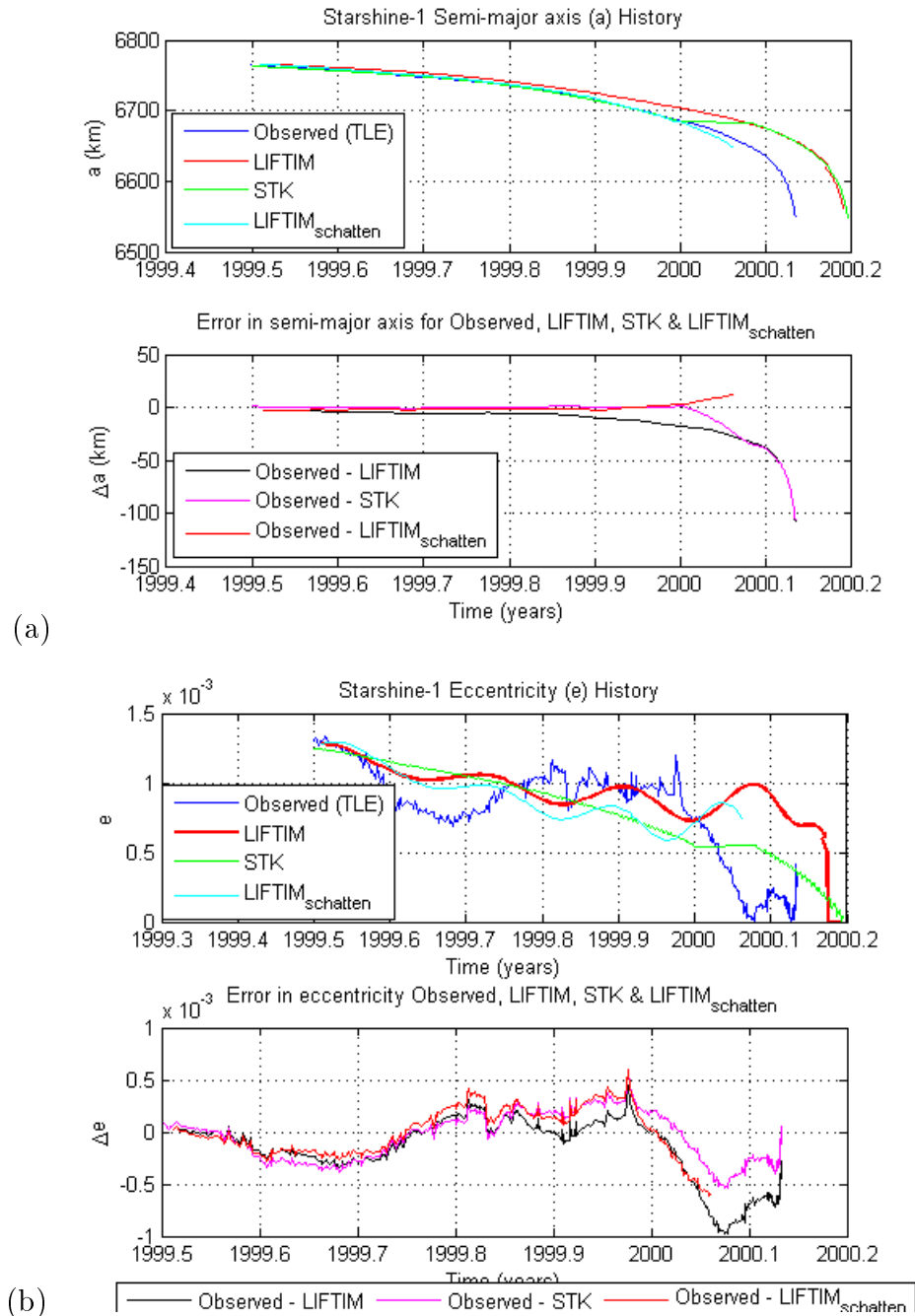
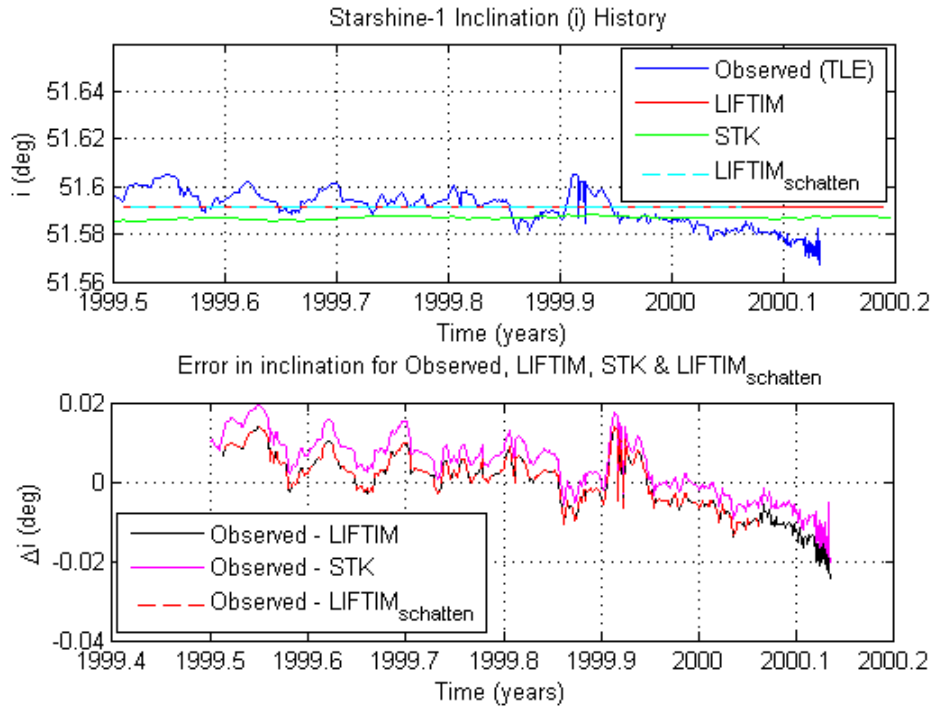
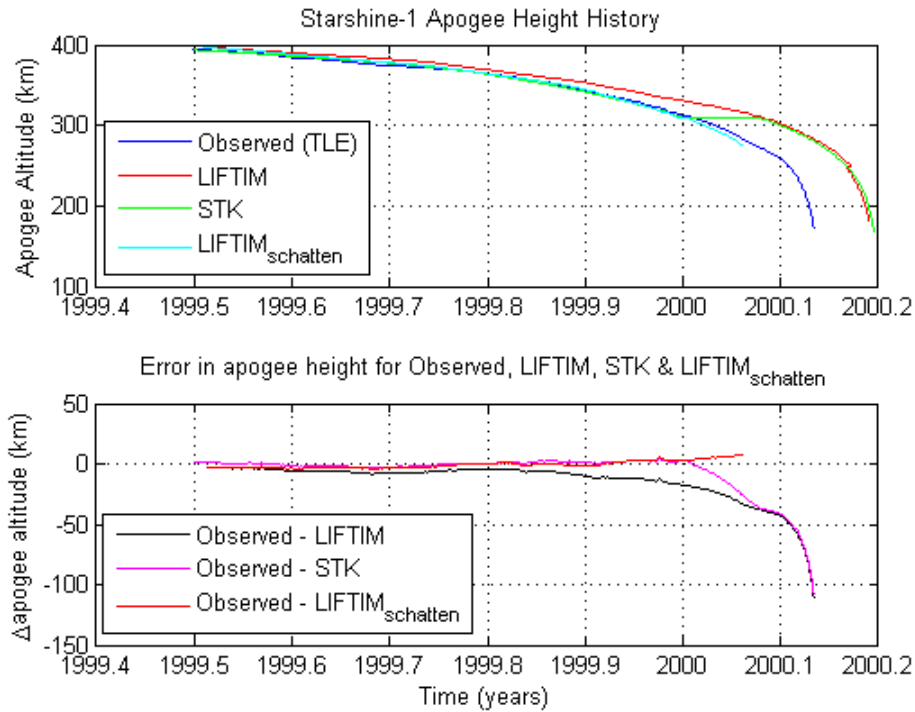


Figure 6.5: Comparison in (a) semi-major axis. (b) eccentricity of Starshine-1.

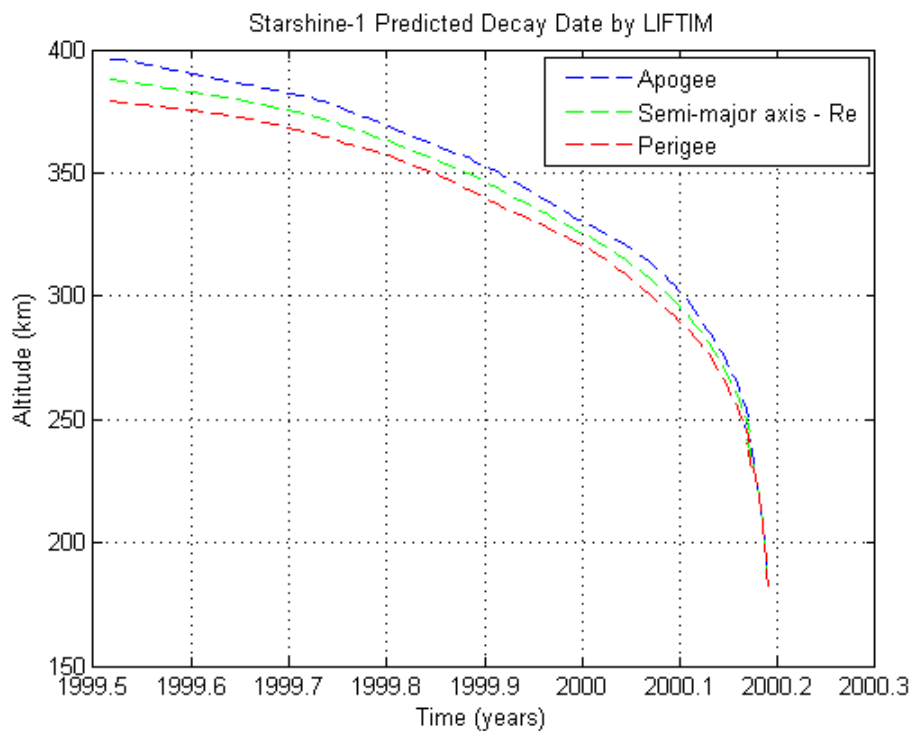


(a)

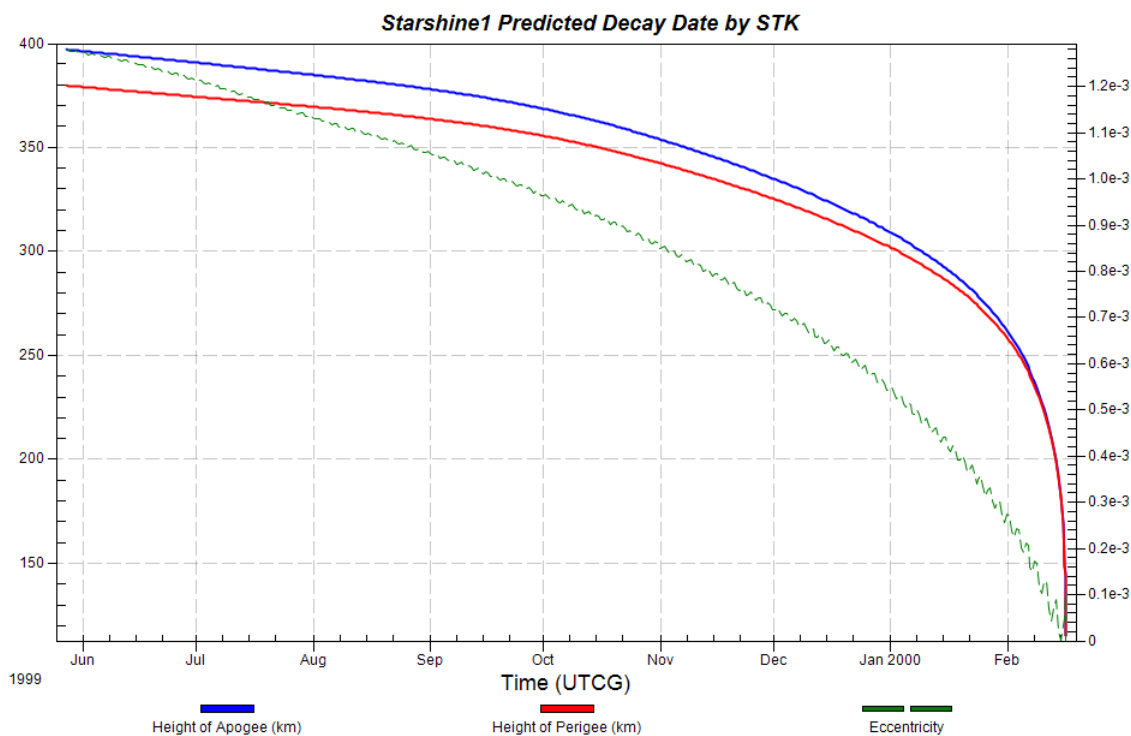


(b)

Figure 6.6: Comparison in (a) inclination. (b) apogee height of Starshine-1.



(a)



(b)

Figure 6.7: Predicted decay date of Starshine-1 using (a) LIFTIM. (b) STK

Similarly, the change in inclination angle is assumed to be zero and hence the inclination angle remains constant throughout the orbital lifetime (Figure 6.6a). Average orbital

height for *starshine-1* is about 400 km. Figure 6.7a,b shows the decay rate of *starshine-1* orbit. The gradual decrease is caused by atmospheric drag. The rate of descent is not constant and this variation is caused by changes in the density of the tenuous outer atmosphere due mainly to solar activity. The sudden deviation from year 2000 in the STK curve for *starshine-1* (Figures 6.5a, 6.6b) is probably as a result of increase in solar activity levels which altered the decay path until a rapid descend resulting in re-entry. Figure E.2 (Appendix E) shows observed cycle solar maximum and minimum variations.

The evolved orbital elements as depicted above show periodic and secular variations in both the semi-major axis and eccentricity. The orbit decay date for *starshine-1* using Schatten solar flux data in LIFTIM program is estimated as 22 December, 1999 and differs in about two months from the observed TLE decay date.

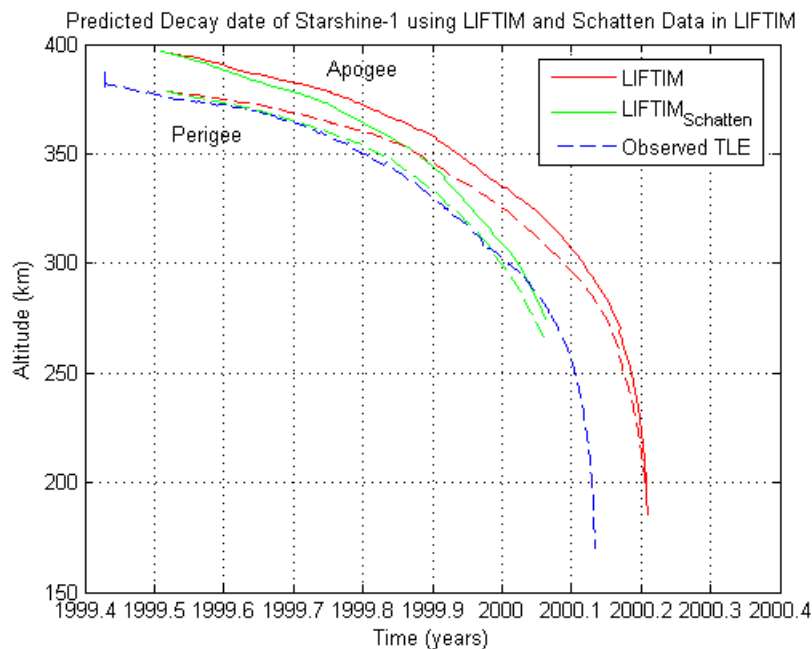


Figure 6.8: Predicted orbit decay of Starshine-1 with and without Schatten solar flux data.

6.3.3 SUNSAT

The time histories of the SUNSAT's predicted and observed orbital parameters from epoch date, 9 March 1999 until 1 November, 2012 are shown in Figures 6.9b to 6.11a. Figure 6.9a shows rapid then gradual decrease of about 10 km in the altitude of SUNSAT since its launch. The evolution of semi-major axis, eccentricity, inclination and apogee height are presented and the respective error predictions between the observed (TLE) and predicted values are shown. Secular variations are observed in the semi-major axis and to a small

extent in the eccentricity.

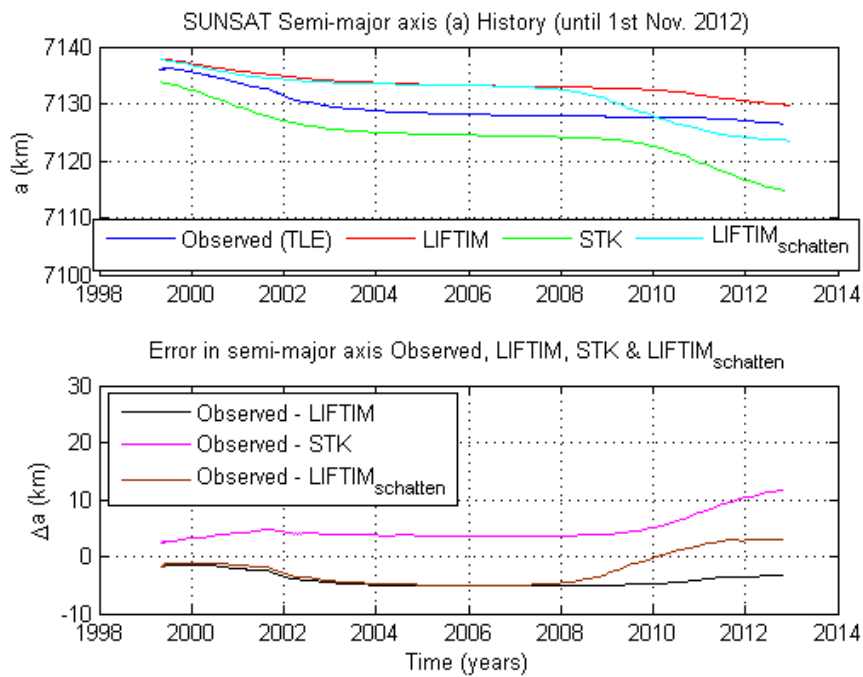
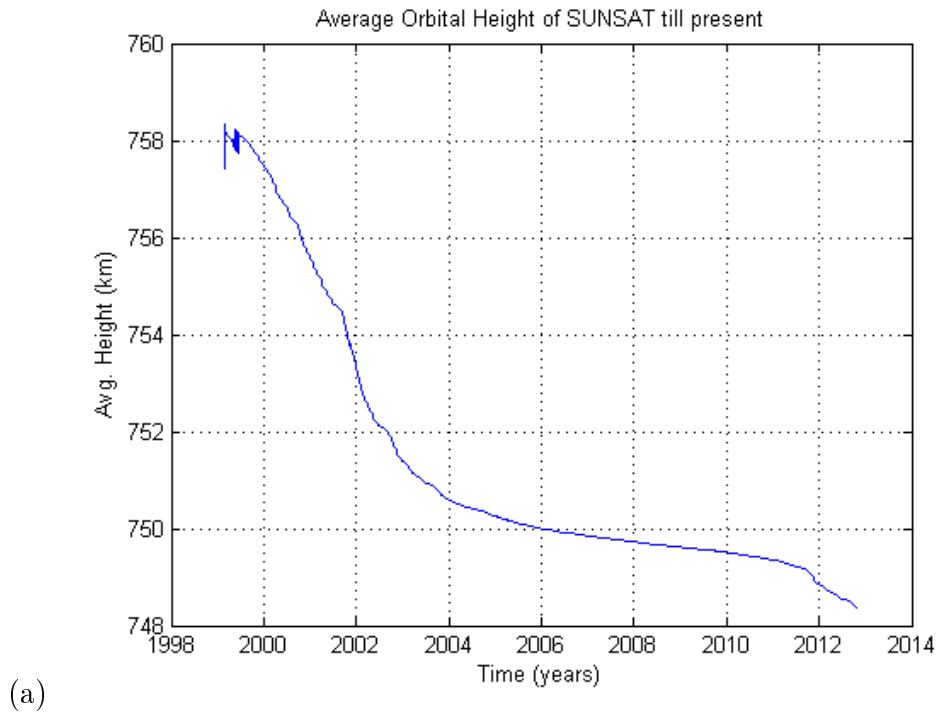


Figure 6.9: (a) Average orbital height of SUNSAT since launch. (b) Evolution of semi-major axis from epoch until 1st Nov. 2012.

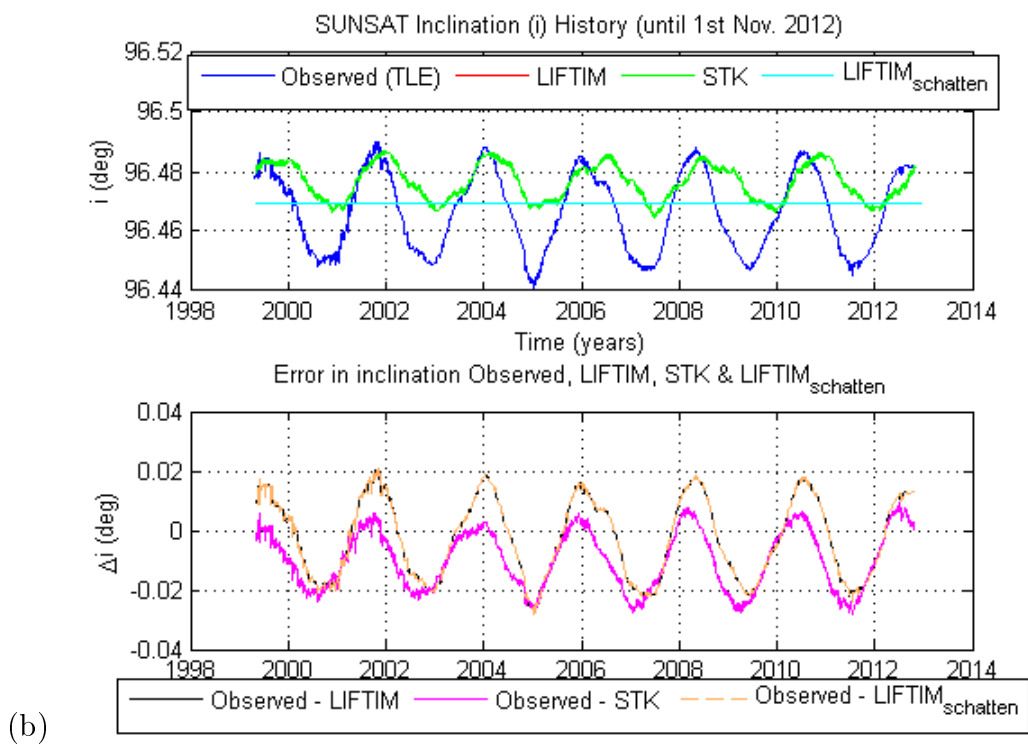
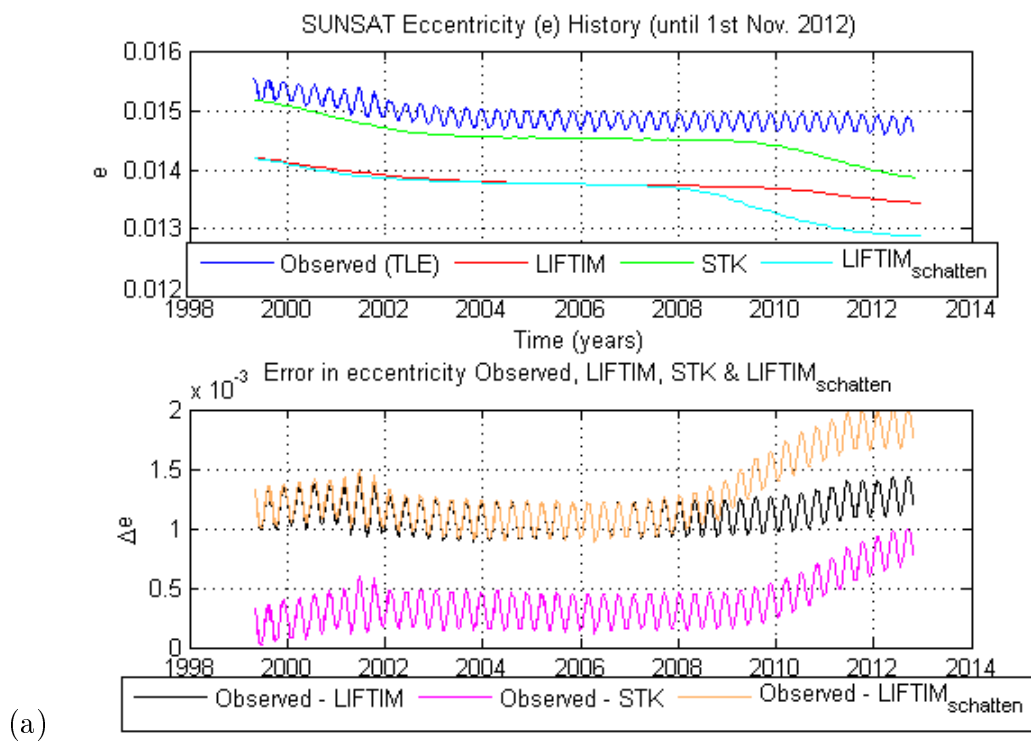
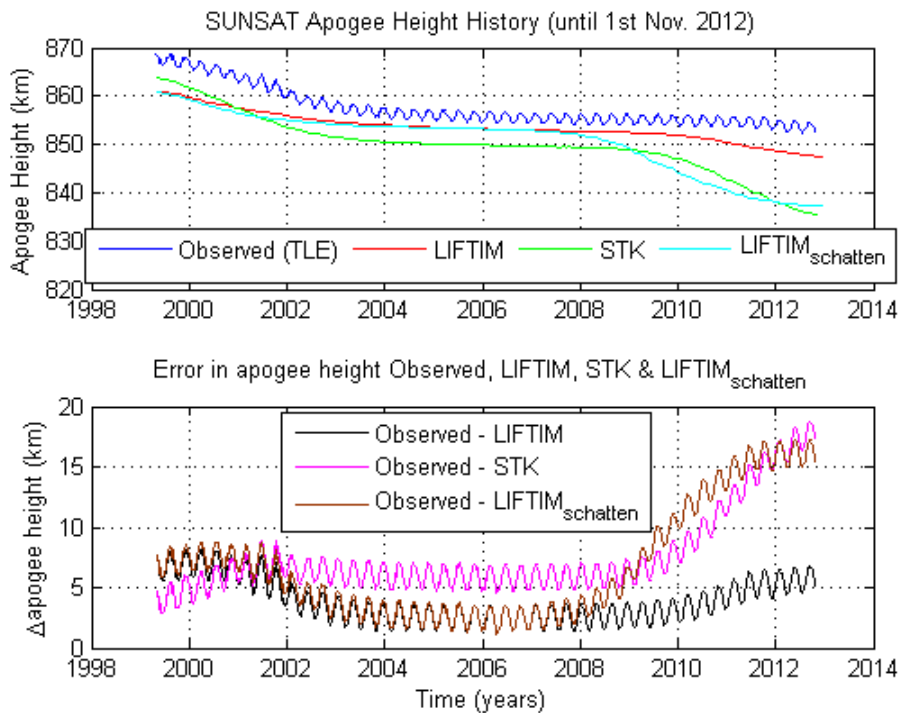
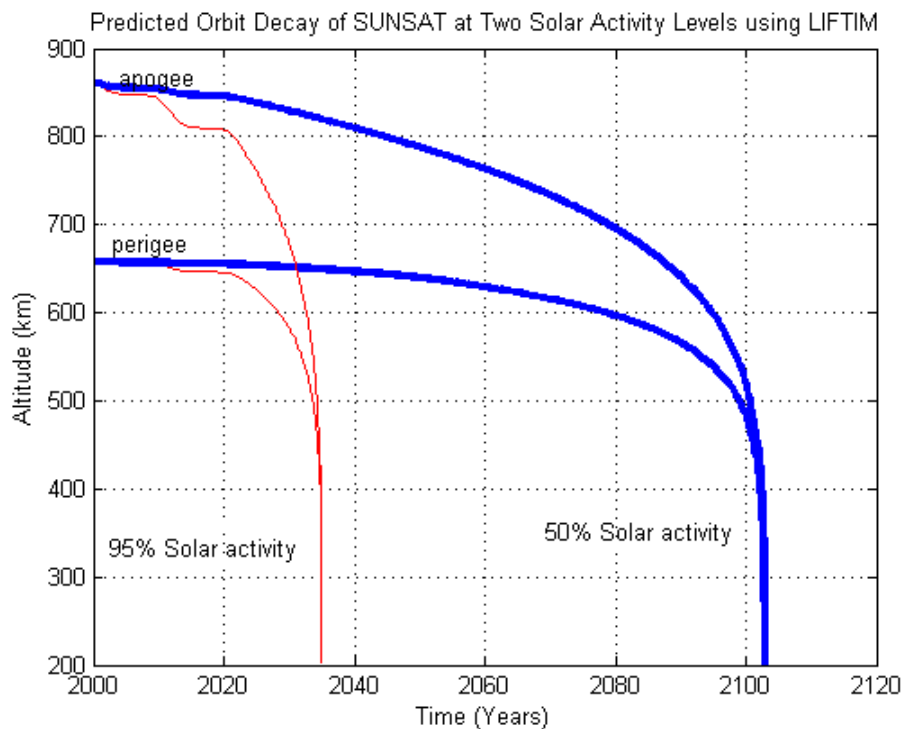


Figure 6.10: Evolution of (a) eccentricity. (b) inclination of SUNSAT from epoch until 1st Nov. 2012



(a)



(b)

Figure 6.11: (a) Comparison in apogee height from epoch until 1st Nov. 2012. (b) Predicted decay date of SUNSAT at two solar activity levels using LIFTIM.

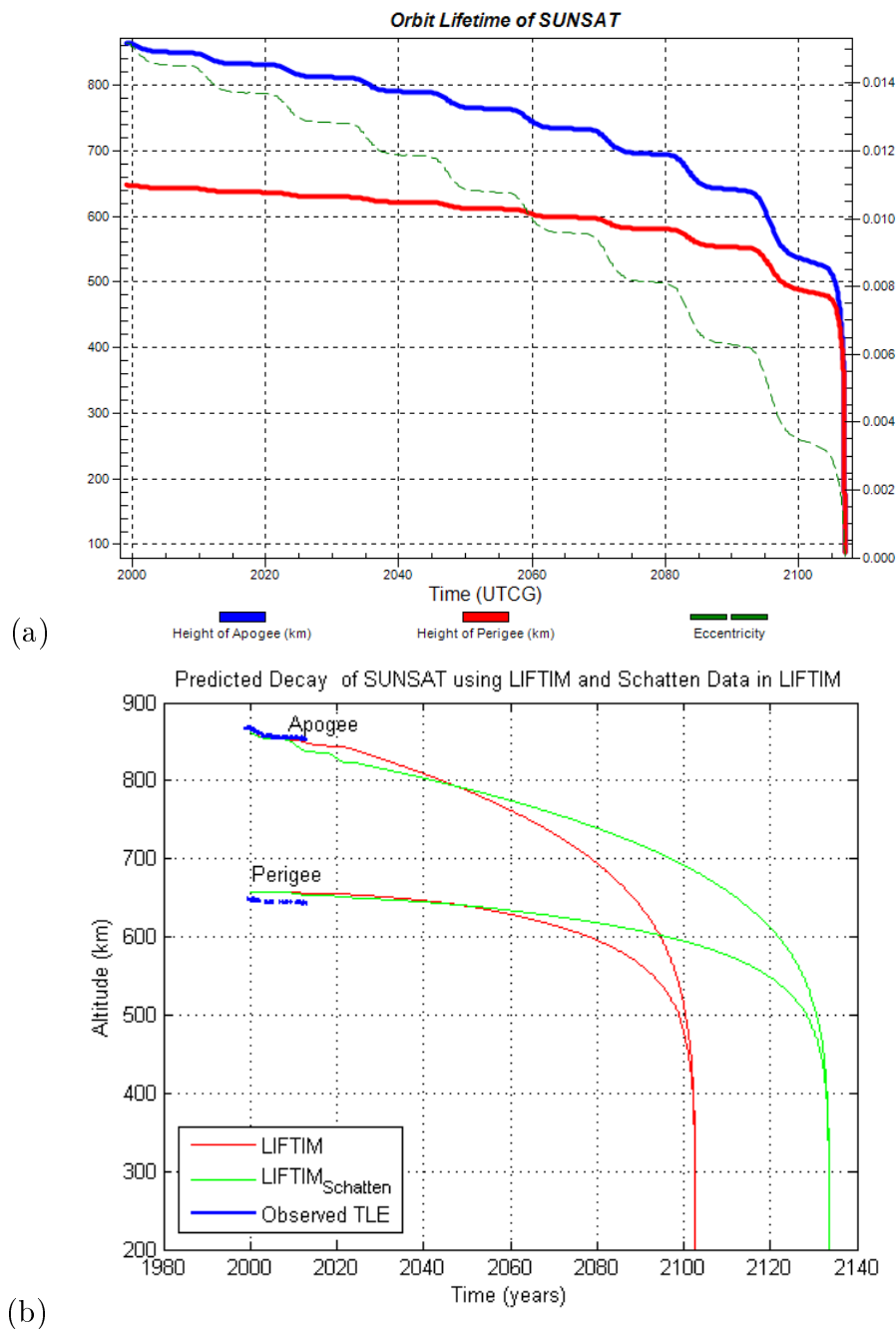


Figure 6.12: Predicted decay date of SUNSAT using (a) STK. (b) LIFTIM with and without Schatten solar flux data..

Resonance tides on a satellite modifies the orbit moving away from deep resonance, hence decreasing the orbital eccentricities from higher to lower values. For every sidereal day, the satellite passes over the same place on the Earth causing the satellite in what is called deep resonance with the Earth's gravity field [56]. Due to this resonance, the satellite experiences significant orbit perturbation. The effect of resonance tides on satellite orbits are changes in the eccentricity exhibited by long-term periodic variations [57]. The spectrum distribution is depicted in Figure 6.13 for a range of eccentricity values from epoch until

1st November 2012. The peak shows a sixty day variation in the eccentricity of SUNSAT.

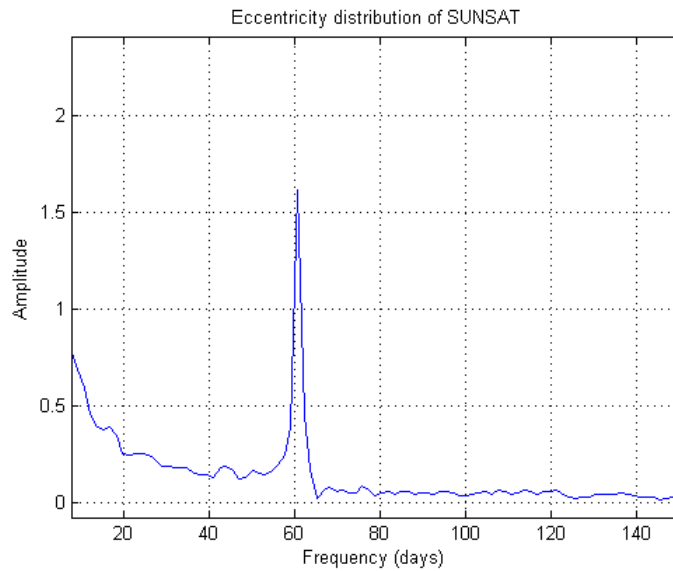


Figure 6.13: Spectrum distribution of eccentricity for SUNSAT.

SUNSAT's orbital elements were analysed. Eccentricity and semi-major axis show secular variations. The estimated orbit decay date using LIFTIM at two solar activity levels 95% (+2sigma) and 50% (nominal) are 2 July, 2034 and 15 August, 2101 respectively (Figure 6.11b). STK's predicted orbit decay date is 11 December, 2106 (Figure 6.12a). LIFTIM_{Schatten} is estimated as 29 January, 2136 (Figure 6.12b) as compared to the prediction using LIFTIM. The difference in prediction is about 34.5 years. The vast difference in predicted dates is attributed to the different methods used in the software packages as well as the recorded solar flux data used for both predictions. The influence of the 11 year solar cycle in atmospheric density is observed from the onset of predictions in Figures 6.11b, 6.12a, 6.12b.

6.3.4 1U CubeSAT (ZACUBE-01)

LIFTIM was also employed to predict the expected lifetime of ZACUBE-01. Although not yet launched, it is expected that, it will decay within 25 years. The simulation was executed over a period of one year from 1 October, 2012 at 10:00:00.000 UTCG to 1 October, 2013 at 10:00:00.000 UTCG (mission operation).

ZACUBE-01 is expected to operate at an altitude of about 600km. Periodic changes are observed in eccentricity and inclination as seen with STK predictions in Figures 6.14b and 6.15a. Eccentricity is zero, assuming ZACUBE-01 will be launched in a circular orbit.

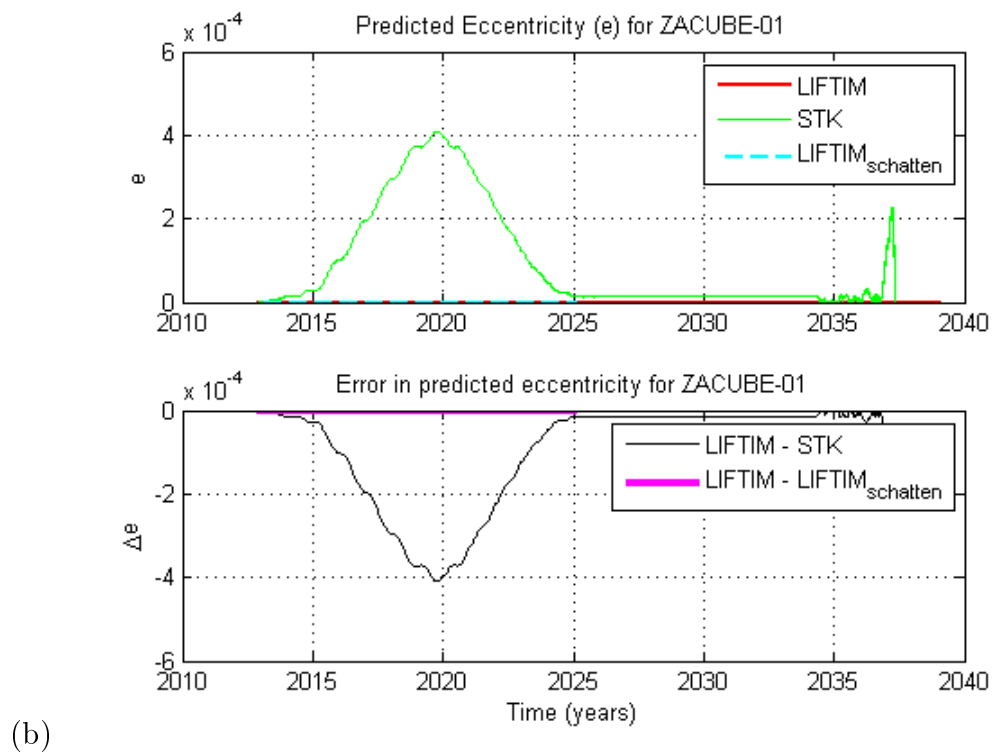
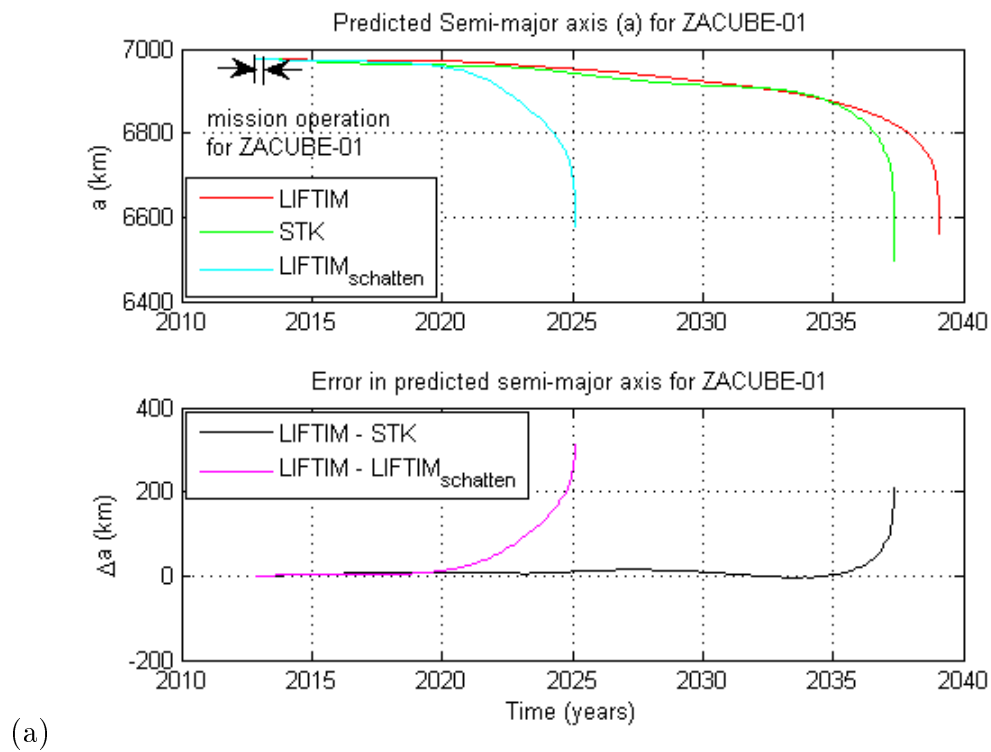


Figure 6.14: Evolution of (a) semi-major axis. (b) eccentricity of ZACUBE-01.

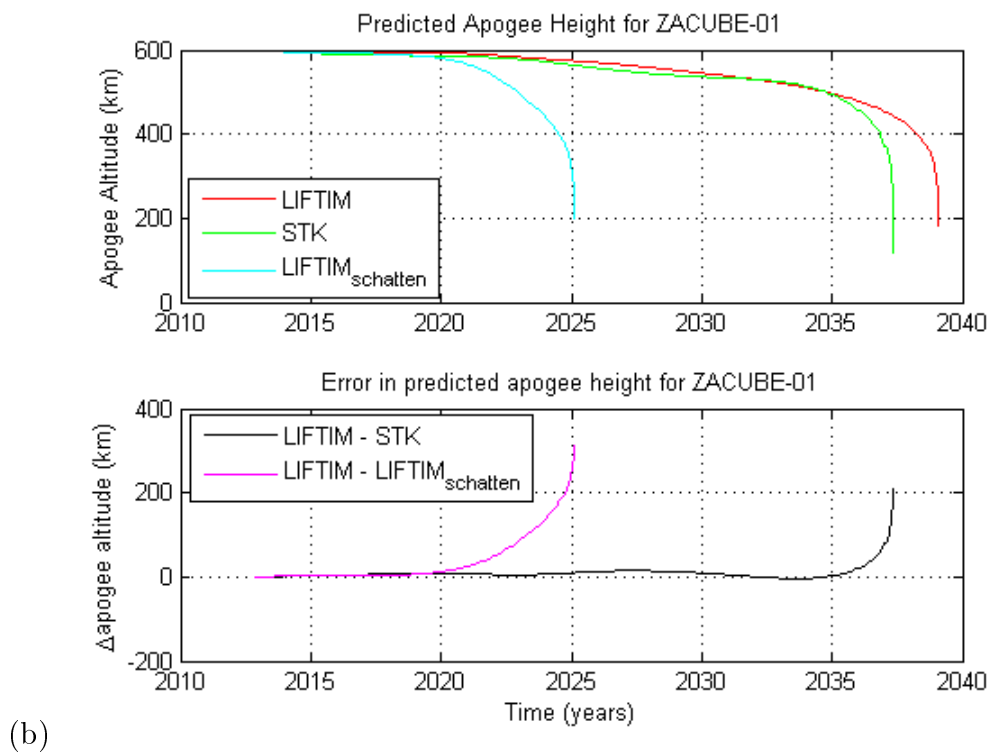
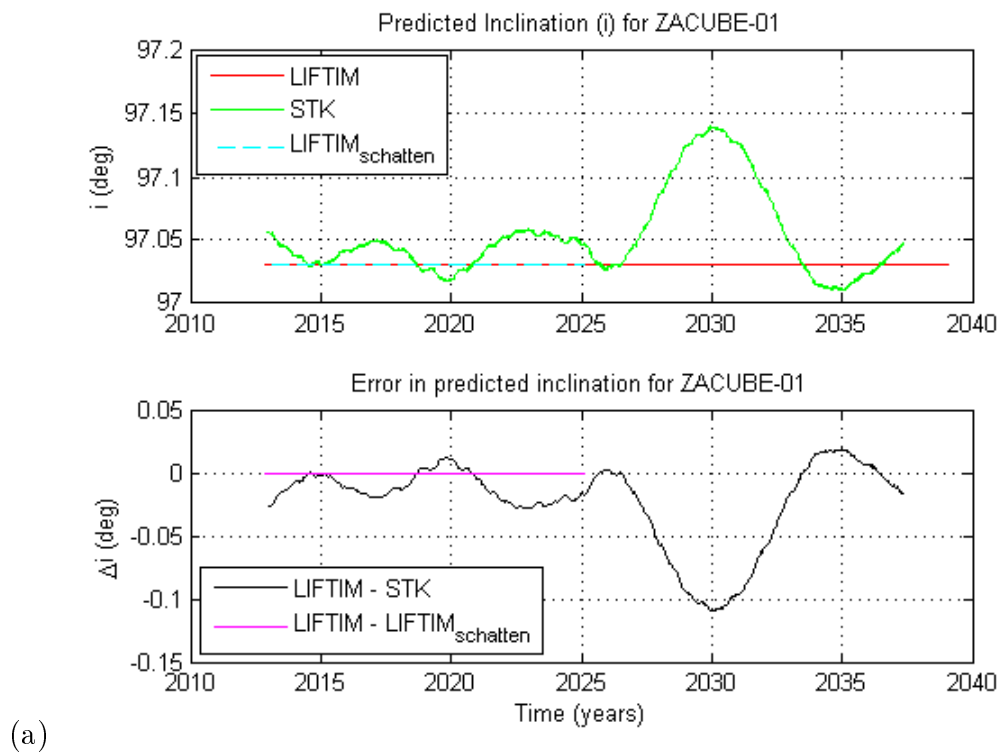
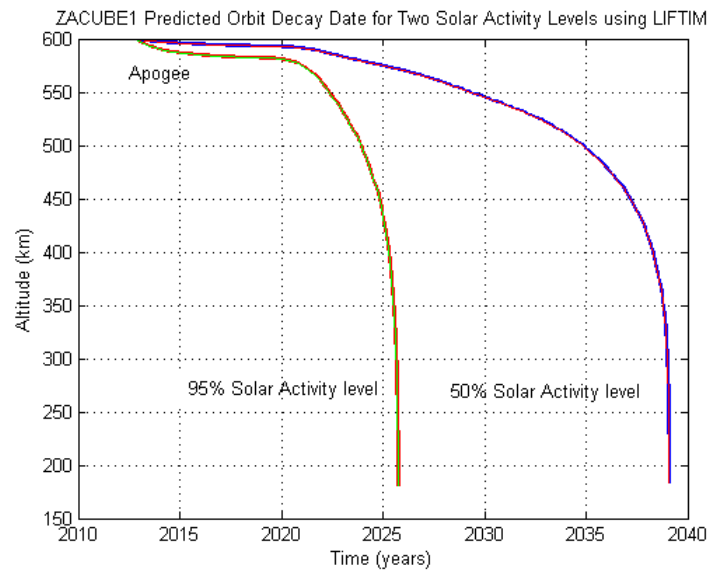
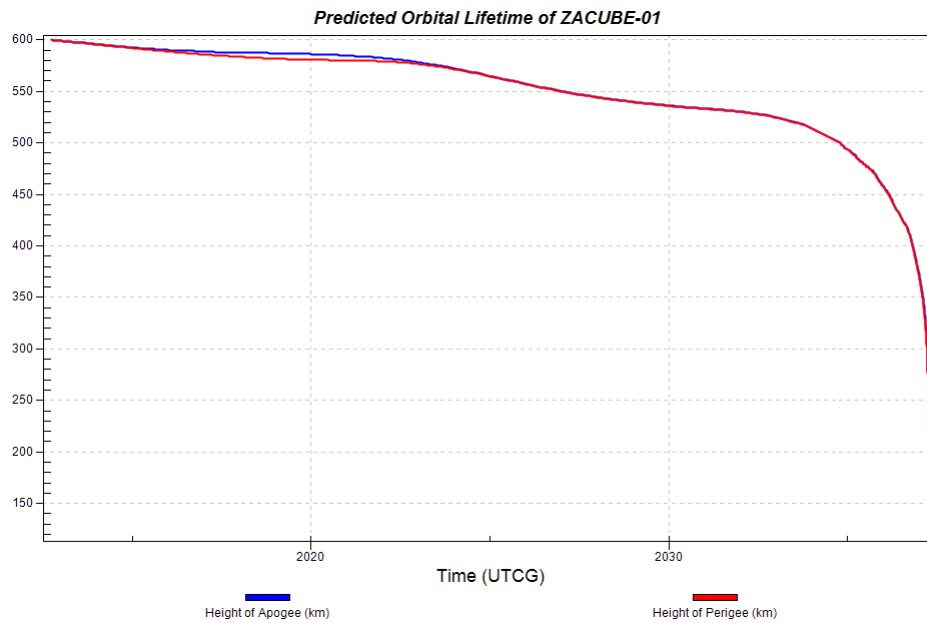


Figure 6.15: Evolution of (a) inclination. (b) apogee height of ZACUBE-01.



(a)



(b)

Figure 6.16: Predicted decay date of ZACUBE-01 (a) at two solar activity levels using LIFTIM. (b) STK.

A comparison of LIFTIM, STK and LIFTIM_{Schatten} was analysed for the evolved orbital parameters similar to the test case satellites (Figures 6.14 to 6.15). The respective decay dates using LIFTIM at two solar activity levels (Figure 6.16a) are 2 August, 2025 (95%) and 2 January, 2039 (50%). Figure 6.16b shows STK predicted orbit decay date of 13 April, 2037. The difference in both predictions (LIFTIM & STK) is estimated as 1.7 years and (LIFTIM & LIFTIM_{Schatten}) is 14 years considering 50% solar activity for LIFTIM. LIFTIM_{Schatten} predicted orbit decay date is 15 January, 2025 (Figure 6.17). Secular

variations are predominant in the semi-major axis.

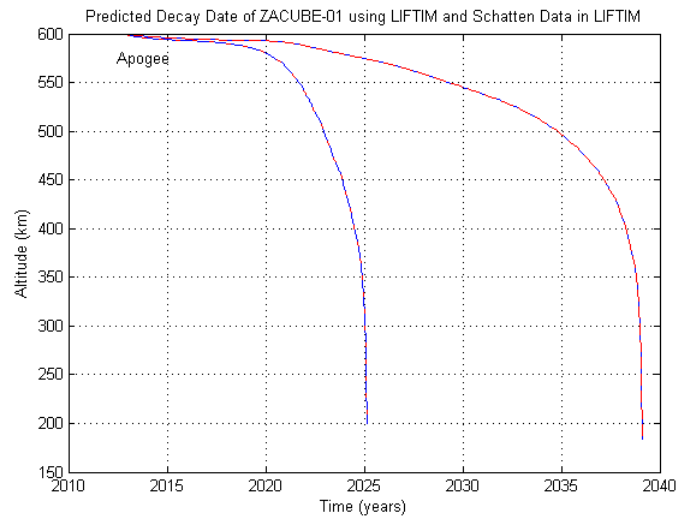


Figure 6.17: Predicted orbit decay of ZACUBE-01 with and without Schatten data.

6.4 Theoretical Decay Results using a DeOrbitSail Mechanism

The lifetime implication of a 10 m^2 drag sail deployed as a deorbiting mechanism was investigated for all the satellites under consideration, including ZACUBE-01. The effect of sail size as a function of initial altitude for masses between 200 kg and 1000 kg to deorbit within 25 years was analysed and is shown in Figure 6.18.

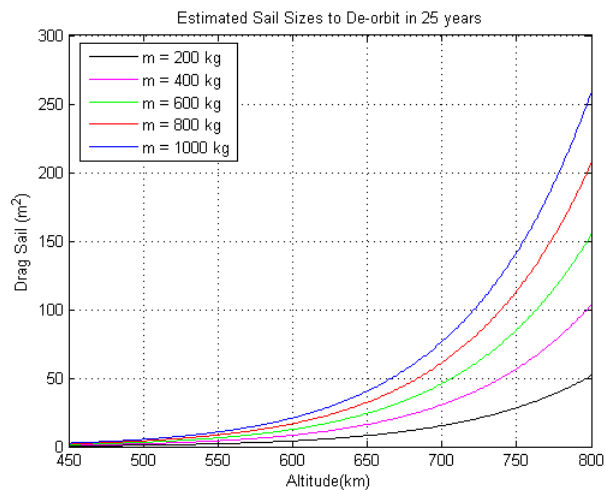


Figure 6.18: Estimates of sail size to deorbit in 25 years.

6.4.1 Iridium-85 Satellite

The predicted deorbit date for *Iridium-85* is 24 Dec. 2000 (LIFTIM). The deployment of a 10 m^2 drag sail mechanism would reduce its lifetime to 1.1 years (Figure 6.19).

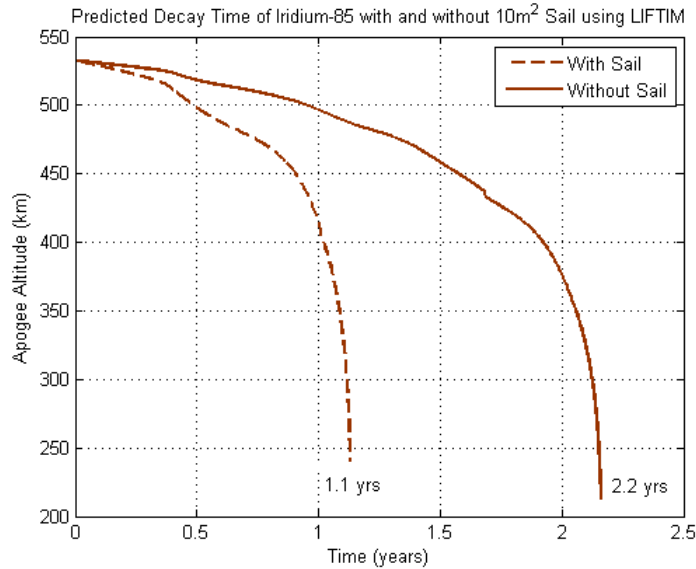


Figure 6.19: Predicted lifetime comparison of Iridium-85 with and without a 10 m^2 sail.

6.4.2 Starshine-1 Satellite

Figure 6.20 shows that, the predicted deorbit time for *Starshine-1* with a 10 m^2 sail is 33 days. The predicted decay time is 26 February, 2000 using LIFTIM.

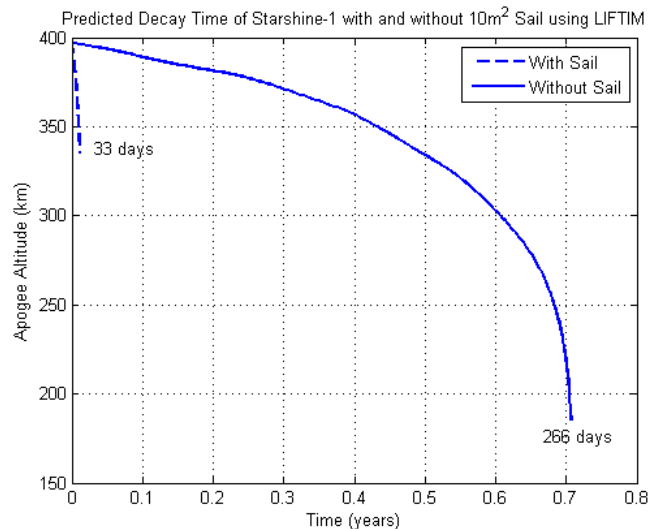


Figure 6.20: Predicted lifetime comparison of Starshine-1 with and without a 10 m^2 sail.

6.4.3 SUNSAT

The expected deorbit time for SUNSAT is about 102.4 years. Its expected lifetime prediction date is 15 August, 2101 at 50% solar activity level. The deployment of a drag sail would reduce its decay time significantly to about 6.7 years (Figure 6.21).

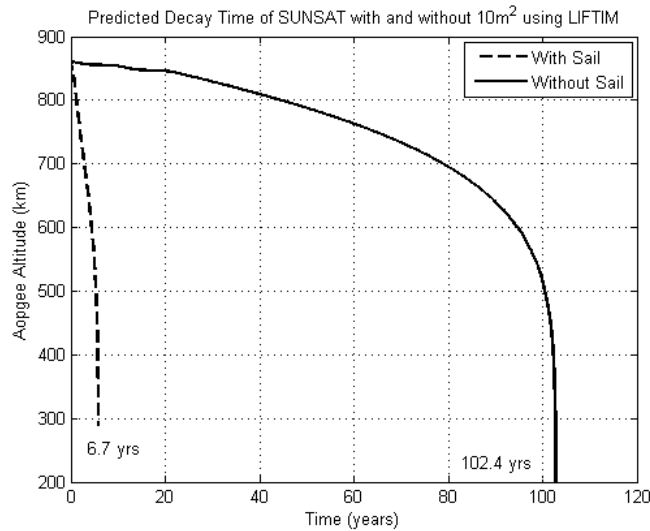


Figure 6.21: Predicted lifetime comparison of SUNSAT with and without a 10 m^2 sail.

6.4.4 1U CubeSAT (ZACUBE-01)

The predicted deorbit time for ZACUBE-01 is 111 days with a 10 m^2 drag sail as shown below (Figure 6.22).

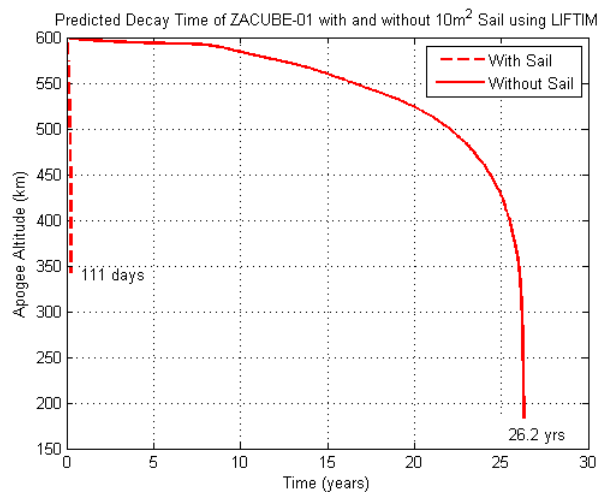


Figure 6.22: Predicted lifetime comparison of ZACUBE-01 with and without a 10 m^2 sail using LIFTIM.

Predictions involving STK software package with a 10 m^2 sail size are presented in Appendix D. The simulations performed within the main scenario conditions showed that, as expected, also in this case the deorbiting time is considerably reduced adopting the drag sail. However, the simulations showed relatively lesser deorbiting times (about 60%) than in LIFTIM. This could be due in part to the different decay algorithms used in both software packages. For ZACUBE-01 with a deorbit time of 25 days, the geometry and mass ($m = 1\text{ kg}$) are contributing factors. Also, it is assumed that the aerodynamic drag deorbiting was achieved when the drag force experienced by the $10 \times 10\text{ m}^2$ sail was maximised. This is as a result of the sail facing the velocity direction throughout the orbit (controlled attitude).

6.5 Discussion

6.5.1 Decay Predictions

Estimation of orbital lifetimes of *Iridium-85*, *Starshine-1*, SUNSAT and a 1U cubeSAT (ZACUBE-01) was performed. The results presented here show the effects of solar activity in predicting the end-of-life of a satellite. Atmospheric drag (below 1000 km) and Earth oblateness play a significant role in estimating lifetime predictions. Accurate drag coefficients are required for minimising propagation errors during long term evolution where atmospheric drag is dominant. Large position errors result from poor choice in drag coefficients employed in determining the lifetime of a satellite. Uncertainties in lifetime computations are also as a result of variations in the atmospheric density due to the difficulty in accurately predicting solar activity levels.

Historic TLE-derived orbital parameters were compared with the corresponding predicted values from the LIFTIM and STK software packages for the satellites under consideration. Secular variations were observed mostly in the semi-major axes and eccentricity. Periodic changes are dominant in eccentricity and inclination for the satellites. Taking into consideration the uncertainties in estimated drag coefficients and atmospheric density values, the behaviour of the predicted orbital elements compared favourably with that of the historic TLE-derived orbital elements. This gives an indication of the success of the SALT theory to predict the evolution of orbital parameters over a satellite's lifetime (Figures 6.1, 6.2, 6.5, 6.6, 6.9*b*, 6.10, 6.11*a*, 6.14, 6.15).

The predicted orbital parameters of the STK software package also do well in comparison with the TLE-observed orbital elements signifying the success of the lifetime theory in STK. The performance and accuracy of the lifetime theory in STK is dependent on the

Gaussian quadratures.

Figures 6.3a, 6.7a show the orbit decay prediction for *Iridium-85* and *Starshine-1* satellites using the LIFTIM software package at 50% (nominal) solar activity level and the optimised drag coefficients in Table 5.5. The nominal solar activity level was used since it was the best match for the observed decay dates of the satellites considered in this study. The predicted decay dates using LIFTIM differ by six (*Iridium-85*) and eighteen (*Starshine-1*) days from the observed decay dates as compared to that estimated by STK (Figures 6.3b, 6.7b) which differ by four (*Iridium-85*) and ten (*Starshine-1*) days respectively. The predicted time histories of perigee and apogee radii demonstrate the reduction of an elliptical orbit into a circular orbit under the influence of atmospheric drag. Comparisons in the apogee height of LIFTIM and STK software packages was analysed to show its long-term variation over a satellite's lifetime as presented in Figures 6.2b, 6.6b.

The predicted deorbit times for the test case satellites, SUNSAT and ZACUBE-01 as well as the difference in predictions for the software packages are presented in Tables 6.1 and 6.2.

Table 6.1: Predicted deorbit dates for test case satellites.

Satellite	Observed decay date	Predicted decay date (LIFTIM)	Predicted decay date (STK)	Predicted decay date (LIFTIM _{Schatten})	Difference (Observed and LIFTIM)	Difference (Observed and STK)	Difference (Observed and LIFTIM _{Schatten})	Difference (LIFTIM and LIFTIM _{Schatten})
Iridium-85	30 Dec.2000	24 Dec. 2000	26 Dec. 2000	20 April 2000	6 days	4 days	8 months	7 months
Starshine-1	18 Feb.2000	08 Mar. 2000	28 Feb. 2000	22 Dec. 2000	18 days	10 days	1.9 months	2.5 months

Simulations on the expected deorbit time for ZACUBE-01 is estimated at 24.5 years (STK), 26.2 years (LIFTIM) and 12.2 years (LIFTIM_{Schatten}) taking into account a 50% (nominal) solar activity level. Changes in the orbital elements over the lifetime period of ZACUBE-01 are presented in Figures 6.14 to 6.15.

The variations in the predicted decay dates using the Schatten solar flux data in the LIFTIM software package is as a result of large variations in the solar activity data due to the methods employed in obtaining the different sets of data. Although, both sets of data are good, it would be more appropriate to use one's data set for predictions than to employ another data set thus, the two solar data sets for LIFTIM and STK should not be interchanged.

Table 6.2: Predicted deorbit dates & time for SUNSAT and ZACUBE-01.

Satellite	Predicted decay date (LIFTIM)	Predicted decay date (STK)	Predicted decay date (LIFTIM _{Schatten})	Predicted decay time (LIFTIM)	Predicted decay time (STK)	Predicted decay time (LIFTIM _{Schatten})	Difference (LIFTIM and STK)	Difference (LIFTIM and LIFTIM _{Schatten})
SUNSAT	15 Aug. 2101	11 Dec. 2106	29 Jan. 2136	102.4 yrs	107.7 yrs	136.9 yrs	5.3 yrs	34.5 years
ZACUBE-01	2 Jan. 2039	13 Apr. 2037	15 Jan. 2025	26.2 yrs	24.5 yrs	12.2 yrs	1.7 yrs	14 years

The predicted orbit decay dates for the satellites using $LIFTIM_{Schatten}$ are 20 April 2000 (*Iridium-85*), 22 December 1999 (*Starshine-1*), 29 January 2136 (SUNSAT) and 15 January 2025 (ZACUBE-01) as shown in Figures 6.4, 6.8, 6.12b, and 6.17 respectively. These dates differ by 7 months, 2.5 months, 34.5 years and 14 years respectively for *Iridium-85*, *Starshine-1*, SUNSAT and ZACUBE-01 satellites, considering the predicted decay dates by LIFTIM. Variations in some of the orbital elements are depicted above for the various satellites. The respective quantitative difference for $LIFTIM_{Schatten}$ showed large errors (Figures 6.1a, 6.2b, 6.10a, 6.11a, 6.14a, 6.15b) as compared to that of LIFTIM and STK. The predicted deorbit dates and times considering $LIFTIM_{Schatten}$ were “shorter” (under estimated) compared to the observed deorbit times in most cases as a result of different solar flux data employed.

The performance of the lifetime models match quite well for long-duration predictions. This may be attributed in part to LIFTIM and STK’s ability to combine sophisticated atmospheric models and integration routines with self-consistent drag coefficients for each satellite.

Accurate prediction of a satellite’s lifetime is based on the solar heating parameters ($F_{10.7}$ and A_p), atmospheric density and ballistic coefficient. But in the absence of precise attitude information, estimates of satellite parameters are used to obtain a mean value for the ballistic coefficient [1]. The consequence of uncertainties in the predicted solar heating parameters are accommodated in the choice of the solar and magnetic index parameters at the three different solar activity levels (Figures 4.3 and 4.4).

6.5.2 Effects of the DeOrbitSail Mechanism

A drag sail involves passive technology as the unfolding of the sail is the only activity. In Figure 6.18, we observe a nonlinear behaviour in drag sail, hence sail sizes could be limited for satellites with low mass and low altitude missions.

The concept of using a drag sail as, a solution for deorbiting satellites is evident from Figures 6.19 to 6.22. The predicted lifetimes of the test case satellites reduced signifi-

cantly to 1.1 years (*Iridium-85*) and 33 days (*Starshine-1*) respectively if a sail had been used. Similarly, the deorbit times for SUNSAT and ZACUBE-01 at their present altitude utilising LIFTIM is more than the 25 year regulation. However, in the drag sail mode, the deorbit time reduced to about 6.7 years and 111 days as shown in Figures 6.21 and 6.22 respectively. When drag sails are attached to spacecraft, they affect the ballistic coefficient of the spacecraft after deployment, causing rapid deorbiting thus drag sails can be used as a deorbiting device.

In conclusion, the use of sails can be an advantageous low-cost solution for deorbiting satellites, as the total cost of this technology is not prohibitive. For certain missions, drag sails may be a better solution than the traditional propulsion systems [28].

6.6 Summary

The results obtained in this chapter shows the various decay prediction dates using the lifetime tool package for LIFTIM and STK. The predicted decay dates compared favourably to the observed decay dates. Variations in the predicted and TLE-derived orbital elements were established for the satellites considered in this study. Predictions of satellite lifetimes are dependent on accurately determining atmospheric density models, solar heating parameters and the ballistic coefficients.

The effects of using sails as a deorbit solution is presented. The reduced lifetimes for the satellites under consideration show the overall importance of deploying a sail on a satellite which causes rapid deorbiting. Tables 6.3 and 6.4 gives an overview of the deorbiting times for the satellites using both LIFTIM and STK software packages.

Table 6.3: LIFTIM predicted orbital lifetime with and without a deorbit sail.

Satellite	Initial Mean Altitude (km)	Mass (kg)	Predicted deorbit time without a sail	Predicted deorbit time with 10 m^2 sail (LIFTIM)
Iridium-85	550	689	2.2 yrs*	1.1 yrs
Starshine-1	400	39	266 days*	33 days
SUNSAT	870	63	102.5 yrs	6.7 yrs
ZACUBE-01	600	1	26.2 yrs	111 days

* Observed deorbit time

Table 6.4: STK predicted orbital lifetime with and without a deorbital sail.

Satellite	Initial Mean Altitude (km)	Mass (kg)	Predicted deorbit time without a sail	Predicted deorbit time with 10 m^2 sail (STK)
Iridium-85	550	689	2.2 yrs *	355 days
Starshine-1	400	39	266 days *	18 days
SUNSAT	870	63	107.7 yrs	3.5 yrs
ZACUBE-01	600	1	24.5 yrs	25 days

* Observed deorbit time

Chapter 7

Conclusion and Future Work

This chapter summarise the content of this study and the overall perspective of this work is established. The most significant assumptions and simplifications that were made in the previous chapters are summarised and results evaluated against the initial objectives of this study. Conclusions are drawn from the results obtained, with further recommendations based on the results and observations presented.

The objectives as formulated in Chapter one, are repeated here for reference:

1. Investigate the accuracy of predicted orbital element evolution over (test) satellite's lifetime (re-entry date).
2. Investigate the effects of perturbations on time evolution of satellite orbital elements and orbital lifetime of SUNSAT.
3. Test the theory and long-term predicted solar and magnetic data sets by implementing relevant algorithms and software packages and comparing the theoretical results with observed/ historic TLE-derived orbital parameters.
4. Investigate the DeOrbitSail mission to reduce the lifetime of satellites with regards to deorbiting using aerodynamic drag.

The following sections summarises the results of the study with reference to the above objectives.

7.1 Summary of Study

7.1.1 Lifetime Predictions

Two lifetime prediction models, the Semi-Analytical Liu Theory (SALT) and Satellite ToolKit (STK) were used in this study. Liu's theory utilised the variational equations of motion for the orbit mean elements due to the Earth's oblateness and atmospheric drag only. The satellite toolkit used an n 9-point Gaussian quadrature which integrates the slowly varying orbital elements over time by integrating over one orbit to determine the rate-of-change of each variable. A theoretical and numerical foundation of the SALT is presented in Chapter 4 and provides an efficient simulation tool used in this study.

The first important aspect in the decay process was established and it was shown that, two separate parameters (atmospheric drag and earth oblateness) are the main forces which influences the decay of near Earth satellites. The perturbing effects on time evolved orbital elements showed that, atmospheric drag leads to decreasing values of eccentricity (e) and semi-major axis (a). Apart from the effects on a and e , the perturbation in the trajectory was also observed in other orbital elements such as the inclination (i) as observed in the TLE-derived historic orbital elements and predictions using the STK software package. Variations in apogee (r_a) and perigee radius (r_p) are bound to affect an orbit substantially. The apogee and perigee heights are functions of a and e , hence oscillations induced in these two elements produce a faster decrease in r_a than in r_p (due to the secular reduction in eccentricity) associated with a lower r_a which will cause a satellite to ultimately enter the lower atmosphere.

The accuracy of both models was considered next. The software packages were first evaluated against the actual orbit decay histories of the test case satellites (*Iridium-85 and Starshine-1*) prior to applying the solution to SUNSAT's orbit. The comparative small differences between the predicted and TLE-observed deorbit dates for the test case satellites, demonstrated the success of the LIFTIM and STK in predicting satellite lifetime for these satellites. According to Liu's theory [1], variations in the solar heating parameters coupled with satellite's ballistic coefficient are of greater importance on the prediction accuracy of a satellite's life span.

A quantitative comparison of the orbital parameters was investigated for the satellites involved. This showed the error difference in predictions between the actual TLE decay histories and the software packages. The relatively small errors gives an indication of the performance of the software packages. The evolution of the orbital elements other than the cartesian position of the satellites over their lifetimes was used due to the long orbital

lifetime. The effects of resonance on a satellite's orbit causes variations in the eccentricity as well, exhibited by long-term periodic changes. It must be kept in mind that, this also decreases the orbital eccentricities from higher to lower values causing significant orbit perturbations.

Lifetime predictions depend primarily on the solar heating parameters as well. In order to employ the Schatten solar flux data in LIFTIM, a comparative analysis on the solar flux data for both LIFTIM and STK was considered. By utilising the Schatten solar data in the LIFTIM model, it was hoped to eliminate some uncertainties in the prediction performance by LIFTIM and STK since they use different prediction algorithms and different predicted solar data sets by letting both models use the same solar data.

The predictions obtained using the Schatten solar flux data set in the LIFTIM prediction tool showed large variations in the estimated decay dates compared to the observed TLE. The lifetime theory employed in LIFTIM is different compared to STK which uses n 9 Gaussian quadrature for drag integration. Judging by the large variances resulting from $LIFTIM_{Schatten}$, compared to the "good" correspondence when STK and LIFTM use their own data sets, the difference lie in the respective algorithms. Hence, it would be more appropriate to use one's data set for predictions than to employ another data set (the two solar data sets thus LIFTIM and STK should not be interchanged). A pictorial diagram of lifetime estimation process is shown in Figure 7.1.

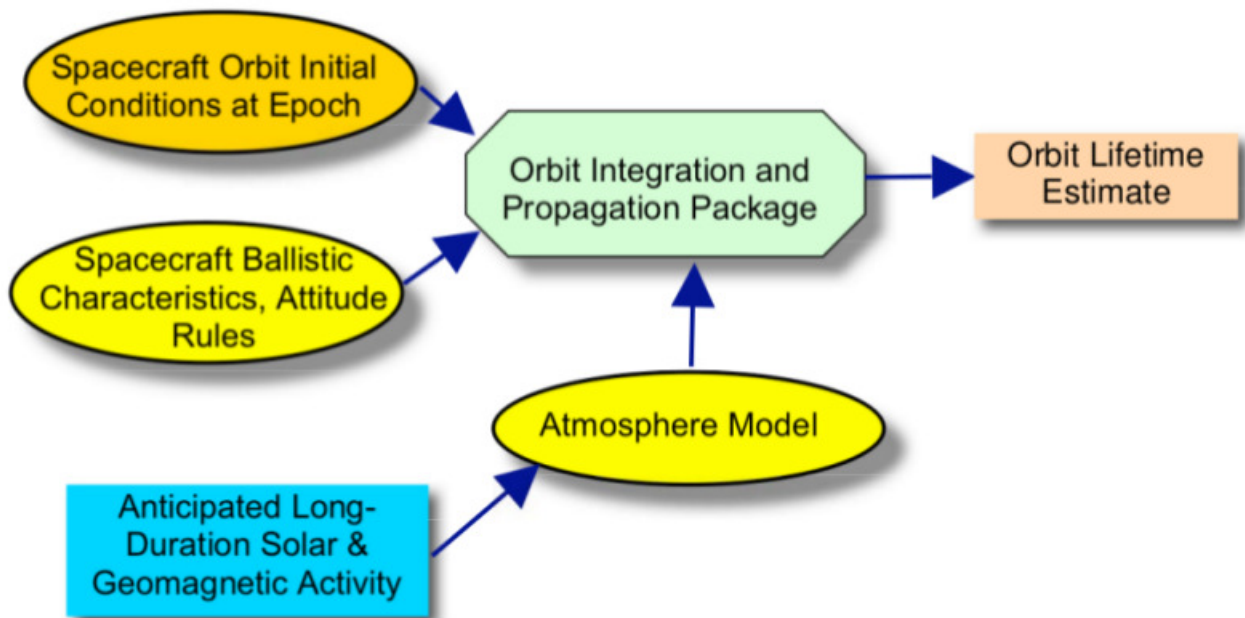


Figure 7.1: Orbit lifetime estimation process [7].

Finally, depending on solar activity levels thus 95% (+2sigma) and 50% (nominal), the estimated lifetime for SUNSAT according to Liu's theory is between 35 and 103 years. ZACUBE-01 expected lifetime is between 13 and 27 years. STK's estimated lifetime for SUNSAT is 107.7 years and ZACUBE-01 is 24.5 years.

7.1.2 DeOrbitSail Mechanism

The deorbital sail concept was investigated. The primary aim was to demonstrate the concept of end-of-life deorbiting using a sail membrane ($10 \times 10 \text{ m}^2$) as a drag sail. We observed that, in the drag sail mode the satellites have shorter predicted lifetimes than without a sail. This demonstrated that drag sails could subsequently be used as a deorbiting device for rapid deorbiting. This technology shows the readiness level of drag sails and hence can be adapted for use on satellites in the future. The sail deployment can be used as a low cost solution to reduce the accumulation of space debris in the near future. Appendix E shows a configuration (stowed and deployed) of a sail membrane.

7.2 Conclusion

In this thesis, the feasibility of predicting satellite lifetimes in LEO by employing two separate software packages was established. More importantly, investigating the effects of orbital perturbations on the time evolution of the satellite orbital elements and orbital lifetime of SUNSAT was ascertained.

The efficiency of satellite lifetime predictions depend on the ability to estimate many variables in combination with sophisticated atmospheric models. These models, though highly recommended, are still inadequate to account for all the variations of the satellite's environment that affects the lifetime of satellites especially when using uncertain predicted values. Studies in atmospheric density modelling, estimation of drag coefficient and their effects on atmospheric drag have produced notable advances in orbital lifetime estimation models.

LIFTIM and STK prediction tools has been found to be a simplified yet rather accurate tool in the continuing effort of understanding and estimating a satellite's orbital life. It also illustrates greater significance on prediction accuracy taking into account the atmospheric density model.

The deorbital sail technique allowed for safe deorbiting of spacecraft at the end of their lifetime. It also addressed the challenge of continual growth of space debris in LEO by

employing sizeable ($10 \times 10 \text{ m}^2$) drag sails to help reduce the accumulation of “space junk” in the near future. We also demonstrated that, in a drag sail mode, rapid deorbiting is enhanced.

7.3 Further Research and Recommendation

The following considerations must be taken into account for improvements in the prediction process;

- The accuracy and execution speed of the numerical integration algorithm of Liu’s model could be compensated by using higher order integrators such as Adams-Bashforth etc.
- The atmospheric density model (Jacchia-70) could also be replaced with a more sophisticated and accurate model.
- A dedicated drag analysis study could be investigated for each satellite based on the geometry, orbital regime and environmental conditions to be used in the prediction theory or algorithm.
- The need for an improved LIFTIM algorithm.

The performance of Liu’s theory should be evaluated for a variety of orbit classes and satellite lifetimes.

The concept of the deorbital sail mechanism could be further expanded by looking at alternatives towards finding a scalable solution for drag sails depending on the size and mass of the satellite.

Bibliography

- [1] J. J. F. Liu, R. L. Alford, *The Orbit Decay and Lifetime (LIFTIM) Prediction Program*. Northrop Services, Inc., Hunstville, Ala., M-240-21278, May, 1974.
- [2] B. Hofmann-Wellenhof, H. Lichtenegger, W. Wasle, *GNSS - Global Navigation Satellite Systems, GPS, GLONASS, Galileo and more*. 1st ed. New York: Springer-Verlag Wien, 2008.
- [3] V. A. Chobotov, *Orbital Mechanics*, 3rd ed. AIAA Educational Series, Reston, Virginia, VA, 2002.
- [4] D. A. Vallado, *Fundamentals of Astrodynamics and Applications*. Space Technology Series, McGraw-Hill Custom Publishing, New York, 1997.
- [5] J. J. Sellers, W. J. Larson, R. B. Giffen, W. J. Astore, *Understanding Space: An Introduction to Astronautics*. Revised 2nd ed. Space Technology Series, McGraw-Hill Custom Publishing, New York, NY, 2004.
- [6] R. Bate, D. D. Mueller, J. E. White, *Fundamentals of Astrodynamics*. 1st ed, Dover Publications, Inc, New York, NY, 1971.
- [7] Space Systems, *Determining orbit lifetime*, ISO copyright office, CH-1211, ISO/TC 20/SC 14 27852, Geneva20, 2007.
- [8] [Online]. Available: <http://sail.msfc.nasa.gov/nse/solar.html>. [accessed 3 March, 2012].
- [9] R. Sandau, K. Brieß., *Reasons for satellite mission miniaturisation and its consequences*. Acta Astronautica, Elsevier, Vol 43, Issues 11 -12, 1998, pp. 583 - 596, [http://dx.doi.org/10.1016/S0094-5765\(99\)00007-7](http://dx.doi.org/10.1016/S0094-5765(99)00007-7).
- [10] T. S. Kelso, NORAD Two-Line Element Sets, Current Data. [Online]. Available: <http://celestrak.com/NORAD/elements/>. [accessed 20 August, 2011].

- [11] [Online]. Available: <https://www.space-track.org/perl/home.pl>. [accessed 3 April, 2012].
- [12] B. D. L. Opperman, *Precision Propagation and Orbit Decay Prediction of Low Earth Orbit Satellites*. M.Sc. Thesis. University of Stellenbosch, Stellenbosch, South Africa, 2003.
- [13] F. R. Hoots, R. L. Roehrich, T. S. Kelso, *Models for Propagation of NORAD Element Sets*. Spacetrack report no.3. Defense Documentation Center Cameron Station, Alexandria, VA 22314. 1988.
- [14] H. Klinkrad, *Space Debris - Models and Risk Analysis*. Springer, Verlag, Berlin, Heidelberg, New York. 2006.
- [15] J. C. Liou, N. Johnson, N. Hill, *Controlling the Growth of Future LEO Debris Population with Active Debris Removal*. Acta Astronautica, Vol. 66 No. 5-6, 2010, pp. 648-653, doi:10.1016/j.actaastro.2009.08.05. [accessed 15 February, 2012]
- [16] NASA HANDBOOK, *Handbook for Limiting Orbital Debris: Measurement System Identification metric*. [Online]. Available: <http://www.hq.nasa.gov/office/codeq/doc-tree/NHBK871914.pdf>. [accessed 6 November, 2011]
- [17] Anon., Inter-Agency Space Debris Coordination Committee, *Space Debris Mitigation Guidelines*. Issue 1, Rev.1, 2002a.
- [18] NASA Safety Standard: *Guidelines and Assessment Procedures for Limiting Orbital Debris*. NSS 1740.14. August, 1995.
- [19] J-C. Liou, N. L. Johnson, *Risks in Space from Orbiting Debris*. Science, Vol. 311, pp. 342 - 341, 20th January, 2006.
- [20] Anon., *Monthly Number of Cataloged Objects in Earth Orbit by Object Type*. Chart, The Orbital Debris Quartely News, NASA JSC , p.10, January 2011. [Online]. Available: <http://www.orbitaldebris.jsc.nasa.gov/newsletter/pfds/ODQNv15i1.pdf>. [12 April, 2012]
- [21] H. Klinkrad, P. Beltrami, S. Hauptmann, C. Martin, H. Sdunnus, H. Stokes, R. Walker, J. Wilkinson, *ESA Space Debris Mitigation Handbook*. Advances in Space, Vol. 34, Issue 5, pp 1251- 1259, 2004. <http://dx.doi.org/10.1016/j.asr.2003.01.018>.
- [22] NASA Orbital Debris Program Office, *Orbital Debris Mitigation*. [Online]. Available. <http://www.orbitaldebris.jsc.nasa.gov/mitigate/mitigation.html>. [accessed 10 September, 2011]

- [23] U. S. Government Orbital Debris Mitigation Standard Practices. [Online]. Available. http://orbitaldebris.jsc.nasa.gov/library/USG_OD_Standard_Practices.pdf. [15 January, 2012]
- [24] Federal Communications Commission, In the Matter of Mitigation of Orbital Debris. FCC 04-130, Washington, DC, pp. 2, June 2004.
- [25] C. R. McInnes, *Solar Sailing: Orbital Mechanics and Mission Applications*. Advance in Space Research, Vol. 31, No. 8, pp. 1971 - 1980, 2003.
- [26] C. R. McInnes, *Solar Sailing: Technology, Dynamics and Mission Applications*, Springer-Verlag Series in Space Science and Technology, Springer-Verlag, Praxis, 1999.
- [27] B. Wie, *Solar Sail Attitude Control and Dynamics*, Parts 1 and 2. Journal of Guidance, Control and Dynamics, Vol. 27, No.4, pp. 526- 544, July-August, 2004.
- [28] V. Lappas, N. Adeli, L. Visagie, J. Fernandez, T. Theodorou, W. Steyn, M. Perren, *CubeSail: A low cost CubeSat based solar sail demonstration mission*. Advances in Space Research, 48 , pp. 1890 - 1901. 2011. <http://doi:10.1016/j.asr.2011.05.033>.
- [29] J. Amos, *Mini-camera pictures Japan's Ikaros solar sail*. [Online]. Available. <http://www.bbc.co.uk/news/10328584>. [12 April, 2012]
- [30] J. R. Wertz, D. F. Everett, J. J. Puschell, *Space Mission Engineering: The New SMAD*, Space Technology Library, Microcosm Press, Hawthorne, CA, 2011.
- [31] K. Alfriend, S. R. Vadali, P. Gurfil, J. How, L. Breger, *Spacecraft Formation Flying: Dynamics, Control, and Navigation*. 1st ed, Elsevier Astrodynamics Series, Butterworth-Heinemann Publication, 2010.
- [32] F. R. Hoots, R. L. Roehrich, T. S. Kelso, *Models for Propagation of NORAD Element Sets. Spacetrack report no. 3*. Defense Documentation Center Cameron Station Alexandria VA 22314. 1988.
- [33] D. G. King-Hele, *Satellite Orbits in an Atmosphere, Theory and Applications*. Blackie and Sons Ltd, pp 10 - 11, 1987.
- [34] P. R. Escobal, *Methods of Orbit Determination*, 2nd ed, Krieger Publishing Company, Malabar, Florida, 1985.
- [35] [Online]. Available: www.fas.org/spp/guide/china/earth/fy-1.htm. [accessed 18 May, 2012].

- [36] O. Montenbruck, E. Gill, *Satellite Orbits: Models, Methods, Applications*. 1st ed, Springer, 2000.
- [37] K. E. Tsiolkovsky, *Extension of Man into Outer Space*, 1921 [also, Tsiolkovsky, K. E., *Symposium Jet Propulsion*, No. 2, United Scientific and Technical Presses, 1936].
- [38] K. Tsander, *From a Scientific Heritage*, NASA Technical Translation TTF-541, 1967 [quoting a 1924 report by the author].
- [39] [Online]. Available: www.nasa.gov/mission_pages/smallsats/11-148.html. [accessed 20 October, 2011].
- [40] J. J. F. Liu, *A Second-order Theory of an Artificial Satellite under the Influence of the Oblateness of the Earth*. AIAA 12th Aerospace Sciences meeting, AIAA paper, pp. 74 - 166, January, 30 - February 1st, 1974.
- [41] J. J. F. Liu, R. L. Alford, *An Introduction to Gauss-Legendre Quadrature*, Northrop Services, Inc., Huntsville Ala., M-240-1288, October, 1973.
- [42] FP7 DeOrbitSail Kickoff Meeting, University of Surrey, Guildford, Surrey, United Kingdom, June 3, 2011.
- [43] NASA Orbital Debris Program Office, *Orbital Debris Remediation*. [Online]. Available: <http://www.orbitaldebris.jsc.nasa.gov/Remediation/remediation.html>. [15 May, 2012].
- [44] Analytical Graphics, Inc. [Online]. Available: <http://www.agi.com/products/stk/Default.aspx>. [accessed 20 October, 2012].
- [45] Analytical Graphics, Inc. [Online]. Available: <ftp://ftp.agi.com/pub/DynamicEarthData/>. [accessed 20 October, 2012].
- [46] Analytical Graphics, Inc. [Online]. Available: <http://www.agi.com/resources/help/online/stk/source/stk/importfiles-15.htm>. [accessed 20 October, 2012].
- [47] Analytical Graphics, Inc. [Online]. Available: <http://www.agi.com/resources/help/online/stk/source/stk/tools-11.htm>. [accessed 20 October, 2012].
- [48] [Online]. Available: www.swpc.noaa.gov/ftpmenu/indices/old_indices.html. [5 October, 2012].
- [49] K. O. Niehuss, H. C. Euler, W. W. Vaughan, *Statistical Technique for Intermediate and Long-Range Estimation of 13-Month Smoothed Solar Flux and Geomagnetic Index*. NASA Technical Memorandum 4759, Marshall Space Flight Center. MSFC, Alabama 35912. September, 1996.

- [50] [Online]. Available: [www.cput.ac.za/files/images_folder/news/news/newsletters/moja/Moja %20Newsletter%20October%202011.pdf](http://www.cput.ac.za/files/images_folder/news/news/newsletters/moja/Moja%20Newsletter%20October%202011.pdf). [20 October, 2012].
- [51] J. J. F. Liu, R. L. Alford, *Semi-analytic Theory for a Close-Earth Artificial Satellite*. Journal of Guidance and Control, Vol 3, No. 6, pp. 304-311, July-Aug, 1980.
- [52] J. J. F. Liu, *Satellite Motion About an Oblate Earth*. AIAA Journal, Vol. 12, pp. 1511-1516, Nov. 1974.
- [53] Y. Kozai, *The Motion of a Close Earth Satellite*. Astronomical Journal, Vol. 64, pp. 367, Oct. 1959.
- [54] D. Brouwer, *Solution of the Problem of Artificial Satellite Theory Without Drag*. Astronomical Journal, Vol 64, pp. 378-397, Nov. 1959.
- [55] H. D. Curtis., *Orbital Mechanics for Engineering Students*. 2nd ed, Elsevier Aerospace Engineering Series, Butterworth-Heinemann, Burlington, MA 01803, USA, 2010.
- [56] [Online]. Available: www.positim.com/navsys_overview.html. [10 November, 2012].
- [57] C. C. Chao, R. A. Gick., *Long-term evolution of navigation satellite orbits: GPS/GLONASS/GALILEO*. Advances in Space Research, Vol. 34, 1221-1226, 2004.

Appendix A

Derivation of Equations of Motion

This chapter contains the mathematical derivations of the two-body problem and constants of motion, as described in chapter 3.

A.1 Two-Body Problem

The two-body motion is derived according to the assumptions stated in section 3.2.1. Consider a system of two bodies of masses, M and m , as illustrated in Figure 3.3. Their position vectors with respect to an inertial frame are \mathbf{R}_M and \mathbf{R}_m .

The general two-body problems results if $\mathbf{R} \neq 0$ [3]. Then for mass, M ,

$$M\ddot{\mathbf{R}}_M = \frac{GMm\mathbf{R}}{R^3} \quad (\text{A.1})$$

and for mass, m ,

$$m\ddot{\mathbf{R}}_m = -\frac{GMm\mathbf{R}}{R^3} \quad (\text{A.2})$$

Subtracting equations. (A.2) from (A.1) yields

$$\ddot{\mathbf{R}} = -\frac{G(M+m)}{R^3}\mathbf{R} \quad (\text{A.3})$$

In a restricted two-body problem the principal mass M is assumed fixed in inertial space and $m \ll M$, so that m does not affect the motion of M [3]. Define the gravitational

parameter μ with $G(M + m) \cong GM = \mu$. Therefore, from equation (A.3), therefore [3]

$$\ddot{\mathbf{R}} + \frac{GM\mathbf{R}}{R^3} = 0 \quad (\text{A.4})$$

$$\ddot{\mathbf{R}} + \frac{\mu}{R^3}\mathbf{R} = 0 \quad (\text{A.5})$$

where $\mu \equiv GM$, thus the gravitational parameter.

A.2 Specific Mechanical Energy is a Constant

The two-body equation of motion is given by equation (3.2) as

$$\ddot{\mathbf{R}} + \frac{\mu}{R^3}\mathbf{R} = 0$$

take the dot product of both sides with $\dot{\mathbf{R}}$ [5],

$$\dot{\mathbf{R}} \bullet \left(\ddot{\mathbf{R}} + \frac{\mu}{R^3}\mathbf{R} \right) = \dot{\mathbf{R}} \bullet 0$$

or

$$\dot{\mathbf{R}} \bullet \ddot{\mathbf{R}} + \frac{\mu}{R^3}\mathbf{R} \bullet \dot{\mathbf{R}} = 0 \bullet \dot{\mathbf{R}} = 0$$

note: $\dot{\mathbf{R}} = \mathbf{V}$ and $\ddot{\mathbf{R}} = \dot{\mathbf{V}}$ so

$$\mathbf{V} \bullet \dot{\mathbf{V}} + \frac{\mu}{R^3}\mathbf{R} \bullet \dot{\mathbf{R}} = 0 \quad (\text{A.6})$$

in general, for any two vectors \mathbf{a} and \mathbf{b} ,

$$\mathbf{a} \bullet \mathbf{b} = ab \cos \theta$$

where θ is the angle between the two vectors.

Assume \mathbf{a} is parallel to itself and the angle between them is 0 and $\cos \theta = 1$, then

$$\mathbf{a} \bullet \mathbf{a} = a^2 \quad (\text{A.7})$$

Take the derivative of both sides of equation (A.7), thus

$$\frac{d}{dt}(\mathbf{a} \bullet \mathbf{a}) = \frac{d}{dt}(a^2)$$

and applying the chain rule of calculus, the derivative becomes

$$\mathbf{a} \bullet \dot{\mathbf{a}} = \mathbf{a}\dot{\mathbf{a}} \quad (\text{A.8})$$

Rewriting equation (A.8) as

$$V\dot{V} + \frac{\mu}{R^3}\mathbf{R}\dot{\mathbf{R}} = 0$$

or

$$V\dot{V} + \frac{\mu}{R^2}\dot{\mathbf{R}} = 0 \quad (\text{A.9})$$

Take the derivative of equation A.9, we recognise that,

$$\frac{d}{dt} \left(\frac{V^2}{2} \right) = V\dot{V}$$

$$\frac{d}{dt} \left(-\frac{\mu}{R} \right) = \frac{\mu}{R^2}\dot{\mathbf{R}}$$

hence,

$$\frac{d}{dt} \left(\frac{V^2}{2} - \frac{\mu}{R} \right) = 0 \quad (\text{A.10})$$

The term in parenthesis is the specific mechanical energy, ε

$$\varepsilon = \frac{V^2}{2} - \frac{\mu}{R} \quad (\text{A.11})$$

if $\frac{d}{dt}(\varepsilon) = 0$, the $\varepsilon = \text{constant}$ since we get a constant of integration after integrating the the differential equation [5].

A.3 Specific Angular Momentum is a Constant

Take the cross product of the two-body equation of motion with the position vector, \mathbf{R} [5]:

$$\mathbf{R} \times \left(\ddot{\mathbf{R}} + \frac{\mu}{R^3}\mathbf{R} \right) = \mathbf{R} \times 0$$

$$\mathbf{R} \times \ddot{\mathbf{R}} + \frac{\mu}{R^3}(\mathbf{R} \times \mathbf{R}) = 0$$

The cross product of parallel vectors is zero, hence second term goes to zero and we have

$$\mathbf{R} \times \ddot{\mathbf{R}} = 0 \quad (\text{A.12})$$

Now realise that

$$\frac{d}{dt}(\mathbf{R} \times \dot{\mathbf{R}}) = (\dot{\mathbf{R}} \times \dot{\mathbf{R}}) + (\mathbf{R} \times \ddot{\mathbf{R}})$$

where $\dot{\mathbf{R}} \times \dot{\mathbf{R}} = 0$, hence we have [5]

$$\frac{d}{dt}(\mathbf{R} \times \dot{\mathbf{R}}) = \mathbf{R} \times \ddot{\mathbf{R}}$$

substituting this quantity into equation (A.12), we obtain

$$\frac{d}{dt}(\mathbf{R} \times \dot{\mathbf{R}}) = 0$$

but $\dot{\mathbf{R}} = \mathbf{V}$, therefore

$$\frac{d}{dt}(\mathbf{R} \times \mathbf{V}) = 0 \tag{A.13}$$

recall from equation (3.7), the specific angular momentum is

$$\mathbf{h} = \mathbf{R} \times \mathbf{V}$$

thus,

$$\frac{d}{dt}(\mathbf{h}) = 0 \tag{A.14}$$

integrating both sides of this equation, we have [5]

$$\mathbf{h} = \text{constant}$$

Appendix B

Description of Files

B.1 Two-Line Element (TLE) file

Table A:1 Format of a TLE file

Line 1

Column	Description
01	Line Number of Element Data
03 - 07	Satellite Number
08	Classification (U=Unclassified)
10 - 11	International Designator (Last two digits of launch year)
12 - 14	International Designator (Launch number of the year)
15 - 17	International Designator (Piece of the launch)
19 - 20	Epoch Year (Last two digits of year)
21 - 32	Epoch (Day of the year and fractional portion of the day)
34 - 43	First Time Derivative of the Mean Motion
45 - 52	Second Time Derivative of Mean Motion (decimal point assumed)
54 - 61	BSTAR drag term (decimal point assumed)
63	Ephemeris type
65 - 68	Element number
69	Checksum (Modulo 10) (Letters, blanks, periods, plus signs = 0; minus signs = 1)

Line 2

Column	Description
01	Line Number of Element Data
03 - 07	Satellite Number
09 - 16	Inclination (Degrees)
18 - 25	Right Ascension of the Ascending Node (Degrees)
27 - 33	Eccentricity (decimal point assumed)
35 - 42	Argument of Perigee (Degrees)
44 - 51	Mean Anomaly (Degrees)
53 - 63	Mean Motion (Revs per day)
64 - 68	Revolution number at epoch (Revs)
69	Checksum (Modulo 10)

B.2 Subroutine and Microflow

The subprogram of LIFTIM [1] can be grouped into categories as presented below in the Table B.1

Table B.1: Functional grouping of Subprograms

Executive program	MAIN
Numerical integration driver	INTG
Differential equations of motion	QUAD1 QUAD2
Density calculation	ATMSP BIVLGA SOLPAR SUN
Utility routines	TIME PLOT OUTPUT BLOCK DATA XTRAN ELMT

Executive program

The MAIN program reads the input through a NAMELIST and prints a summary of the input data. The primary function of the MAIN program is to act as the executive routine

for the elliptical and circular orbit options (Figure B.1). The routine functions in the following manner as in [1]:

- First, the eccentricity e is checked against the program parameter EBND.
 - If e is greater than EBND, the number of dependent variables are specified to be 4 and subroutine INTG is called using the equations of motion in QUAD1.
 - If INTG returns due to maximum elapsed time or orbital decay, the main program will read in the next case.
 - If INTG returns because the eccentricity has dropped below EBND, then e and ω are set to zero, the semi-major axis is set equal to $(r_a + r_p)/2$ and INTG is called with the equations in QUAD2.
 - If INTG again returns control, the main program will read in the next case.
 - If the initial value of e is less than EBND, then the number of dependent variables is 2 and INTG is called with the equations of motion in QUAD2. When INTG returns control, the next case will be read.

Integration driver

- The subroutine INTG is the driver program for the numerical solution of the differential equations of motion. The first calling argument of INTG specifies which routine will be used to define the equations of motion.

Equations of motion

- Subroutine QUAD1 calculates the numerical values of the differential equations of motion for a fixed time when the elliptical orbit option is specified. The output for the QUAD1 are the values: \dot{r}_a , $\dot{\Omega}$, \dot{r}_p , and $\dot{\omega}$. \dot{r}_a and \dot{r}_p are calculated from Equations 4.10a and 4.10b. e is estimated from Equation 4.7a while $\dot{\omega}$ and $\dot{\Omega}$ are obtained from Equations 4.7c and 4.7d respectively.
- QUAD2 calculates the numerical value of the differential equations for the circular orbit option for a given time. The outputs are \dot{a} and $\dot{\Omega}$ and are calculated from Equations 4.14a and 4.14b.

Density calculations

- ATMSP, calculates the atmospheric density for a given altitude according to the Jacchia 70 model atmosphere. ATMSP has two entry points;

- The first entry requires the input variables XNS, XMS, XLS, the Earth-Sun unit vector, the F10.7 and $\bar{F}10.7$ heating parameters for a given time as supplied by SOLPAR, the present Julian date (XMJD), the geomagnetic index (A_p) as supplied by SOLPAR and the day number (DD). These input variables depend only on time and not altitude.
- The second entry is composed of altitude dependent calculations only. Time is held constant and the altitude is varied according to the true anomaly when the integrals in Equations 4.10c, 4.10d and 4.14a are solved with the Gauss-Legendre method. The first entry of ATMSP is used for the first call and the second entry is used on all subsequent calls, until the quadrature has been evaluated.
- BIVLGA performs a bivariate table lookup for the logarithm of the corresponding density. Linear interpolations are used between the values in the table. BIVLGA is called from the ATMSP with a value of altitude and the exospheric temperature (T4).
- The subroutine SUN determines the Earth-Sun unit vector in days for a given time from the following:

$$\lambda = 0.017203T + 0.0335 \sin(0.017203T) - 1.41$$

$$\hat{L} = \cos \lambda$$

$$\hat{M} = \cos \varepsilon \sin \lambda$$

$$\hat{N} = \sin \varepsilon \sin \lambda$$

where $\varepsilon = 23.445433^\circ$. The unit vector is required for location of the diurnal bulge in the Jacchia model.

- The SOLPAR routine calculates the heating parameters F10.7 and $\bar{F}10.7$ and the geomagnetic index A_p for a given time. $\bar{F}10.7$ is determined by linear interpolation from a table. Nominally, F10.7 is set equal to $\bar{F}10.7$. If tables for F10.7 and A_p are provided, SOLPAR will interpolate for the proper values of A_p and F10.7.

Utility routines

- Subroutine TIME is used to print out the CPU time required to integrate a single case. It also evaluates the effects of changes in program parameters.
- PLOT handles the interface for plot routines.

- BLOCK DATA contains the coefficients for the Gauss-Legendre quadrature and the present values for the nominal, $+2\sigma$ and -2σ values of the $\bar{F}10.7$.
- OUTPUT has six entry points. The first two entries place the output variables in an array STORE which holds these values until a truncation error is checked. The third entry is called to print STORE if the error is within an acceptable tolerance. Entry four is used when there is a change in step size. Entries five and six are called to print the summary tables after computation. Entry five is for termination on maximum time and six for termination on decay.
- XTRAN converts osculating orbital elements to mean orbital elements.
- ELMT computes the state vectors to orbital elements.

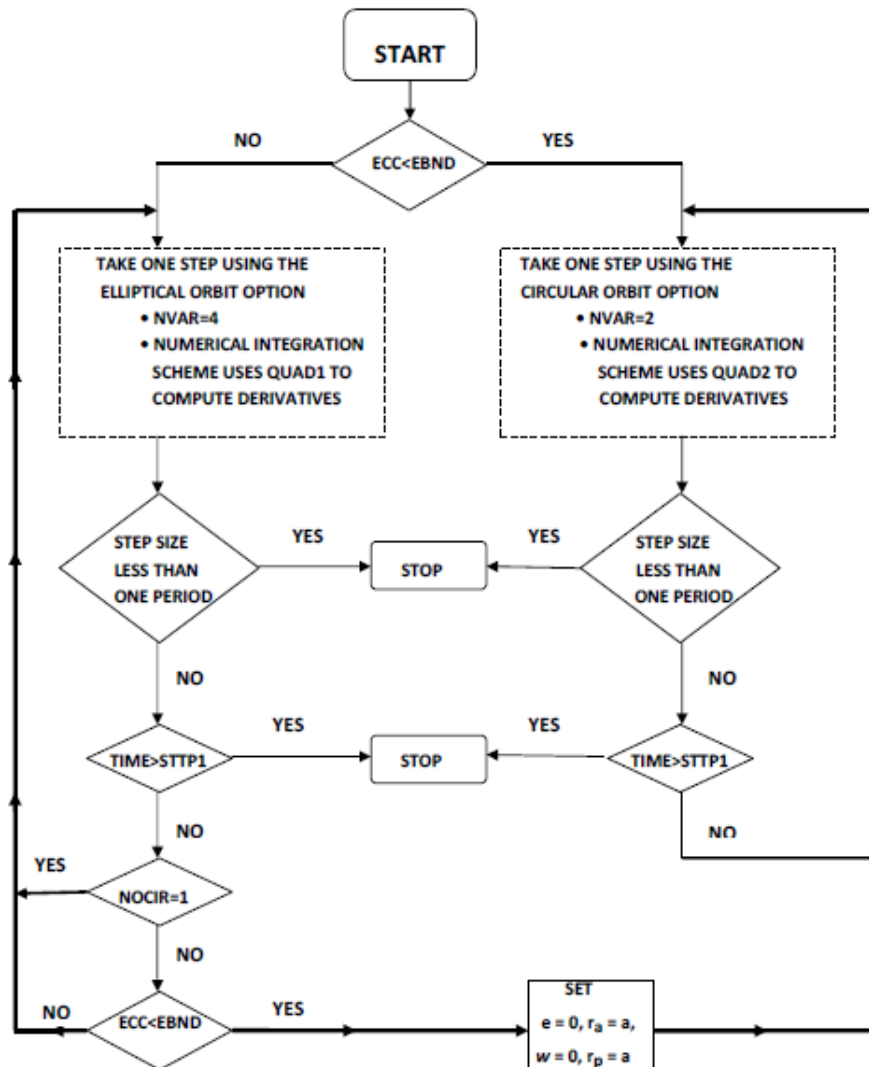


Figure B.1: LIFTIM flow chart showing the routines for circular and elliptical cases [1].

B.3 Input File Format used in Decay Analysis [1]

```

&DATA
TITLE = 'Header to be printed in output file'
XJ2 = J2 harmonic (Earth oblateness factor, 1.08263D-3).
XJ3 = J3 harmonic (-2.54D-6).
XJ4 = J4 harmonic (-1.58D-6).
REQ = Earth equatorial radius ( 6378.14D0 km)
FLATN = Earth flattening (298.257D0)
GM = Earth gravitational parameter (398600.5D0 )
WS = Earth rotation rate (7.2921151467D-5)
TOL = Integration error (.0000001D0)
N1 = Lagrange quadrature degree (10)
N2 = Lagrange quadrature order (10).
NOCIR = Switch over to circular option (0 =yes, 1 keeps integrating elliptical orbit)
EBND = Lower eccentricity limit for elliptical orbits ( 0.0005D0)
CUTOFF = Minimum integration stepsize (days) below which program terminates (1.0D0)
APMIN = Minimum altitude (km) for decay (6378.0D0)
IOSC = Type of input orbital elements ( 0 = osculating, 1 = mean)
ICART = Input coordinate type (0 = orbital elements, 1 = cartesian)
EL = Comma separated orb. elements : a (km), e , i, RAAN, w, M. (all angles in degrees)
R = Comma separated initial ECI position ( X, Y, Z) km
V = Comma separated initial ECI velocity ( Vx, Vy, Vz ) km
AREA = Satellite cross-sectional area (m2)
CD = Drag coefficient (dimensionless)
YMASS = Satellite mass (kg)
XMDOT1 = mass rate of change # 1. (kg.day-1). Not used in simulation (0.0D0)
XMDOT2 = mass rate of change # 2. (kg.day-1). Not used in simulation (0.0D0)
XMDOT3 = mass rate of change # 3. (kg.day-1). Not used in simulation (0.0D0)
TMS1 = Time to start using XMDOT1 (0.0D0) (days)
TME1 = Time to stop using XMDOT1 (10000.0D0) (days)
TMS2 = Time to start using XMDOT2 (0.0D0) (days)
TME2 = Time to stop using XMDOT2 (10000.0D0) (days)
TMS3 = Time to start using XMDOT3 (0.0D0) (days)
TME3 = Time to stop using XMDOT3 (10000.0D0) (days)
CDATE = Initial calendar date ( month, Day, Year) ( e.g. 11, 6,1998)
UT = Initial Universal Time (hh, mm, s) ( e.g. 16, 11, 25)
STTP1 = Maximum simulation (days) 2000.0D0
DELSAV = Initial integration step size (days)
A1 = User-define altitude of interst # 1 (km)
A3 = User-define altitude of interst # 2 (km)
TLIFEX = Solar activity level ( 'nominal' or '+2sigma' or '-2sigma')
IWRIT = Output indicator file (summary, detail, plot) E.g. (1, 1, 1)
/

```

D = Double precision

B.3.1 Iridium-85 Input File for Decay Prediction

```
&DATA
TITLE = 'Iridium-85 orbit decay prediction with epoch 6 Nov. 1998'
XJ2 = 1.08263D-3
XJ3 = -2.54D-6
XJ4 = -1.58D-6
REQ = 6378.14D0
FLATN = 298.257D0
GM = 398600.5D0
WS = 7.2921151467D-5
TOL = .0000001D0
N1 = 10
N2 = 10
NOCIR = 0
EBND = 0.0005D0
CUTOFF = 1.0D0
APMIN = 6378.0D0
IOSC = 1
ICART = 1
EL = 0.0d0, 0.0d0, 0.0d0, 0.0d0,0.0d0
R = 4615.726576913d0, -5140.0645351089d0, -3.2502133726271d0
V = 0.39971817161889d0, 0.34452728595463d0, 7.5738578564604d0
AREA = 5.12D0
CD = 5.0D0
YMASS = 689.0D0
XMDOT1 = 0.0D0
XMDOT2 = 0.0D0
XMDOT3 = 0.0D0
TMS1 = 0.0D0
TME1 = 10000.0D0
TMS2 = 0.0D0
TME2 = 10000.0D0
TMS3 = 0.0D0
TME3 = 10000.0D0
CDATE = 11, 6,1998
UT = 16, 11, 25
STTP1 = 2000.0D0
DELSAV = 10.0D0
A1 = 300.0D0
A3 = 200.0D0
TLIFEX = 'nominal'
IWRIT = 1, 1, 1
/
```

B.3.2 Starshine-1 Input File for Decay Prediction

```
&DATA
TITLE = 'Starshine-1 orbit decay prediction with epoch 5 June, 1999'
XJ2 = 1.08263D-3
XJ3 = -2.54D-6
XJ4 = -1.58D-6
REQ = 6378.14D0
FLATN = 298.257D0
GM = 398600.5D0
WS = 7.2921151467D-5
TOL = .0000001D0
N1 = 10
N2 = 10
NOCIR = 0
EBND = 0.0005D0
CUTOFF = 1.0D0
APMIN = 6378.0D0
IOSC = 1
ICART = 1
EL = 0.D0, 0.0D0, 0.0D0, 0.D0, 0.0D0
R = -1470.8847577407d0, -6597.4000198937d0, 7.575148260619d0
V = 4.6590650961199d0, -1.0378271436944d0, 6.0205117611652d0
AREA = 0.1809D0
CD = 2.1366D0
YMASS = 39.0D0
XMDOT1 = 0.0D0
XMDOT2 = 0.0D0
XMDOT3 = 0.0D0
TMS1 = 0.0D0
TME1 = 10000.0D0
TMS2 = 0.0D0
TME2 = 10000.0D0
TMS3 = 0.0D0
TME3 = 10000.0D0
CDATE = 6, 5,1999
UT = 07, 21, 00
STTP1 = 2000.0D0
DELSAV = 10.0D0
A1 = 200.0D0
A3 = 100.0D0
TLIFEX = 'nominal'
IWRIT = 1, 1, 1
/
```

B.3.3 SUNSAT Input File for Decay Prediction

```
&DATA
TITLE = 'SUNSAT orbit decay prediction with epoch 9 March, 1999'
XJ2 = 1.08263D-3
XJ3 = -2.54D-6
XJ4 = -1.58D-6
REQ = 6378.14D0
FLATN = 298.257D0
GM = 398600.5D0
WS = 7.2921151467D-5
TOL = .0000001D0
N1 = 10
N2 = 10
NOCIR = 0
EBND = 0.0005D0
CUTOFF = 1.0D0
APMIN = 6378.0D0
IOSC = 1
ICART = 1
EL = 0.D0, 0.0D0, 0.0D0, 0.D0, 0.0D0
R = -611.3596933947160D0, 6818.3129602830699D0, 1885.99916780365D0
V = 0.7058965616152D0, 1.9564987352054D0, -7.2181300644107D0
AREA = 0.40D0
CD = 3.10D0
YMASS = 63.0D0
XMDOT1 = 0.0D0
XMDOT2 = 0.0D0
XMDOT3 = 0.0D0
TMS1 = 0.0D0
TME1 = 10000.0D0
TMS2 = 0.0D0
TME2 = 10000.0D0
TMS3 = 0.0D0
TME3 = 10000.0D0
CDATE = 3, 9,1999
UT = 0, 0, 00
STTP1 = 50000.0D0
DELSAV = 10.0D0
A1 = 0.0D0
A3 = 0.0D0
TLIFEX = 'nominal'
IWRIT = 1, 1, 1
/
```

B.3.4 ZACUBE-01 Input File for Decay Prediction

```
&DATA
TITLE = 'ZACUBE1 at epoch 1 October, 2012'
XJ2 = 1.08263D-3
XJ3 = -2.54D-6
XJ4 = -1.58D-6
REQ = 6378.14D0
FLATN = 298.257D0
GM = 398600.5D0
WS = 7.2921151467D-5
TOL = .0000001D0
N1 = 10
N2 = 10
NOCIR = 0
EBND = 0.0005D0
CUTOFF = 1.0D0
APMIN = 6378.0D0
IOSC = 1
ICART = 0
EL = 6978.0D0, 0.000D0, 97.03D0, 0.0D0, 0.0D0, 0.0D0
R = 0.0D0, 0.0D0, 0.0D0 V = 0.0D0, 0.0D0, 0.0D0
AREA = 1.30D0
CD = 2.20D0
YMASS = 1.30D0
XMDOT1 = 0.0D0
XMDOT2 = 0.0D0
XMDOT3 = 0.0D0
TMS1 = 0.0D0
TME1 = 10000.0D0
TMS2 = 0.0D0
TME2 = 10000.0D0
TMS3 = 0.0D0
TME3 = 10000.0D0
CDATE = 10, 1, 2012
UT = 10, 10, 00
STP1 = 20000
DELSAV = 100.0D0
A1 = 0.0D0
A3 = 0.0D0
TLIFEX = 'nominal'
IWRIT = 1, 1, 1
/
```

Appendix C

M-FILES

C.1 Routine for Estimated Drag Sail Size

```
% Routine for Estimated Drag Sail Sizes
clear all, close all;
m1 = 100;
m2 = 1000;
ma = [m1:m2];
for z = 1:200:length(ma)
    p(z) = ma(z)+ 100;

Cd = 2.2; % Drag Coefficient
Amin = 0.25; % Minimum Frontal Area (Incl. Solar Panels) in m^2
Amax = 0.4; % Maximum Frontal Area in m^2

Hmin = 100; % Minimum Altitude in km
Hmax = 800; % Maximum Altitude in km
rho0 = 6.98*10^-12; % Density at Altitude in kg/m^3
hstarmin = 54.8; % Scale Height at Minimum Altitude in km
hstarmax = 68.7; %Scale Height at Maximum Altitude in km
FOS = 1.2; %Margin for Orbital Lifetime

% Physical Constants
rE = 6378.14; %Radius of Earth in km
mu = 398000; %Earth Gravitational Constant km
g0 = 9.81; %Earth Gravitational Acceleration in m/s^2
```

```

%Calculate Density Variation over the some range
h0 = [Hmin:Hmax];
for j = 1:length(h0)
r(j) = h0(j)+rE;
v(j) = sqrt(mu/r(j));
hstar(j) = hstarmin + ((hstarmax-hstarmin)/length(h0))*j;
rho(j) = rho0*exp(-(h0(j)-Hmin)/hstar(j));
end

%Perform Time Integration over range of Altitudes and Area
%Cd Case

for u = 1:length(h0)
Area(u) = Amin + ((Amax - Amin)/length(h0))*u;
for b = 1:length(h0)
tlo(u,b) = (p(z)/(r(b)*1000*v(b)*1000*Area(u)*Cd*rho(b))*hstar(b)*1000);
dayslow(u,b) = tlo(u,b)/(24*3600);
if dayslow(u,b)>365*FOS && dayslow(u,b) < 400*FOS
optlo(u,b) = dayslow(u,b);
else
optlo(u,b) = 0;
end
end
end
hold on
figure(1), plot(h0(1,:), (dayslow(1, :)/365/1000))
end

xlabel('Altitude(km)')
ylabel('Drag Sail (m^2)')
grid on

```

C.2 TLE History File

```

%tle_history.m
%function sat=mytle(tlefile, satname)
clear all
clc
fclose all; close all;

tlefile = 'sunsatp.txt';
%tlefile = 'iridium85.txt';
%tlefile = 'starshine2.txt';
%tlefile = 'icesat.txt';

satname='SUNSAT';
%satname='IRIDIUM85';
%satname='STARSHINE2';
%satname='ICESAT';

%TLE2ORB Get Keplerian elements from Two-Line Element data.
% SAT = TLE2ORB([TLEFILE],satname), where SAT is an array of struct
%
% SAT(1:N).oe
% SAT(1:N).name
% SAT(1:N).epoch
%

```



```

%   as described below. N is the number of satellites.
%
%   NAME is the satellite name,
%   EPOCH is in YMDhms format and
%   OE is the Keplerian orbital elements.
%
%   The orbital elements have the format:
%       a [m]   : semi-major axis
%       e []    : eccentricity
%       i [deg] : inclination
%       W [deg] : longitude of the ascending node
%       w [deg] : argument of perigee
%       M [deg] : mean anomaly at EPOCH
%       P [s]   : orbit period
%
%   The data is extracted from the text file TLEFILE with
%   Two-Line Element format of the satellite orbits.
%   To download current satellite data go to:
%
%       http://celestrak.com/NORAD/elements/
%       http://space-track.org
%
%   Then put the file(s) in the ../sat/ directory.
%

fp=fopen('sunsatsp.txt','r');
%fp=fopen('iridium85.txt','r');
%fp=fopen('starshine2.txt','r');
%fp=fopen('icesat.txt','r');
if(fp == -1)
    error('Cannot open file');
end

mu=my_const('G')*my_const('Me');
Pes=24*3600; % revolutions per solar day

counter=0;
%% scan file until satname found
while ~feof(fp)
    %line=fgetl(fp);
    %   found = strcmp(strtrim(line),satname);
    %   if found
    %       break
    %   end

    %% read two lines
    line1=fgetl(fp);
    line2=fgetl(fp);
    %fclose(fp);

    %% Information from LINE0
    sat.name=deblank(satname);

```

```

%% Information from LINE1
sat.satid = line1(3:7);
sat.launchYear = str2double(line1(10:11));
sat.launchNumber = str2double(line1(12:14));
sat.launchpiece = str2double(line1(15:17));
year=line1(19:20);
sat.epochDayOfYear=str2double(line1(21:32));
if str2double(year(1))>4
    syear=['19' year];
else
    syear=['20' year];
end
dayToMin = 1440;
sat.epochYear=str2double(syear);
ep=datevec(datenum(sat.epochYear,0,sat.epochDayOfYear));
sat.epoch=ep;
sat.jdeepoch = jday(ep(1),ep(2),ep(3),ep(4),ep(5),ep(6));
sat.ballisticCoeff = str2double(line1(34:43));
sat.n0Dot = str2double(line1(34:43))*2*pi/dayToMin^2;
sat.n0DDot = Str2NumE(line1(45:52))*2*pi/dayToMin^3/1e5;
sat.bStar = Str2NumE(line1(54:61))/1e5;
sat.radPressure = Str2NumE(line1(54:61))/1e5;

%% Information from LINE2
sat.rpd=str2double(line2(53:63)); % rounds per day
P=Pes/sat.rpd;
OE(1)=(mu*(P/2/pi)^2)^(1/3); % semimajor axis
OE(2)=str2double(['.' line2(27:33)]); % eccentricity
OE(3)=str2double(line2(9:16)); % [deg] inclination

OE(4)=str2double(line2(18:25)); % [deg] longitude (or right
                                ascension) of the ascending node

OE(5)=str2double(line2(35:42)); % [deg] argument of periapsis
                                (or perigee)
OE(6)=str2double(line2(44:51)); % [deg] mean anomaly at epoch
OE(7)=P; % orbit period

sat.oe=OE;
sat.p=P;
counter=counter+1;
if mod(counter, 1000) ==0
    disp(['Processing TLE ', num2str(counter)])
end
numdays=365;
if mod(year,4)==0
    numdays=366;
end

```

```

orbelements(counter, 1) = ep(1) + (dom2doy(ep(1),ep(2),ep(3)) +
    ep(4)/24 + ep(5)/(24*60) + ep(6)/(24*3600))/numdays;%sat.jdeepoch;
orbelements(counter, 2:8) = OE(1:7);
orbelements(counter, 9) = sat.ballisticCoeff;
orbelements(counter,10) = (((OE(1)/1000))*(1+OE(2)))-6378.14; %Apogee
                                                                height
orbelements(counter,11) = (((OE(1)/1000))*(1-OE(2)))-6378.14; %Perigee
                                                                height

end

figure(1); plot (orbelements(:,1), orbelements(:,2)/1000-6378.14)% avg.
height
figure(2); plot (orbelements(:,1), orbelements(:,2)/1000)% sma
%figure(3); plot (orbelements(:,1), orbelements(:,10))%Apogee height
figure(4); plot (orbelements(:,1), orbelements(:,11))%Perigee height
figure(5); plot (orbelements(:,1), orbelements(:,3))
grid on

```

C.3 Routine for Computing the various Decay Dates

```

% Computing the various decay dates and time

%plotting routine
fclose all;
close all;
clear all
clc

data = load('perstarshine.DAT'); % LIFTIM data

dataExt = data(:,8); % LIFTIM data

orbitTLE = load('starshine.mat'); % TLE data

yTLE = orbitTLE.orbelements(:,1); % years from TLE data

dataSat = orbitTLE.orbelements(:,10); % TLE data

data1 = load('STA3.DAT'); %STK data

datastk = data1(:,8); % STK data

ystk = data1(:,1);

```

```

oldtime = data(:,1);
n1      = size(data,1);          % length of LIFTIM data
n2      = size(orbitTLE.orbelements,1); % length of TLE data
n3      = size(data1,1); % length of STK data

% calc julian date of Epoch

jd0 = julian(2000, 2, 6, 0,0,0); %sunsat
%jd0 = julian(1998, 11, 6, 16,11,25); %iridium85
%jd0 = julian(1999, 6, 5, 8,11,07); %starshine-2
%jd0 = julian(2003, 2, 19, 0,45,0); %icesat
% jd0 = julian(2012, 10, 1, 10, 00, 00); % zacubel

%add this to days elapsed to decay
data(:,1) = data(:,1) + jd0;
data1(:,1) = data1(:,1) + jd0;
%convert this to decimal years

for i=1:n1
    data(i,1) = decyr(data(i,1));
end

for i=1:n3
    data1(i,1) = decyr(data1(i,1));
end

years1    = data(:,1); % from LIFTIM
years3    = data1(:,1); % from STK

dataInt = interp1(years1, dataExt, yTLE);
datakts = interp1(years3, datastk, yTLE);

Re= 6378.13; %Earth radius

res = dataSat - dataInt; % Error between TLE and LIFTIM
% resstk = dataSat - datakts; % Error between TLE and STK
% res = dataInt - datakts; %Error between LIFTIM and STK

figure %('color','w')

plot(yTLE,orbitTLE.orbelements,'b')% Plots Historic TLE data
% hold on
plot(years1,dataExt,'r') % % Plots LIFTIM data
hold on
plot(years3,datastk,'g--') % Plot STK data
hold on

plot(years1,data(:,7),'r')
hold on
plot(years3,data1(:,7),'g--')
hold on
plot(yTLE,orbitTLE.orbelements(:,11),'b--')

grid on

title('Predicted Decay date using LIFTIM and Schatten Solar Flux Data in
LIFTIM')
ylabel('Altitude (km)')
xlabel('Time (years)')
legend('LIFTIM','Observed-TLE','LIFTIM_S_c_h_a_t_t_e_n')

```

C.4 Routine for Data in STK

```

%%
clear all; fclose all;
clc

fileName = 'C:\Research\decay-results\stkgcube24.txt';
fileName = 'C:\Research\decay-results\za2bdy.txt';

fid = fopen(fileName,'r');

output = textscan (fid, '%s %s %s %s %s %s %s %s %s %s %s %s %s %s');
dom = str2double (output{1});
month = output{2};
year = (str2double(output{3}));
HHMMSS = (output{4});

smp = str2double (output{5}); % Semiparameter (km)
sma = str2double (output{6}); % Semimajor axis (km)
ecc = str2double (output{7}); % Eccentricity
inc = str2double (output{8}); % Inclination (deg)
aop = str2double (output{9}); % Argument of Perigee (deg)
raan = str2double (output{10}); % RAAN (deg)
ha = str2double (output{11}); % Apogee Height (km)
hp = str2double (output{12}); % Perigee Height (km)
pd = str2double (output{13}); % Sidereal Period (sec)
ct = str2double (output{14}); % Orbit count

yyy = []; % Time in Years

%c3 = num2cell(yyy, output);
%covert time days
for k = 1 :length(HHMMSS)
    % read each line of the day values
    dom1 = dom(k);

% read each line of the time values and covert to days
HHMMSS1 = char(HHMMSS(k));
HH = str2double(HHMMSS1(1:2));
MM = str2double(HHMMSS1(4:5));
SS = str2double(HHMMSS1(7:12));

MM2hr = MM/60;
SS2MM = SS/60;
SS2MM2hr = SS2MM/60;
realHH = (HH + MM2hr + SS2MM2hr);
HH2Day = realHH/24;

%all added up days
dd = dom1+HH2Day;

% read the month
month(k);
mn = {'Jan', 'Feb', 'Mar', 'Apr', 'May', 'Jun', 'Jul', 'Aug', 'Sep', 'Oct',
'Nov', 'Dec'};

FLD = 28;

```

```
if mod(year(k),4)==0 % checks leap year
    FLD = 29;          % February last day
end

dysinm = [31 FLD 31 30 31 30 31 31 30 31 30 31];

moy = strmatch(month(k), mn, 'exact');

% all in month dd2month = dd/
days2mn = dd/dysinm(moy);
realmn = moy + days2mn;

%change every thing to years
realmyr = realmn/13 ;
years = year(k)+ realmyr;

YYY = [yyy years]; % Time in years

%tk =str2double({yyy});

end
c = YYY';

for j = 5:14
y =str2double( output{j});
size(y);
c = horzcat(c,y);
end
%save('zacube24stk.txt', 'c', '-ASCII')
save('za2bdystk.txt', 'c', '-ASCII')
```

Appendix D

Predicted Decay Dates using STK

D.1 Iridium-85 Satellite

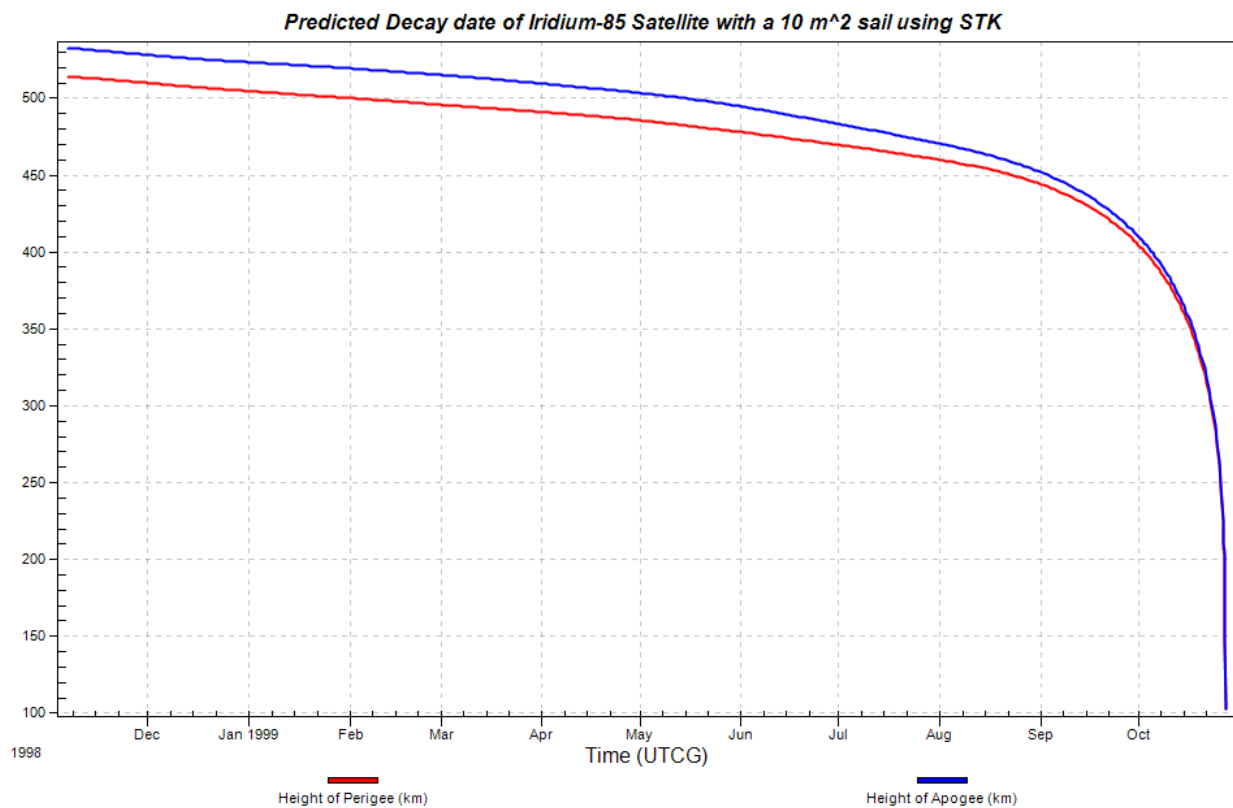


Figure D.1: Predicted decay date with a 10 m² sail using STK for Iridium-85 satellite.

D.2 Starshine-1 Satellite

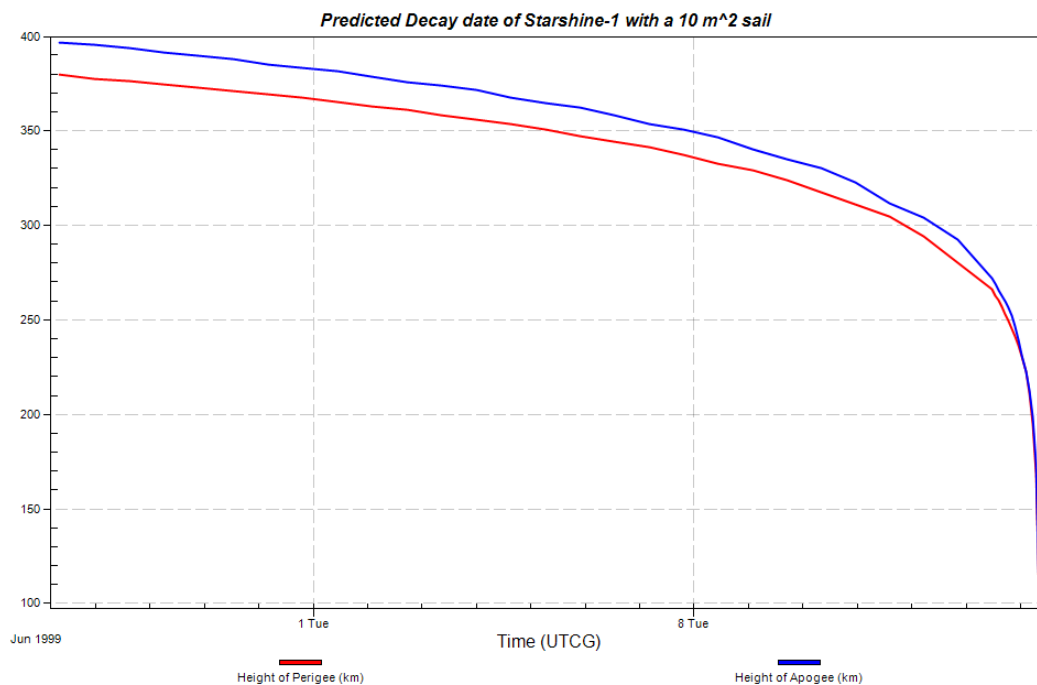


Figure D.2: Predicted decay date with a 10 m² sail using STK for Starshine-1 satellite.

D.3 ZACUBE-01 Satellite

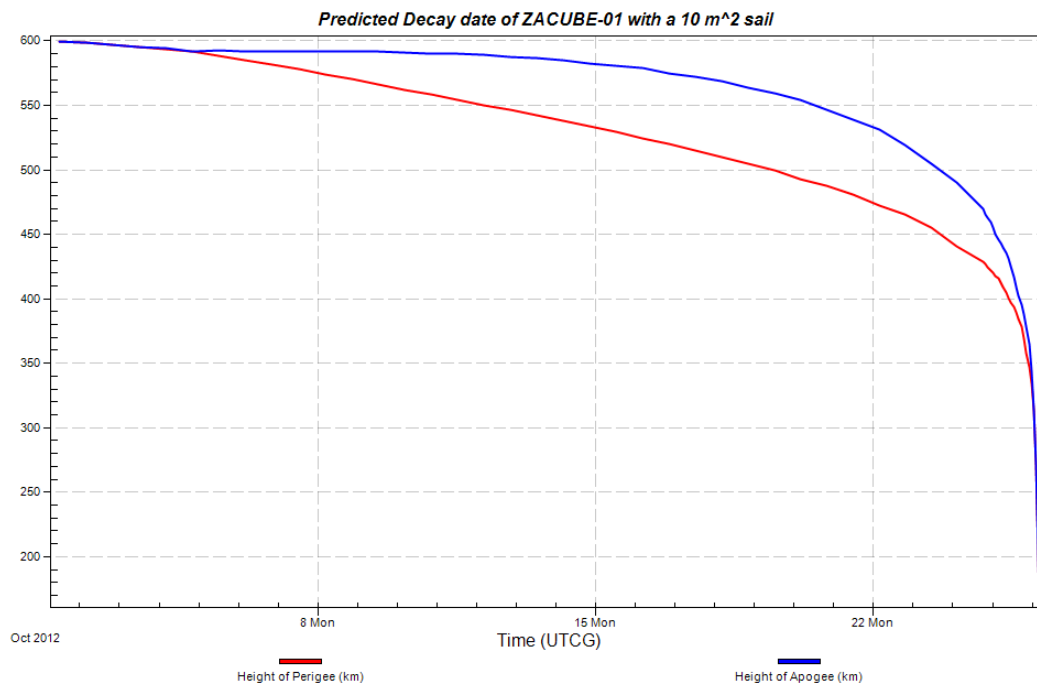


Figure D.3: Predicted decay date with a 10 m² sail using STK for ZACUBE-01 satellite.

Appendix E

De-orbitsail Technique

E.1 Configuration of a sail membrane

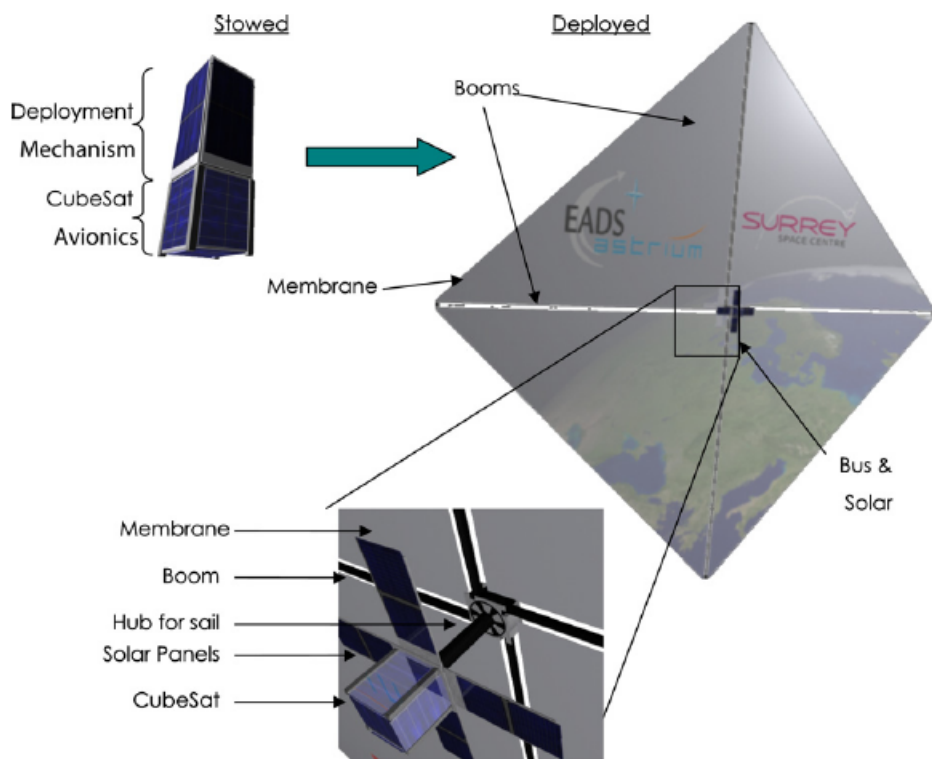


Figure E.1: Sail concept, stowed (left) and deployed (right) [28].

E.2 Observed Monthly Mean Solar Flux Data

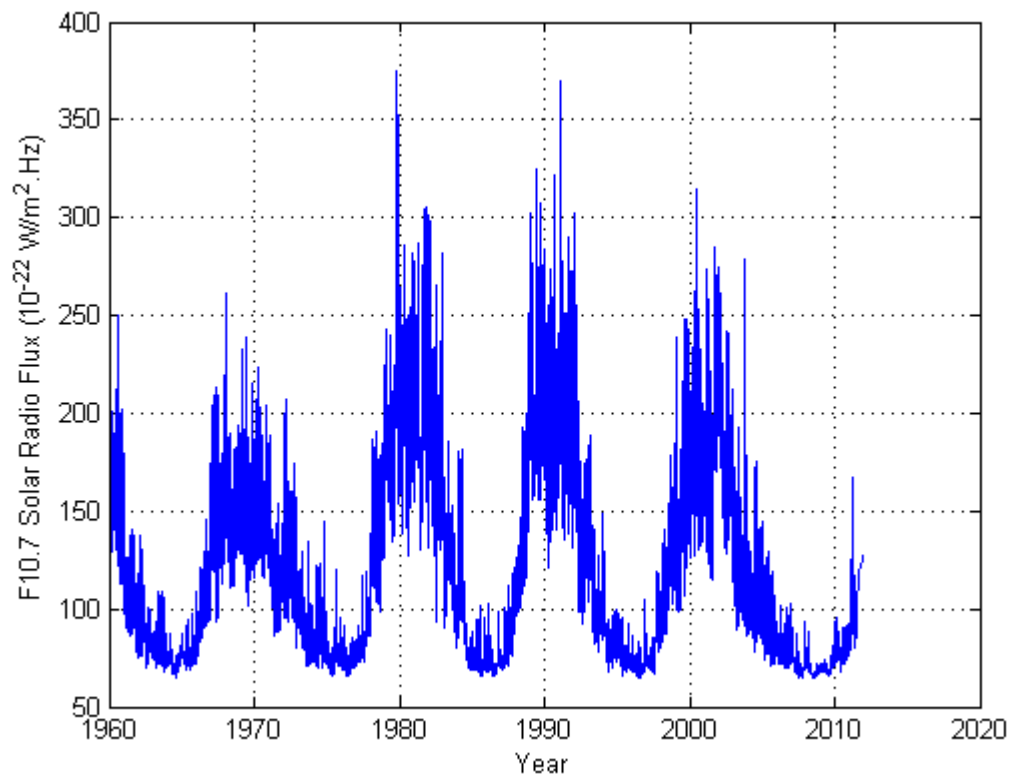


Figure E.2: Observed monthly mean solar flux data